Titre: Title:	3D Full Field Displacement and Strain Measurements at the Microscale in Fiber Reinforced Composites Under Transverse Load Using Digital Image Correlation
Auteur: Author:	Ilyass Tabiai
Date:	2018
Type:	Mémoire ou thèse / Dissertation or Thesis
Référence: Citation:	Tabiai, I. (2018). 3D Full Field Displacement and Strain Measurements at the Microscale in Fiber Reinforced Composites Under Transverse Load Using Digital Image Correlation [Thèse de doctorat, École Polytechnique de Montréal]. PolyPublie. https://publications.polymtl.ca/3796/

URL de PolyPublie: PolyPublie URL:	https://publications.polymtl.ca/3796/
Directeurs de recherche: Advisors:	Martin Lévesque, & Daniel Therriault
Programme: Program:	Génie mécanique

UNIVERSITÉ DE MONTRÉAL

3D FULL FIELD DISPLACEMENT AND STRAIN MEASUREMENTS AT THE MICROSCALE IN FIBER REINFORCED COMPOSITES UNDER TRANSVERSE LOAD USING DIGITAL IMAGE CORRELATION

ILYASS TABIAI
DÉPARTEMENT DE GÉNIE MÉCANIQUE
ÉCOLE POLYTECHNIQUE DE MONTRÉAL

THÈSE PRÉSENTÉE EN VUE DE L'OBTENTION
DU DIPLÔME DE PHILOSOPHIÆ DOCTOR
(GÉNIE MÉCANIQUE)
DÉCEMBRE 2018

UNIVERSITÉ DE MONTRÉAL

ÉCOLE POLYTECHNIQUE DE MONTRÉAL

Cette thèse intitulée :

3D FULL FIELD DISPLACEMENT AND STRAIN MEASUREMENTS AT THE MICROSCALE IN FIBER REINFORCED COMPOSITES UNDER TRANSVERSE LOAD USING DIGITAL IMAGE CORRELATION

présentée par : TABIAI Ilyass
en vue de l'obtention du diplôme de : Philosophiæ Doctor
a été dûment acceptée par le jury d'examen constitué de:

M. VÉTEL Jérôme, Doctorat, président
M. LÉVESQUE Martin, Ph. D., membre et directeur de recherche
M. THERRIAULT Daniel, Ph. D., membre et codirecteur de recherche
M. GONZÀLEZ Carlos, Ph. D., membre
M. TALREJA Ramesh, Ph. D., membre externe

ACKNOWLEDGEMENTS

I would like to thank Prof. Martin Lévesque and Prof. Daniel Therriault for giving me the chance to undertake this project, for their support and trust throughout this thesis. Thanks to their guidance, I was able to learn and gain valuable experience about experimental mechanics, fiber reinforced composites, viscoelasticity, additive manufacturing and polymeric materials. I gained in scientific maturity thanks to your advice and constructive criticism. I would also like to thank them for giving me the opportunity to participate in teaching activities during this thesis.

I owe special gratitude to my coworkers and friends from École Polytechnique and other institutions. Your advice, help and the many animated conversations we had were precious and helped me enhance my work. I would like to particularly thank Rolland Delorme, Patrick Diehl, Yahya Abderrafai, Antonio Castro Moreno, Fubin Tu, Kambiz Chizari, Damien Texier, Gleb Tkachev and Steffen Frey for their contributions and the fruitful discussions all along this project. The technical support of Isabelle Nowlan, Martin Cardonne, Nour Aimene and Bénédict Besner is also gratefully acknowledged.

I would also like to thank the Natural Sciences and Engineering Research Council of Canada (NSERC) and the Mathematics of Information Technology and Complex Systems (MITACS) for the AeroCREATE program which allowed me to benefit from the valuable STEP training program, the possibility to do an internship and for the scholarship I obtained during my PhD.

Finally, I would like to express my heartfelt gratitude to my parents and brother, Nadia, Najib and Nizar. Thank you for being there during the past four and a half years. Last but not least, I would like to thank Houda for her love and unconditional support.

RÉSUMÉ

La rentabilité de l'industrie aérospatiale est fortement liée à une réduction de la consommation de carburant et de la masse des structures utilisées tout en maintenant un niveau de performance et de sécurité similaire. Pour atteindre ces objectifs, les matériaux composites à renfort fibreux (CRF) sont de plus en plus utilisés dans cette industrie. Ces matériaux offrent une résistance spécifique élevée, résistent à la corrosion, sont légers par rapport à leurs propriétés mécaniques et ont de bonnes propriétés de résistance à la fatigue. Ces matériaux sont de plus en plus utilisés mais sont aussi considérés comme une des causes de plusieurs catastrophes aériennes. Les capacités de prédictions de l'état d'endommagement et de rupture de pièces faites en CRF sont encore limitées, tel que démontré par les deux éditions terminées du *World Wide Failure Exercise*.

L'endommagement dans les CRF est caractérisé par une multitude d'événements microscopiques qui se développent puis se regroupent graduellement jusqu'à former un large réseau de micro fissures à travers le matériau. À l'échelle de la fibre, le type d'endommagement le plus critique pour des CRF unidirectionnels est la décohésion inter-faciale entre les fibres et la matrice d'après la littérature. Ce mécanisme commence avec une décohésion inter-faciale en Mode I entre la fibre et la matrice, la fissure inter-faciale se propage ensuite autour de la fibre dans et hors plan. L'interface entre la fibre et la matrice ne peut alors plus transférer de contraintes correctement, ce qui entraîne une augmentation locale de la contrainte autour de la fibre en décohésion. Une des fibres environnantes va ensuite à son tour avoir une décohésion inter-faciale qui se produit dû à l'augmentation de contrainte, et ainsi de suite pour toutes les fibres environnantes. La rupture de l'échantillon se produit éventuellement lorsque les fissures de décohésion commencent à croître dans la matrice, se regroupent et forment un large réseau de fissures qui grandit à travers tout le spécimen. Des observations de décohésion inter-faciale sont disponibles dans la littérature, mais il n'y a pas encore de modèle pour ce mécanisme qui est généralement accepté. La décohésion inter-faciale implique une croissance de la fissure en Mode I, en Mode II et en mode mixte. D'autres mécanismes s'ajoutent aussi, tels que la friction entre la fibre et la matrice, les contraintes résiduelles dues à la cuisson de la matrice et le retrait chimique de la matrice durant la cuisson. Cette combinaison de mécanismes qui participent à la décohésion inter-faciale en font un mécanisme d'endommagement complexe. Des données expérimentales additionnelles, telles que les champs de déplacement ou de déformation in-situ, permettraient de fournir une compréhension plus complète de la décohésion inter-faciale pour différents types de fibres.

Cette thèse a pour but d'étudier expérimentalement l'initiation et la croissance de l'endommagement dans un CRF en chargement transverse, à l'échelle de la fibre (*i.e.*, microscopique). Cette thèse fournit des mesures du champ de déplacement et de déformation in-situ dans et hors du plan d'observation, des mesures de l'aire des fissures inter-faciales pour différents types de fibres durant la croissance de l'endommagement et pour un toron de fibres de carbone.

Dans la première phase de ce travail, un composite à fibre unique a été conçu et fabriqué pour qu'une fibre de taille relativement large, environ 1 mm de diamètre, soit en chargement transverse durant un test de traction. Quatre spécimens de ce type ont été fabriqués, deux d'entre eux contiennent une fibre qui ne forme pas de liens avec l'époxy (PTFE, aussi appelé Teflon $^{\text{TM}}$), le premier ayant une matrice en époxy et le second une matrice en époxy modifiée. Deux autres sont faits avec une fibre qui se lie fortement à l'époxy (acier galvanisé), l'un a une matrice en époxy et l'autre en époxy modifiée. Un montage pour la corrélation d'image numérique (CIN) stéréoscopique a ensuite été utilisé pour obtenir les déplacements des pixels observés et calculer les déformations dans le plan pour la surface visible d'une des fibres et la matrice environnante. Les résultats ont montré que la décohésion inter-faciale se produit en trois étapes, tout d'abord une fissure inter-faciale commence par s'ouvrir en Mode I à l'interface fibre / matrice là où la différence de déplacement hors plan entre la fibre et la matrice est la plus grande et où la déformation dans la direction de la traction, ε_y, est maximale, pour tous les spécimens. La fissure inter-faciale grandit ensuite en mode mixte autour de la fibre. L'effet poisson est visible par la contraction de la matrice dans la direction de la fibre qui fait qu'elle dépasse hors de la matrice. Enfin, lors de la dernière étape, la rupture finale du spécimen se produit différemment pour les spécimens avec une forte cohésion entre la fibre et la matrice et ceux sans cohésion. Pour les spécimens sans cohésion, la rupture finale est provoquée par une fissure qui s'initie et grandit en Mode I dans la matrice à l'endroit où la fibre est compressée horizontalement et où la différence de déplacement hors plan est la plus importante entre la fibre et la matrice. Pour les spécimens avec une forte cohésion, la rupture finale a aussi été provoquée par une fissure en Mode I mais qui s'initie le long d'une des nouvelles surfaces de la fissure inter-faciale, là où ε_y est maximum. Aux alentours de l'interface fibre / matrice, ε_y est 4 à 5 fois supérieur à la déformation appliquée au spécimen. La totalité des résultats expérimentaux, qui contiennent les mesures des champs de déplacement et déformation pour chaque spécimen et chaque pas de temps, sont fournis dans un paquet de données mis à disposition pour effectuer des analyses différentes de la décohésion inter-faciale ou comparer des résultats de simulation pour des modèles d'endommagement micro-mécanique.

La CIN a aussi permis d'obtenir des informations quantitatives à propos des champs de dé-

placement et de déformation concernant la décohésion inter-faciale, mais cette méthode a des limitations, principalement autour de fissures. La CIN ne permet pas non plus d'obtenir des informations quantitatives à propos des fissures elles mêmes car elles perturbent le mouchetis utilisé pour la CIN. Les images utilisées pour l'analyse de CIN et les résultats de cette analyse ont donc été utilisés pour développer une méthode qui permet de précisément délimiter la fissure, déterminer le chemin de la fissure dans les coordonnées de l'image initiale et de mesurer l'aire de la fissure à tout moment. La méthode permet aussi de déterminer avec précision la contrainte ou l'allongement nécessaire pour faire grandir la fissure à travers une zone quelconque de son chemin. Cette méthode a été appliquée aux résultats expérimentaux des expériences précédemment présentées: le spécimen avec une fibre de PTFE moulée dans de l'époxy, et celui avec une fibre d'acier galvanisé moulée dans de l'époxy. Les résultats de cette méthode montrent que l'initiation de la fissure se produit pour la même valeur de déformation appliquée pour les spécimens qui ont une forte cohésion entre la fibre et la matrice et ceux sans cohésion. L'initiation semble donc être indépendante de la cohésion entre la fibre et la matrice. Pour les spécimens avec une forte cohésion, la croissance de la fissure se produit de manière beaucoup plus lente que pour ceux sans cohésion, la croissance de la fissure dans la matrice est retardée, ce qui retarde la rupture du spécimen aussi. La forme du chemin de la fissure finale dans les coordonnées de l'image initiale présente aussi des différences entre les spécimens avec une forte cohésion et sans cohésion. Le programme informatique qui a été utilisé pour implémenter la méthode présentée est fournie comme un logiciel libre pour permettre à d'autres chercheurs d'effectuer des analyses similaires en utilisant des résultats de CIN.

Enfin, un montage d'essai différent qui consiste en un microscope laser confocal à balayage (MLCB) et une machine de micro-traction ont été utilisés pour observer trois spécimens à fibre unique dont les diamètres sont 711 μm, 200 μm et 180 μm. Trois spécimens à fibres uniques ont été préparés, l'un avec une fibre qui n'a pas de cohésion avec l'époxy, le second avec une fibre qui a une cohésion faible avec l'époxy et le dernier avec une fibre qui a une cohésion forte avec l'époxy. Les échantillons fabriqués étaient semblables à ceux utilisés pour le montage de CIN stéréoscopique où la fibre se retrouve aussi en chargement transverse durant l'expérience. Les résultats obtenus ont confirmé les observations et mesures effectuées avec les composites à fibre unique en PTFE et acier galvanisé. Le montage d'essai utilisé a permis d'obtenir des résultats avec une résolution 50 fois plus grande et un grossissement 24 fois grand. En plus des spécimens à fibre unique, un spécimen a aussi été préparé avec un toron de fibres de carbones au lieu d'une fibre unique. Différentes zones du toron ont été observées: un large toron contenant environ cent fibres, un toron plus petit qui ne contient que cinq fibres et une fibre de carbone unique isolée. Chaque fibre a un diamètre d'environ

7.5 µm. Les champs de déplacement et de déformation dans le plan en plus des mesures de profondeur ont été obtenus pour chaque zone observée. L'endommagement s'est initié et est resté localisé sur les bords des torons. Les fissures inter-faciales commencent par apparaître à l'interface des fibres qui se trouvent à la périphérie du toron. Elles se regroupent ensuite en une large fissure autour de chaque toron qui grandit. Les fibres à l'intérieur du toron avec une centaine de fibres ne sont pas affectées par l'endommagement. La présence de fissures dans la direction de la fibre, *i.e.* les fissures hors-plan, a aussi été analysée. Les fissures hors-plan sont plus larges que les fissures visibles dans le plan. Les résultats de mesure hors plan ont aussi montré que l'initiation de fissure serait dû à la présence d'un décalage entre la surface libre de la fibre et celle de la matrice avant le début de l'expérience dû aux différents modules d'Young de la fibre et de la matrice. L'intégralité des résultats expérimentaux générés par ces expériences a aussi été préparée et mise à disposition dans un paquet de données disponible en ligne.

Dans cette thèse, la décohésion inter-faciale de fibres ayant différentes cohésions avec une même matrice a été étudié expérimentalement à différentes échelles pendant que l'endommagement se propage. Les résultats obtenus sont quantitatifs et sont fournis pour permettre à d'autres chercheurs de les utiliser pour obtenir le mode d'ouverture à différents endroits de l'interface par exemple. Ces résultats pourraient aussi être utilisés pour préparer des simulations similaires, pour le placement d'éléments cohésifs par exemple. Les simulations d'endommagement à l'échelle de la fibre peuvent être comparés avec les données des résultats expérimentaux fournis, pour différents types de cohésions.

ABSTRACT

This thesis aimed at experimentally investigate damage initiation and growth of FRCs under transverse loading at the fiber level, provide in plane and out of plane full field measurements and crack area measurements for different single fiber composites and for a bundle of carbon fibers.

Firstly, a single fiber composite specimen is designed and manufactured in such a way that a large fiber, approximately 1 mm in diameter, is under transverse loading during a tensile test. Four specimens were manufactured out of fibers having strong adhesive bonding with epoxies and no adhesive bonding with epoxies combined with an epoxy and a modified epoxy. A stereoscopic Digital Image Correlation (DIC) setup is then used to track 3D displacements and compute in plane strains for a fiber's free surface and its vicinity. The experimental results showed that inter-facial debonding happened in three steps, an inter-facial crack opened under Mode I at the fiber / matrix interface at the location where an out of plane displacement difference between the fiber and matrix was the highest and where ε_y was maximum for all specimens. The inter-facial debonding crack then grew under mixed mode around the fiber while it kept protruding out of the matrix. Finally, specimen failure occurred differently for the specimens with no adhesive bonding compared to the strongly bonded ones. For the ones without adhesive bonding, specimen failure was caused by a crack growing under Mode I in the matrix where fibers were horizontally compressed and large out of plane deformation was experienced. Strongly bonded specimens' failure was also caused by a Mode I crack growing in the matrix but located where the tension is maximal within the inter-facial crack's free surface. The complete experimental results, containing the stereoscopic full field displacement and strain results for each test and timestep, were provided in a data package for further analysis, or benchmarking of simulation results.

DIC provided quantitative information about displacement and strain fields, however, the method has limitations in the vicinity of cracks. In addition, DIC did not provide any quantitative information about cracks themselves. A method using the raw images from the experiment and the DIC results was developed to combine both results and accurately determine the crack area, crack path in the reference coordinates and the exact applied stress on the specimen for the crack to grow through a certain area. This method was applied to the previously mentioned experiments. Results showed that inter-facial crack initiation happens in fact at the same strain value applied on the specimen, whether the fiber has strong or weak adhesive bonding. Crack area growth was after that higher, with respect to the applied

strain, for specimens with no inter-facial bonding. For strongly bonded specimens, crack growth happens much slower, delaying growth of the inter-facial crack into the matrix and specimen failure. The final crack path in the reference coordinate showed differences between the strongly bonded and not bonded specimens, consistent with the different final failure mechanisms observed previously. The code used to obtain these results was open sourced and made available in an online data package hosted on Zenodo.

Finally, micro-tensile experimental setup combined to a Laser Scanning Confocal Microscope (LSCM) was used to observe single fibers of about 200 µm in diameter. Single fiber experiments similar to the ones previously presented were done with a fiber with no adhesive bonding, a fiber with weak adhesive bonding and a fiber with strong adhesive bonding. Out of plane measurements were also done for each micrograph taken. Full field displacement and strain field results confirmed observations and measurements from previous experiments with larger fibers with a higher resolution and magnification. In addition to single fiber composites, a specimen was also manufactured with a bundle of commercial carbon fibers (each fiber is about 7.5 µm) instead of a single fiber. Different areas of the bundle were observed: a large bundle of about 100 fibers, a smaller isolated bundle of about 5 fibers and a single carbon fiber. In plane displacement and strain fields in addition to out of plane measurements were obtained for each experiment and provided quantitative measurements while damage was growing. Damage initiated and then localized at the edges of the bundle, for the large and smaller one. Inter-facial cracks started by appearing for fibers located at the edges of a bundle, these cracks then coalesced, forming a large inter-facial crack all around the bundle while the core remained undamaged. The role of out of plane inter-facial cracks was specifically highlighted as it facilitated the growth of in plane crack. These results also showed that crack initiation might be caused by an initial out of plane mismatch present in all FRCs. The complete experimental results, containing the stereoscopic full field displacement and strain results for each test and timestep, were provided in a data package for further analysis, or benchmarking of simulation results.

In this thesis, inter-facial debonding of fibers with different adhesive bonding strengths was experimentally investigated at different scales while damage is growing. Full field displacement and strain fields measured are provided and can be used by fellow researchers in order to obtain the precise opening mode at any point along the interface, to determine the exact layout of cohesive elements for simulation work, or to benchmark simulation results for various fiber / matrix combination having different adhesive bonding strengths.

TABLE OF CONTENTS

ACKNOWLEDGEMENTS iii

RÉSUMÉ iv

ABSTRACT viii

TABLE OF CONTENTS x

LIST OF TABLES xiv

LIST OF FIGURES xv

LIST OF SYMBOLS AND ACRONYMS xix

LIST OF APPENDICES xxi

CHAPTER 1 INTRODUCTION 1

CHAPTER 2 LITERATURE REVIEW 3
- 2.1 Fiber Reinforced Composites 3
  - 2.1.1 Epoxy manufacturing 4
- 2.2 Damage in FRCs 5
  - 2.2.1 Fiber breakage 5
  - 2.2.2 Matrix micro-cracking 5
  - 2.2.3 Fiber / Matrix: Inter-facial debonding 6
- 2.3 Experimental characterization 8
  - 2.3.1 Single fiber testing 8
- 2.4 Experimental techniques for in-situ observations 10
  - 2.4.1 Acoustic emissions (AE) 10
  - 2.4.2 X-ray tomography 10
  - 2.4.3 Edge replication 10
  - 2.4.4 Scanning Electron Microscope (SEM) 11
  - 2.4.5 Laser Scanning Confocal Microscope (LSCM) 11
  - 2.4.6 Digital Image Correlation 11
- 2.5 Damage modeling 13
  - 2.5.1 World Wide Failure Exercises 13

2.5.2 Macro damage mechanics 15
2.5.3 Micro damage mechanics 15
2.5.4 Mode mixity 17
2.6 DIC applied to damage observation in FRCs 17
2.6.1 DIC and FRCs 17
2.6.2 µDIC and FRCs 17

CHAPTER 3 LITERATURE ANALYSIS AND OBJECTIVES 20
3.1 Problem definition 20
3.2 Research objectives 21

CHAPTER 4 OBJECTIVES AND RATIONALE 23
4.1 Article 1: In-situ full field measurements during inter-facial debonding in single fiber composite under transverse load 23
4.2 Article 2: Hybrid image processing approach for crack area detection and tracking using local Digital Image Correlation results 23
4.3 Article 3: In-situ full field out of plane displacement and strain measurements at the micro-scale in single-reinforcement composites under transverse load . 24
4.4 Long term availability of raw experimental data in experimental fracture mechanics initiative 25

CHAPTER 5 ARTICLE 1: IN-SITU FULL FIELD MEASUREMENTS DURING INTERFACIAL DEBONDING IN SINGLE FIBER COMPOSITE UNDER TRANSVERSE LOAD 26
5.1 Abstract 26
5.2 INTRODUCTION 26
5.3 MATERIALS 29
5.3.1 Specimen manufacture 29
5.3.2 Material properties 31
5.4 METHODS 31
5.4.1 In-situ tensile test procedure 31
5.4.2 Data and image acquisition 32
5.4.3 Digital Image Correlation 33
5.5 RESULTS 35
5.5.1 Interface bonding strength effect on macroscopic behavior 35
5.5.2 Strain evolution 35
5.5.3 Virtual extensometers 42

5.5.4 Out-of-plane evolution 45
5.5.5 Fiber/matrix bonding 48
5.6 DISCUSSION 48
5.6.1 Experimental limitations 48
5.6.2 Advantages of the experimental setup 51
5.6.3 DIC analysis results available online 51
5.7 Conclusion 51

CHAPTER 6 ARTICLE 2: HYBRID IMAGE PROCESSING APPROACH FOR AUTONOMOUS CRACK AREA DETECTION AND TRACKING USING LOCAL DIGITAL IMAGE CORRELATION RESULTS APPLIED TO SINGLE FIBER INTERFACIAL DEBONDING 53
6.1 Abstract 53
6.2 Introduction 53
6.3 Experimental Methods 56
6.3.1 Experimental setup 56
6.3.2 Displacement field measurement by local subset based DIC 58
6.4 Background 59
6.4.1 Damage and crack tracking with DIC limitations 59
6.4.2 Image Processing Methodology 60
6.5 Crack area extraction in single fiber composites 61
6.5.1 DIC-based crack extraction 62
6.5.2 Crack area extraction with the hybrid method 66
6.6 Application of the hybrid method to the experimental data set 68
6.6.1 Crack path visualization in reference frame 68
6.6.2 Volume-based rendering of time-dependent crack growth 71
6.7 Discussion 72
6.8 Conclusion and Outlook 72

CHAPTER 7 ARTICLE 3: *IN-SITU* FULL FIELD OUT OF PLANE DISPLACEMENT AND STRAIN MEASUREMENTS AT THE MICRO-SCAL IN SINGLE REINFORCEMENT COMPOSITES UNDER TRASNVERSE LOAD 76
7.1 Abstract 76
7.2 INTRODUCTION 76
7.3 MATERIALS 80
7.3.1 Specimen fabrication 80
7.3.2 Material properties 80

7.4 METHODS 82
  7.4.1 Experimental setup 82
7.5 RESULTS 85
  7.5.1 Single fiber 85
  7.5.2 Carbon Fiber bundle 94
7.6 DISCUSSION 100
  7.6.1 Strong and weak bonding 100
  7.6.2 Damage initiation 101
  7.6.3 Fiber size effect 101
  7.6.4 Limitations of the study 103
  7.6.5 Experimental data availability 104
7.7 CONCLUSION 104

CHAPTER 8 GENERAL DISCUSSION 106
8.1 Experimental limitations 106
  8.1.1 Image acquisition 106
  8.1.2 Speckle pattern 107
  8.1.3 Out of plane measurements using the LSCM 107
8.2 Damage initiation 108
  8.2.1 Residual stresses measurement 108
  8.2.2 Interface initial state 109
8.3 Matrix viscoelasticity 111

CHAPTER 9 CONCLUSION AND RECOMMENDATIONS 113

REFERENCES 117

APPENDICES 132

LIST OF TABLES

Table 5.1 Elastic and thermal material properties of the constituents studied. The galvanized steel wire and PTFE properties were obtained from the manufacturer's data sheet. The properties for epoxy and modified epoxy were obtained by testing the materials. The epoxy and modified epoxy CTE values were measured using a thermomechanical analysis machine (TMA) 32
Table 5.2 Subset, step, and type of correlation (direct or incremental) parameters selected for each analysis 34
Table 5.3 Maximum stress ($\bar{\sigma}_{\text{max}}$) and strain ($\bar{\varepsilon}_{\text{rupture}}$) values reached while testing each specimen and the stress ($\bar{\sigma}_{\text{crack}}$) and strain ($\bar{\varepsilon}_{\text{crack}}$) values at which it is possible to visually distinguish the inter-facial crack between the matrix and fiber. Galvanized steel fiber specimens significantly improved the strain at rupture (by 2.3% in both cases) 36
Table 6.1 Subset and step parameters selected for each analysis 58
Table 7.1 Studied materials elastic properties. Epoxy and PLA's Young's Modulus and Poisson's ratio were measured experimentally according to the ASTM D638 standard, a 95 % confidence interval was used. The PTFE and HCS's properties were provided as a range by their respective manufacturers 82
Table 7.2 Fiber diameter, size of the area observed and scale for each specimen studied. The height pitch, height step between two out of plane measurements, is also provided 84
Table 7.3 Subset and step parameters selected for each test analysis 85
Table 8.1 Prony series parameters obtained through non-linear least square fit based on creep test data at 11.5MPa. This fitting procedure was automatically done by ABAQUS 111

LIST OF FIGURES

Figure 2.1 Multiscale representation of a wing made out of FRCs. Fibers are woven into a fabric and cured into the resin. 4

Figure 2.2 SEM micrograph of a carbon fiber / epoxy composite loaded under compression. The black lines are a network of micro-cracks growing between carbon fibers (gray discs) in an epoxy matrix. 6

Figure 2.3 Inter-facial damage sequence with growing load on a transversally loaded specimen of Epoxy containing a unique glass fiber of 50 µm diameter observed in-situ through X-ray micro-tomography 7

Figure 2.4 Schematic representations of the most common fiber / matrix interface characterization test. 9

Figure 2.5 (a) Schematics of the 3D DIC method used on a cylindrical setup. (b) Reference subset in an underformed image on the right side. 12

Figure 2.6 Summary of results for the WWFE-II. 14

Figure 2.7 The left drawing shows the traditional local formulation of continuum mechanics, the material is a continua in which each elementary volume interacts with its closest neighbors only. 16

Figure 2.8 Figure (a) presents a contour plot of the vertical displacement for a carbon fiber / epoxy composite under compression along the y direction at a magnification of x2000. Figure (b) presents the central area of Figure (a) with a magnification of x6000 18

Figure 5.1 **(a)** ASTM D638 specimen with an embedded fiber along the z direction. **(b)** Computer aided design (CAD) of the 3D-printed mold. . 30

Figure 5.2 **(a)** Schematic representation of the 3-axis high precision linear stage supporting two cameras with a long range focus stereo microscope used to track the fiber during the test. **(b)** Isometric view of the specimen. 33

Figure 5.3 **PTFE fiber/epoxy** composite loaded in tension in the y direction. . 37

Figure 5.4 **Galvanized steel fiber / epoxy** composite loaded in tension in the y direction. 38

Figure 5.5 **PTFE fiber/epoxy modified with elastomer adduct** composite loaded in tension in the y direction. 39

Figure 5.6 **Galvanized steel fiber/epoxy modified with elastomer adduct** composite loaded in tension in the y direction. 40

Figure 5.7 $\varepsilon^l_{x_m}$ and $\varepsilon^l_{y_m}$ are shown as a function of $\bar{\varepsilon}$ for the four couples of materials tested. 43

Figure 5.8 $\varepsilon^l_{x_f}$ and $\varepsilon^l_{y_f}$ are shown as a function of $\bar{\varepsilon}$ for the four couples of materials tested. 44

Figure 5.9 Out-of-plane displacement of the fiber and areas surrounding it for **PTFE/epoxy** and **galvanized steel/epoxy** specimens. 46

Figure 5.10 Out-of-plane displacement along a vertical line as a function of the position on the line, for the galvanized steel/epoxy and PTFE/epoxy specimens. 49

Figure 5.11 Contour plots of the $\mathcal{C}$ variable for two time-steps early during a test on the **galvanized steel/epoxy** specimen. 50

Figure 6.1 Tensile test specimen used. The arrows show the tensile direction. The fiber is visible as a circle in the middle of the specimen. 57

Figure 6.2 Schematization of the influence of the crack on DIC accuracy. 59

Figure 6.3 PTFE fiber / epoxy composite loaded in tension in the y direction: (a) before damage, (b) at the onset of visually distinguishable damage, and (c) at the onset of crack kinking. 60

Figure 6.4 Crack extraction using DIC tracking data for the PTFE / epoxy specimen with $\bar{\sigma} = 20.2$ MPa and $\bar{\epsilon} = 6.66$ % 62

Figure 6.5 An overview of the filtering performed on the unmatched pixels, which were extracted from the tracking data. 63

Figure 6.6 Crack extraction using texture features in the original camera images for the PTFE / epoxy specimen with $\bar{\sigma} = 20.2$ MPa and $\bar{\epsilon} = 6.66$ %. . 64

Figure 6.7 Crack extraction using the hybrid method for the PTFE / epoxy specimen with $\bar{\sigma} = 20.2$ MPa and $\bar{\epsilon} = 6.66$ %. 64

Figure 6.8 Crack path extraction in the reference frame for the PTFE / epoxy specimen with $\bar{\sigma} = 20.2$ MPa and $\bar{\epsilon} = 6.66$ %. 65

Figure 6.9 PTFE fiber / epoxy composite loaded in tension in the y direction: (a) before damage, (b) at the onset of visually distinguishable damage, and (c) at the onset of crack kinking. 66

Figure 6.10 An overview of our proposed crack estimation approach. 67

Figure 6.11 Timelapse of the crack area detection and extraction presented for the PTFE / epoxy specimen. 68

Figure 6.12 Crack path extraction for two different sets of fiber / matrix. 69

Figure 6.13 Estimated crack area as a function of the applied strain. The area obtained for the PTFE / epoxy and galvanized steel / epoxy specimens are shown as blue and black lines, respectively. 70

Figure 6.14 PTFE fiber with epoxy matrix. 74

Figure 6.15 Galvanized steel fiber with epoxy matrix. 74

Figure 6.16 Crack growth volume visualization. Extracted crack regions from each frame were stacked on top of each other in the direction perpendicular to the image. 74

Figure 6.17 Sensitivity of the crack area with respect to the proposed algorithm parameters. 75

Figure 7.1 **(a)** Computer aided design of the 3D printed mold. The red dashed line shows how the reinforcement was held in the mold. **(b)** Modified ASTM D638 Type V specimen with an embedded transverse fiber. Load is applied along the y direction. 81

Figure 7.2 Schematic illustration of the LSCM paired with the microtensile device for in-situ full field strain measurements. The specimen is mounted into the micro-tensile test machine which is installed on the LSCM plate. 83

Figure 7.3 **PTFE/epoxy** single-fiber composite loaded in tension in the y direction. 86

Figure 7.4 **PLA/epoxy** single-fiber composite loaded in tension in the y direction. 87

Figure 7.5 **HCS/epoxy** single-fiber composite loaded in tension in the y direction. 88

Figure 7.6 The average strain ε_y^T is plotted for two positions around the fiber, for each specimen. 90

Figure 7.7 ε_x^l and ε_y^l are shown as a function of the global strain applied on the specimen $\bar{\varepsilon}$. ε_x^l and ε_y^l are obtained by applying a virtual extensometer around the fibre/matrix interface, as shown on the schematics in Figures **a** and **b**. 92

Figure 7.8 Height measurements along longitudinal and transverse profile lines for each single fiber specimen. The left hand side shows the fiber along with the x and y profile lines over which the z coordinate is extracted. The right hand side shows the actual plots for the z coordinates. . . . 93

Figure 7.9 Micrograph of the area of interest studied for the **CF/epoxy**. The **area on the left** contains a small bundle containing five carbon fibers and a single fiber on the top left. The **area on the right** contains a bundle of carbon fibers with about a hundred fibers. 95

Figure 7.10 Timelapse of **CF** bundle / **epoxy** composite loaded in tension in the y direction, this figure presents results for the area on the **right hand side**, ROI CF1, in Figure 7.9. The bundle contains about 100 CFs. . 96
Figure 7.11 **CF** bundle / **epoxy** single-fiber composite loaded in tension in the y direction for ROI CF2, in Figure 7.9. The bundle contains five CFs and an isolated fiber. 97
Figure 7.12 3D surface profile of the area presented in Figure 7.9 for $\bar{\varepsilon} = 2.5$ % (see Figures 7.10c and 7.11c). 99
Figure 7.13 **(a)** Cropped area around the single fiber shown in Figure 7.9. **(b)** Height measurements along two profile lines shown in (a). The top of the CF is visible as a plateau at about 7 µm. 100
Figure 7.14 Comparison of ε_x^l and ε_y^l for a PTFE macro fiber of 1000 µm in diameter from [1] and results for the PTFE fiber (711 µm) used in this work (presented in Figure 7.7). 102
Figure 8.1 A plasma torch can be used to create a roughness profile on polymers. (a) shows a graph presenting the height of nanocolumns as a function of the oxygen jet plasma treatment time; results are presented for two polymers, PEEK and PMMA. 108
Figure 8.2 The cross-section of a single-fiber surrounded by matrix is schematically shown after curing and once it relaxed. 109
Figure 8.3 (a) shows the initial micrograph (unloaded) of the PLA / epoxy specimen. (b) presents a plot of $z(x)_{PLA}$, the height of each material point along the orange line drawn in (a). 110
Figure 8.4 A standard tensile test pulled in displacement ($v = 0.05$ mm/min) test was performed on a plain dogbone specimen made of the studied matrix epoxy. The test was arbitrarily paused (the machine's crosshead was blocked) for a random amount of time several times during the test. . 112

LIST OF SYMBOLS AND ACRONYMS

Latin symbols

$\mathbf{b}$	Body force vector
$\mathbf{C}$	Stiffness tensor
$\mathcal{C}$	1-standard deviation confidence in displacement match
E	Young Modulus
$\mathrm{G_c}$	Fracture toughness
$\mathrm{G_{Ic}}$	Mode I fracture toughness
$\mathrm{G_{IIc}}$	Mode II fracture toughness
$\mathbf{p}$	Traction vector force
$P(x)$	Probability mass function
$\mathbf{u}$	Displacement vector

Greek symbols

$\alpha*$	Maximum limiting angle for a fiber / matrix debond with a negligible contact zone
ε	Strain tensor
$\bar{\varepsilon}$	Longitudinal strain applied on a specimen
θ_d^-	Inter-facial debonding angle for a fiber half
σ	Cauchy stress tensor
$\bar{\sigma}$	Longitudinal stress applied on a specimen
ψ	Mode mixity

Abbreviations

2D	Two-dimensional
3D	Three-dimensional
AE	Acoustic Emissions
AOI	Area Of Interest
ALM	Atomistic Lattice Models
CDM	Continuous Damage Mechanics
CF(s)	Carbon Fiber(s)
CPU	Central Processing Unit
CTE	Coefficient of Thermal Expansion
DIC	Digital Image Correlation

FEA	Finite Element Analysis
FEM	Finite Element Method
FRC(s)	Fiber Reinforced Composite(s)
HCS	High Carbon Steel
IFSS	Inter-facial Shear Strength
LEFM	Linear Elastic Fracture Mechanics
LSCM	Laser Scanning Electron Microscope
MADM	Macro Damage Mechanics
MDS	Molecular Dynamics Simulation
MIDM	Micro Damage Mechanics
PLA	Polylactic acid
PSU	Polysulfone
PTFE	Polytetrafluoroethylene
ROI	Region of Interest
SDIC	Stereoscopic Digital Image Correlation
SEM	Scanning Electron Microscope
μCT	Micro Computed Tomography
UD	Unidirectional
μDIC	Micro Digital Image Correlation
WWFE	World Wide Failure Exercise
XFEM	eXtended Finite Element Method

LIST OF APPENDICES

Appendix A PUBLISHED PAPERS 132
Appendix B SUBMITTED PAPERS 133
Appendix C OPEN SOURCE CODE 134
Appendix D EXPERIMENTAL DATA PACKAGES 135

CHAPTER 1 INTRODUCTION

Aerospace and automotive industries are driven by fuel consumption reduction, which can be achieved by mass savings. Fiber Reinforced Composites (FRCs) have been increasingly used by these industries to achieve this goal. FRCs offer high specific strength, corrosion resistance, lightweight and fatigue resistance properties. Structures containing FRCs are lighter while still maintaining high mechanical properties. Nowadays, FRCs represent more than 50% in mass of a commercial aircraft such as the Airbus A350-900 XWB and are routinely used within the primary structure [2]. Although the usage of FRCs increased, unexpected composite parts failure still happened and were pointed out as one of the causes of several crashes [2, 3].

Damage in a FRC is characterized by a multitude of microscopic events that gradually develop and lead to a large network of cracks coalescing through the material. At the micro level, the most critical type of damage for unidirectional (UD) FRCs is reported to be fiber / matrix inter-facial debonding. It first initiates at the inter-facial areas under Mode I, then propagates all around the fibers in and out of plane. At this point, the fiber / matrix interface no longer properly transfers stresses, which increases the load on surrounding fibers, until inter-facial debonding occurs for one of them, and so on. Specimen failure eventually happens when inter-facial cracks coalesce and propagate through the matrix. Observations of inter-facial debonding are available in the literature. They show that it is a complex process that involves several other mechanisms (*i.e.*, Mode I, Mode II and mixed mode crack growth, fiber / matrix friction, residual stresses and chemical shrinkage due to curing, in addition to out of plane crack growth). Experimental observations of these phenomena can be used to provide a better understanding of inter-facial debonding.

The World Wide Failure Exercise (WWFE) initiative started in 1991 around the subject of "Failure of polymeric composites and structures: mechanisms and criteria for the prediction of performance". The first exercise showed that there was a lack of faith regarding failure criteria used at the time to provide meaningful failure prediction. The second WWFE edition in 2013 showed that a large scatter and divergence in prediction existed in the results and showed limitations in the existing models to properly predict failure modes. Another conclusion of the second edition of the WWFE is that key experimental data is critically lacking to provide meaningful assessment for certain loading cases and damage mechanisms. Various failure criteria and modeling techniques were available to model damage in FRCs. However no single model received a wide acceptance. There is therefore a need for a better understanding of how damage initiates and propagates at the single fiber level, through full field displacement measurements at the fiber level.

This study focuses on providing fiber / matrix inter-facial debonding in-situ full field stereoscopic measurements for single fiber composites. The main objectives are: *(1)* to provide full stereoscopic displacement and strain fields for single fiber composites with known adhesive bonding strengths and *(2)* to extract quantitative information about damage features for each specimen and to then provide similar results for a commercial life carbon fiber / epoxy composite. The obtained results should be available and easy to explore by fellow researchers. The novelty of this work lies on the application of digital image correlation (DIC) at microscopic scales, out of plane measurements while damage is happening in a FRC and relating full field measurements with known adhesive bonding strengths of different fiber / matrix couples.

This thesis is organized as follows. Chapter 2 presents a literature survey on damage features and local full field measurements methods for composites in addition to current limitations in damage modeling of FRCs. Chapter 3 introduces the project's research objectives and describes the relationship between the objectives and the publication strategy. The three articles resulting from this work are presented in Chapters 4 to 7. Chapter 5 studies stereoscopic full field displacement and strain measurements for single fiber composites with known adhesive bonding strength. Chapter 6 presents a method to accurately extract damage features from digital image correlation results. Chapter 7 studies full field displacement and strain measurements for single fiber composites with known adhesive bonding strength in addition to a multiscale study of damage growth in a bundle of carbon fibers. Chapter 8 discusses the relationship between the articles. The contributions and limitations from this thesis are finally summarized and topics for future studies are recommended.

CHAPTER 2 LITERATURE REVIEW

It is important at this stage to explicitly define some terms since their meanings change from one author to the other in the literature. The same standpoint as [4] was adopted for fracture, damage and fatigue, namely:

- **Fracture:** Fracture is understood as the material's breakage at the fundamental level (e.g. breakage of atomic bonds leading to macrolevel cracks). These phenomena lead to the apparition of new internal surfaces.
- **Damage:** Damage is any irreversible change occurring in a material due to thermo-mechanical loadings that generate physical or chemical energy dissipating processes. Atomic bonds breakage is a manifestation of damage.
- **Failure:** A part is referred to as failed when it can no longer meet the purpose it was designed for. The part's failure is typically associated with an accumulation of damage within the material it is made of.

2.1 Fiber Reinforced Composites

Composites can be defined as materials composed of two or more constituents with different properties and distinct boundaries between them [5]. Many of materials fit within this definition. This work focuses on man-made composites reinforced with long continuous fibers, often called Fiber Reinforced Composites (FRCs). FRCs are conventionally classified based on their constituent materials and their fiber's length and distribution. This thesis focuses on FRCs for which the matrix is a thermoset polymer, sometimes called Fiber Reinforced Plastics (FRPs). Fibers can be woven into various configurations prior to curing within a matrix. When all fibers are aligned along the same direction, the FRC is called a unidirectional (UD) FRC.

FRCs offer advantageous strength / weight and stiffness / weight ratios with respect to metallic alloys often used in aerospace. In addition, a FRCs mesostructure (plies) and microstructure (fibers) can be tailored for a specific application [6]. FRCs mechanical properties, such as strength, are strongly affected by the fiber / matrix interface, which ensures load transfer between the constituents [4]. In addition, these constituents also have large differences between their mechanical properties. Although UD FRCs offer attractive mechanical properties in the direction along the reinforcements, their mechanical properties are significantly weaker in the transverse direction [4]. Figure 2.1 presents a FRC's constituting element. At the microscopic scale (*i.e.,* ≤100 µm, named here the *microscale*), a carbon FRC can be represented as a bundle of UD parallel fibers, having diameters ranging from 5-10 µm surrounded by a homogeneous matrix [7]. At the microscopic scale, a FRC can be seen as a UD composite [8,9].

2.1.1 Epoxy manufacturing

To manufacture a thermoset polymer, such as epoxy, a resin and hardener, two separate liquids are mixed together to initiate polymerization. In its liquid state, a bi-component epoxy can be seen as strands of monomers and oligomers (groups of monomers) [10]. After mixing both components and providing energy as heat, monomers start attaching one to another as a network at chemically active sites, gradually cross-linking into a 3D structure. Each time a monomer bonds to the network, its movement is restricted which creates a loss of free volume [11]. This process is responsible for the so called chemical shrinkage which is partially at the source of a compressive stress applied by the matrix on the fiber during curing.

For a neat epoxy thermoset specimen, the Coefficient of Thermal Expansion (CTE) keeps increasing with temperature during curing. The first step of curing, providing heat, provokes volume expansion. Then, during cooling, the epoxy shrinks again. Fibers and matrix have different CTEs as they are different materials. This difference in CTE induces an expansion

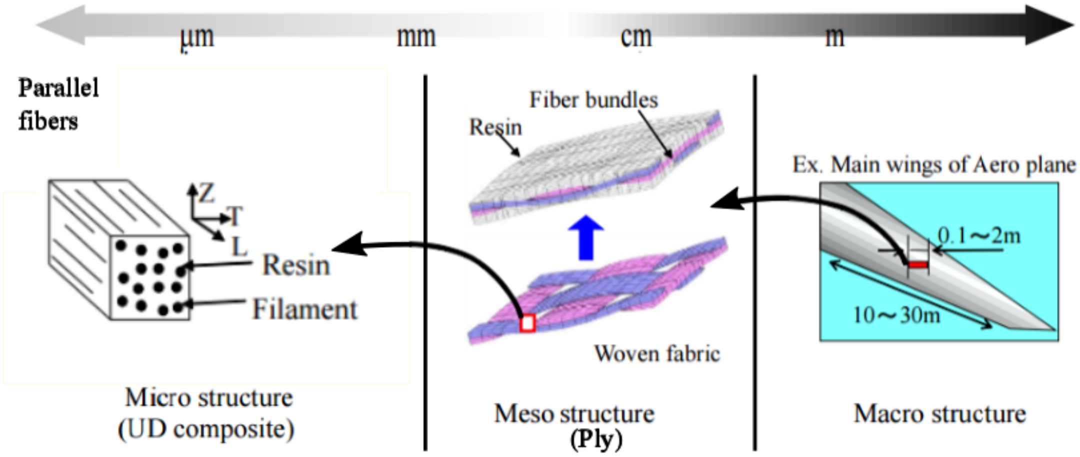

Figure 2.1 Multiscale representation of a wing made out of FRCs. Fibers are woven into a fabric and cured into the resin. A stack of woven fiber cured together is called a ply, once it has been cured within the matrix. Several plies molded into a specific shape form a functional macro structure such as a wing [8]

mismatch between the constituents during and after curing [5, 12]. The total volumetric shrinkage of an epoxy matrix is about 2 to 3% in weight after curing [13]. This shrinkage is due to chemical shrinkage and thermomechanical shrinkage due to the CTE mismatch [14]. Fibers and epoxy develop chemical bonds during curing. Fibers are thus held into the matrix through chemical bonds, chemical shrinkage of the matrix holding fibers into position and an expansion mismatch due to different CTEs.

2.2 Damage in FRCs

It has been reported that damage leading to failure in FRCs can initiate and grow according to a multitude of scenarios [4]. Life damage is characterized by a large number of microscopic events that gradually develop and lead to a large network of cracks coalescing throughout the material [4, 15, 16]. Damage initiates at the micro scale and then keeps growing through the material until macroscopic failure eventually happens. FRCs' microstructure is responsible for their intricate damage mechanisms: inter-facial debonding, matrix microcracking, inter-facial sliding, fiber breakage, fiber microbuckling, void growth, among others [4, 17–20]. The most common damage mechanisms in FRCs were reported to be fiber breakage, inter-facial debonding and matrix micro-cracking [4].

2.2.1 Fiber breakage

When a UD composite is loaded in tension along the fibers' direction, failure initiates when a fiber can no longer sustain the load and eventually snaps gradually into smaller parts. The broken fiber can then no longer transmit stresses to the matrix. A stress redistribution affecting other fibers around the broken one follows, which leads to the failure of other fibers [21]. This process continues until macroscopic failure ensues. Fiber breakage typically occurs at stress concentrations along fibers which are defects usually induced during the manufacturing process [4].

2.2.2 Matrix micro-cracking

Matrix micro-cracking can be attributed to static loading, fatigue loading or even thermal cycling [4, 12, 22]. Micro-cracks are reported to coalesce and grow into a large network of cracks, visible in Figure 2.2. Explanations regarding the origin of these micro-cracks are not clear yet [4]. The micro-cracks could be caused by micro-voids remaining in the part after the curing process, fiber / matrix inter-facial cracks which then propagate in the matrix, or local matrix failure [4]. Figure 2.2 presents a Scanning Electron Microscope (SEM) micrograph of a carbon fibers (CF) / epoxy composite under compression. Micro-cracks are visible in the matrix and at the fiber / matrix interface. The figure shows micro-cracks coalescing into a network.

2.2.3 Fiber / Matrix: Inter-facial debonding

The fiber / matrix interface results from chemical reactions occurring during curing. This means that there are chemical bonds between the matrix and fiber surface, forming a thin area with mechanical properties different from the matrix and the fiber [23]. A chemical solution, called sizing, is usually used in high performance composites to improve the fiber / matrix interface bonding. Depending of the fiber / matrix couple, the bonding strength can be completely different. The effect of the sizing treatment on the failure mechanism is complex and has been studied by several authors (see [24] for example) although no modeling method of the interface has achieved consensus yet [4, 25, 26].

When a UD composite is submitted to transverse loading, inter-facial debonding has been reported to initiate at the fiber / matrix interface and then to propagate along the fiber in and out of plane [9, 27, 28]. Under these circumstances, stresses are no longer fully transferred from the matrix to the fibers, thus increasing the stress in the matrix and further propagating cracks [29]. Damage for a single-fiber composite under transverse loading was

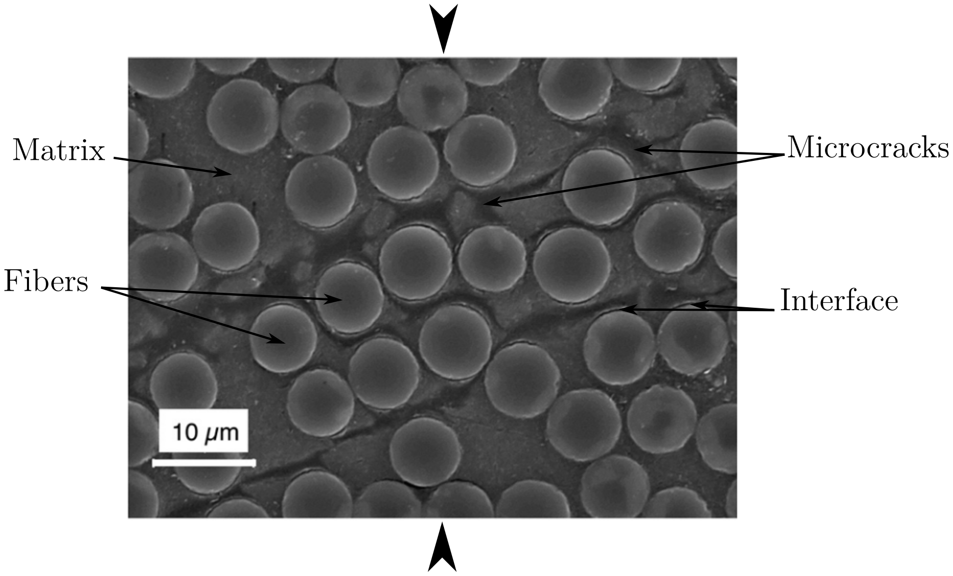

Figure 2.2 SEM micrograph of a carbon fiber / epoxy composite loaded under compression [12]. The black lines are a network of micro-cracks growing between carbon fibers (gray discs) in an epoxy matrix. The fibers are stacked following the z direction. The two large black arrows at the top and bottom of the figure show the loading direction, y

investigated by Martyniuk et al [9]. Through X-Ray Computed Micro-Tomography (μCT), the authors demonstrated how tunneling (i.e., inter-facial debonding along a fiber's axis) directly impacted the inter-facial debonding at the specimen's free surface for an E-glass / epoxy single-fiber composite. The observations documented and validated damage mechanisms and predictions for theories for which experimental data was lacking [9]. Figure 2.3 presents the debonding and tunneling steps during the test performed. The study provided quantitative measurements of damage features appearing in three steps. Firstly, fiber / matrix inter-facial debonding initiated with debonding at the free surface at the intersection of the interface and the tensile loading direction. Next, progressive debonding at the free surface increased gradually. The inter-facial debonding angle for a half fiber is designated by $2\theta_d$. Inter-facial debonding is shown for $2\theta_d^- = 94^o$ and $2\theta_d^- = 114^o$ in Figure 2.3a. As the in plane inter-facial cracks ($2\theta_d^-$) are growing, the out of plane inter-facial crack (along the z axis) is also growing at the same time. Finally, during the last step, $2\theta_d^-$ keeps increasing until it reaches 180° while the out of plane inter-facial crack increases linearly throughout the whole specimen. The out of plane inter-facial crack reaches a steady-state tunnelling at this point in the test, as shown in Figure 2.3b. Failure eventually happens after this last step.

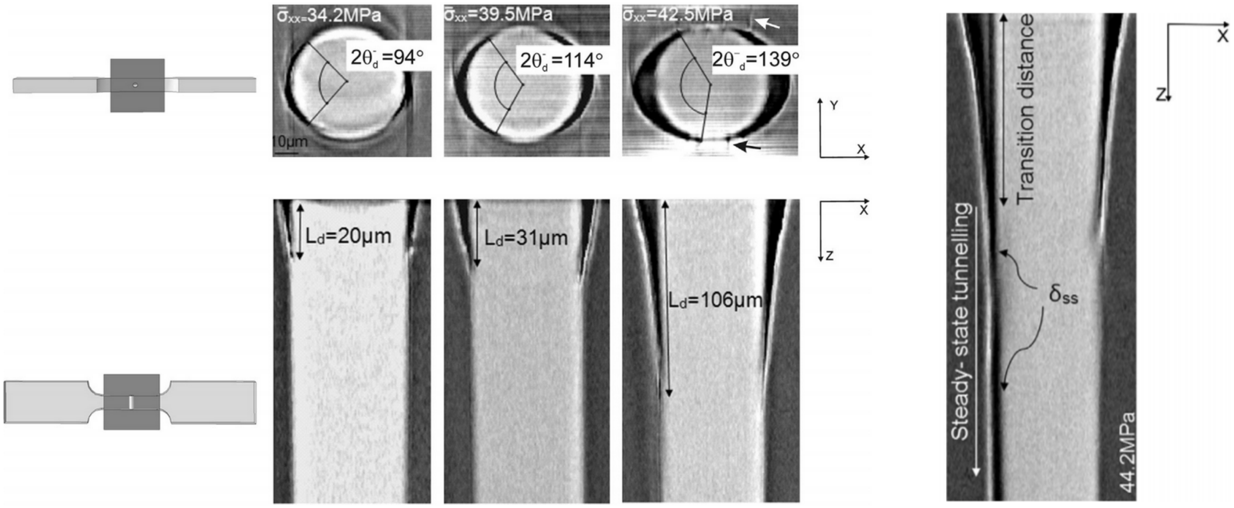

(a) (b)

Figure 2.3 Inter-facial damage sequence with growing load on a transversally loaded specimen of Epoxy containing a unique glass fiber of 50 μm diameter observed in-situ through X-ray micro-tomography [9]. It can be seen that inter-facial debonding starts at the surface and grows in plane (free surface) and out of plane (along z) at the same time. Tensile load is applied along the x direction

Various experimental methods have been used to characterize the mechanical properties of the fiber / matrix interface. The most widely used method is the single-fiber fragmentation test [30–32]. Other tests are also used such as the push out [33,34] or single-fiber pull out [33] test.

2.3 Experimental characterization

2.3.1 Single fiber testing

A variety of single-fiber composite tests have been developed to characterize the fiber / matrix inter-facial shear strength (IFSS) (*e.g.,* the pull-out, push-out, three fiber and microbond tests) [35]. These methods measure an average value of the IFSS [36]. Figure 2.4 schematically shows these methods.

In the single-fiber fragmentation test, the most common of these tests, one unique fiber is pre-strained along the longest direction of a dogbone shaped specimen. The specimen is then gradually loaded under tension in the fiber's direction until it slowly starts to crack into several fragments of constant length, the critical length. This value can then be used to compute the interface strength of this fiber / matrix system. Fragmentation test's results are mainly qualitative since quite different results are obtained in different laboratories for similar material systems and processing conditions [37,38]. In addition, test is not designed to explore transverse damage mechanisms since the fiber is loaded along its longitudinal axis.

The pull-out test involves a fiber partially embedded in a polymer that is then loaded in tension and pulled out of the polymer. The force can be plotted with respect to the distance pulled out and gradually increases during the test until a sudden drop can be seen, when the fiber completely debonds from the material. The maximum force recorded during the test is then used to compute the IFSS [23,32,36,39]. This test does not explore transverse damage mechanisms.

In the microcompression or microindentation test, the specimen is a commercial UD FRC cut perpendicularly to the fibers' direction. A pressure is then applied with an indenter in order to produce inter-facial debonding, and the maximum force provoking debonding is recorded [30]. An analytical formula assuming a set of stresses applied on the fiber can then be applied to retrieve the IFSS. The IFSS can also be retrieved through comparison with FEM results [40]. The microindentation test is however routinely used to qualitatively test real composites after manufacturing, after fatigue or environmental exposition thanks to its easy setup and application [30].

The three fiber test, push-out, and microbond tests are variations of the pull-out test with similar limitations [36]. Figure 2.4 shows a microtension setup. The fiber is partially embedded in a drop of resin, and is then being pulled longitudinally while knives retain the resin drop. The maximum stress applied on the fiber is recorded [39]. These tests rely on single-fiber composites and are designed to determine a stress value above which fiber debonding occurs. This stress value is computed from the force applied on the fiber [4, 23, 26, 41].

The IFSS value computed in these tests is thus an average parameter while the debonding phenomenon itself is local since different opening modes occur along the fiber / matrix interface [9, 23, 26]. Another issue with results obtained from these tests is that friction and chemical bonding are often hardly separable in the proposed models [30, 36, 42]. In addition, none of these tests are designed to test a fiber embedded in a polymer under transverse loading, which is the most critical damage mechanism in FRCs [4].

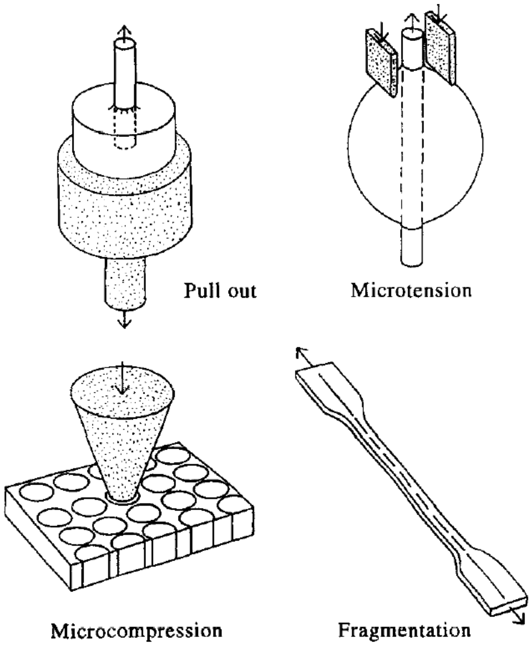

Figure 2.4 Schematic representations of the most common fiber / matrix interface characterization test. In the pull out, the fiber can be seen partially embedded in resin while being pulled out of the resin. The microtension test shows a partially embedded fiber in a drop of resin knives retaining the droplet while the fiber is longitudinally pulled. The microcompression tests use and indenter which applies compressive loaded on a fiber from a commercial composite until inter-facial debonding occurs. The fragmentation test involves tensile tension being applied on a fiber longitudinally embedded in a polymer specimen [36]

2.4 Experimental techniques for in-situ observations

Damage initiation is characterized by several events (e.g. micro-cracks, debonding) simultaneously happening at different places in the specimen. Later during a FRCs' damage life, damage growth is then mainly characterized by micro-cracks coalescing into larger cracks. Since several damage events are happening repeatedly at different places of the material, it is necessary to observe damage while it is happening to better understand the whole damage life in a UD composite at the fiber scale.

2.4.1 Acoustic emissions (AE)

A sensor is used to monitor AE resulting from damage within the composite. AE can be used to monitor a unique fiber's debonding (intra-laminar damage), but can also be used to monitor several plies (inter-laminar) damage evolution. This technique has been widely used to monitor monolithic materials and composite material damages [17, 43–46]. AE can even be used to identify damage progression and origin [17] through a delicate calibration procedure. Simply recording a damage event, without localization, does not need any specific calibration procedure [45].

2.4.2 X-ray tomography

X-ray tomography has been used to observe cracks inside materials [4,47]. This method can be used to detect fiber fractures, delaminations, matrix cracks and provide valuable information about the damage process [48–51]. However, by opposition to AE, damage must occur inside the observation zone (which is a sub-domain of the whole specimen) to be detected. X-ray tomography requires extensive table-top equipment or even nationally sized infrastructures for delivering high resolution images. This method has also been reported to damage epoxy matrices during observation. Epoxy color change has been observed after X-rays were used for observation [9, 51]. The intensity of the color change was also observed to be linked to the exposure time of samples. Fiber protrusion, assumed to be due to inelastic contractions in the fiber's vicinity, were also observed after usage of X-ray for observations [9].

2.4.3 Edge replication

A rubber tape or paste is applied on the sample while it is under load, around the damaged surface. The sample's surface makes an imprint on the paste which gives the surface shape at a certain moment. By doing so at different moments of the experiment, it is possible to track the damage's evolution.

2.4.4 Scanning Electron Microscope (SEM)

SEM produces images by scanning a surface with a focused beam of electrons. SEM can be used to observe features between 1 µm and 0.1 nm. Conventional SEMs are often equipped with high vacuum chambers which are necessary for observation. Carbon fiber / epoxy composites can be observed using a SEM by coating the material with a thin conductive film and adding conductive material between the material and the observation stage. SEM can also be used under partial vacuum at low magnification to avoid coating of non conductive materials. However, in these conditions, the SEM beam is reported to etch the sample's surface [52]. In addition, the chemical bonds of resin polymers, such as epoxy, have also been reported to break and reform due to a SEM beam. The mechanical properties of epoxies are affected by it as the observation surface becomes more brittle [53]. These conditions make in situ usage of SEM for FRCs complex.

2.4.5 Laser Scanning Confocal Microscope (LSCM)

Laser Scanning Confocal Microscope (LSCM) is an optical imaging technique which consists in capturing images at different regular depth intervals, blocking out of focus light at each depth. The method thus enables reconstruction of 3D structures and accurate depth measurements. Most LSCM can be used for observation of features as small as 1 µm.

2.4.6 Digital Image Correlation

Digital image correlation (DIC) is a method to track changes, *e.g.* the displacement field, in a series of deformed images with respect to an initial reference image. DIC experimental setups are usually composed of a single digital image camera (2D DIC) or two cameras (stereoscopic or 3D DIC) used to capture images of the visible surface of a material being deformed.

Several DIC algorithms have been developed since the 1980s, with subset based DIC (local DIC) [56] and finite element-based DIC (FE-based global DIC) [57] being the most popular ones. Global DIC algorithms discretize the specified Region of Interest (ROI) into elements connected by nodes, which are then traced in the target image. All nodal displacements are thus obtained simultaneously. FE-based global DIC employs elements used in the FE method to mesh the image and perform a minimization over the displacement field [58].

The subset based DIC method correlates the intensity (grey levels) distribution of small subsets of pixels between a deformed and a non-deformed image of a same area on a specimen surface to determine the displacement field [56]. The subset size is defined as the set of pixels contained in a square centered on the pixel currently being tracked. Each subset from the non deformed image is then compared with every possible subset in the deformed image, until a deformed subset minimizing the error with a non deformed one is found. The displacement of the pixel at the center of the subset can thus be determined. Figure 2.5a presents a typical stereoscopic DIC setup. This kind of setups can also track out of plane displacements of tracked pixels. In order to distinguish each subset from the others, each specimen's surface is covered with a random pattern. Thanks to its randomness, it can be used to identify each subset in the deformed image through matching and minimization of the error between non deformed and deformed subsets. The subset size is conditioned by the paint dots' size, or average feature size of the speckle pattern used, since it should contain a recognizable pattern with respect to other subsets to yield accurate DIC results [59]. Subsets are compared using

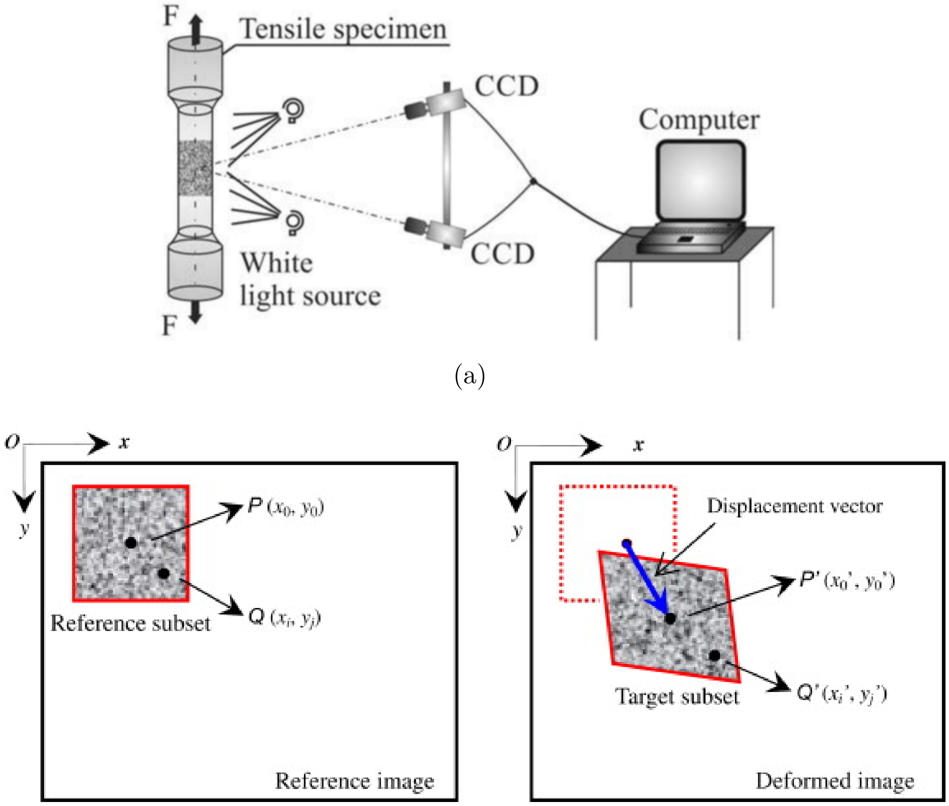

(a)

(b)

Figure 2.5 (a) Schematics of 3D DIC method used on a cylindrical setup. Two CCD cameras acquire images of the tensile test at regular intervals while the specimen is being deformed [54]. (b) Reference subset in an underformed image on the right side. The center pixel P and an arbitrary point Q are highlighted with their respective coordinates. The left side presents the deformed image tracked using DIC, the center position of the target subset is obtained by searching the subset which minimizes the correlation coefficient $\mathcal{C}$ with respect to the reference subset [55] a correlation function. The difference obtained between the reference and deformed image gives an error called the confidence $\mathcal{C}$ [60]. This information can then be used to measure the subset displacement at a subpixel resolution, and thus the whole ROI's kinematic field. The step size defines the spacing between analyzed pixels. Displacement values for pixels not tracked by the DIC software (between two consecutive steps) are interpolated between tracked pixels, assuming a continuous displacement gradient [60]. With growing load, each subset becomes more and more deformed. At some point, subset distortion becomes large enough that the confidence is too large to ensure that the same pixel from the initial image has been found. Features like the apparition of cracks typically lead to a loss of tracking by disturbing the speckle pattern of a subset [56, 60].

2.5 Damage modeling

2.5.1 World Wide Failure Exercises

A large diversity of analytical and computational models attempting to reproduce FRCs various damage mechanisms are available in the literature [4, 26, 61–63]. The World Wide Failure Exercise (WWFE) is an international process that evaluates the predictive capabilities of a number of such damage predictive models [64]. The First exercise focused on 2D failure criteria and showed a clear lack of faith in the failure criteria in use in the 1990s-2000s, but also no clear evidence that any criteria provided meaningful failure predictions [64]. In 2013, the second edition of the WWFE evaluated twelve failure theories applied to polymeric matrices reinforced by carbon and glass fibers in a variety of composites, geometries and loadings. This edition focused on triaxial failure criteria. A large scatter and divergence in predictions were observed between predictions and experiments. The exercise showed that models at the time could hardly predict every failure mode in 3D [65, 66]. This edition also included an isotropic material case, a bulk epoxy material under triaxial loading for which only a quarter of tested theories were able to predict damage evolution. Another conclusion of the second WWFE is that key experimental data is critically lacking to provide meaningful assessment for certain loading cases and damage mechanisms as some cases were considered although no experimental results were available for [65]. Figure 2.6 presents a Table from the WWFE-II report by the organizers. The left half of the table presents a qualitative evaluation of each test case before available additional data related to the test was provided to each group, while the right half presents results after it was provided. Theories were evaluated by organizers based on the quantitative and qualitative assessments and on a judgment on the degree of maturity, degree of correlation with test data, robustness, implementation into software and usefulness for designers. Detailed results show that green colored theories produced accurate results within ±10 % with respect to experimental results for approximately 30 % of test cases, yellow and red colored theories were even less accurate. It is worth noticing that another issue with yellow theories is that it was not possible to judge how the theory can be relied upon in the absence of experimental data for that specific case [65, 67].

The third edition of the WWFE started in 2015 and is focused on benchmarking 3D damage models against experimental data. Complete results for this edition are yet to be published. Although various damage prediction models are available, their ability to predict damage for different materials, geometries and loadings remains limited [66]. The WWFE focuses on commercial composites made of several plies with fibers in various directions under various loading conditions. These exercises show that although various damage models are available, their ability to predict damage for different materials, geometries and loadings remains limited. The analysis of failure in these FRCs models has been studied along two different levels of abstraction, macro damage mechanics (MADM) and micro damage mechanics (MIDM).

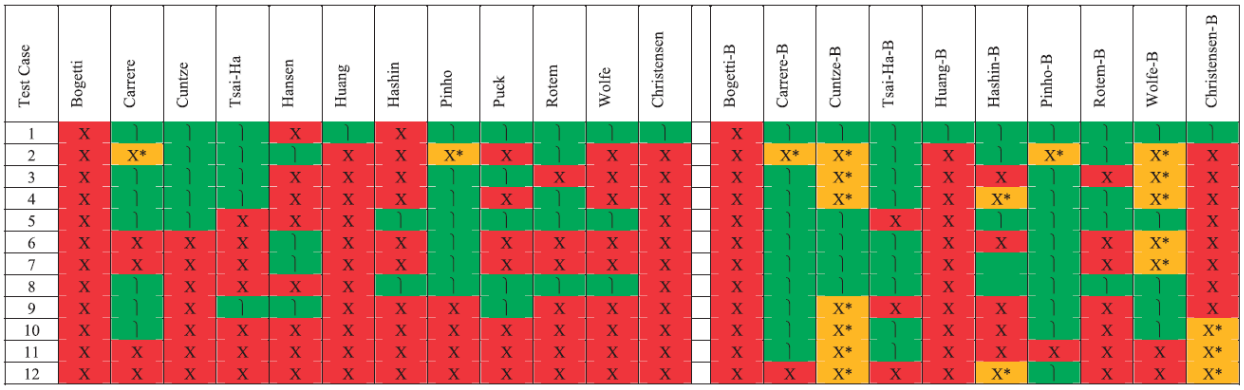

Test Case	Bogetti	Carrere	Cuntze	Tsai-Ha	Hansen	Huang	Hashin	Pinho	Puck	Rotem	Wolfe	Christensen		Bogetti-B	Carrere-B	Cuntze-B	Tsai-Ha-B	Huang-B	Hashin-B	Pinho-B	Rotem-B	Wolfe-B	Christensen-B
1	X	⌉	⌉	⌉	X	⌉	X	⌉	⌉	⌉	⌉	⌉		X	⌉	⌉	⌉	⌉	⌉	⌉	⌉	⌉	⌉
2	X	X*	⌉	⌉	⌉	X	X	X*	X	⌉	X	X		X	X*	X*	⌉	X	⌉	X*	⌉	X*	X
3	X	⌉	⌉	⌉	X	X	X	⌉	⌉	X	X	X		X	⌉	X*	⌉	X	X	⌉	X	X*	X
4	X	⌉	⌉	⌉	X	X	X	⌉	X	⌉	X	X		X	⌉	X*	⌉	X	X*	⌉	⌉	X*	X
5	X	⌉	⌉	X	X	X	⌉	⌉	⌉	⌉	⌉	X		X	⌉	⌉	X	X	⌉	⌉	⌉	⌉	X
6	X	X	X	X	⌉	X	X	⌉	X	X	X	X		X	⌉	⌉	⌉	X	X	⌉	X	X*	X
7	X	X	X	X	⌉	X	X	⌉	X	X	X	X		X	⌉	⌉	⌉	X		⌉	X	X*	X
8	X	⌉	X	X	X	X	⌉	⌉	⌉	⌉	⌉	X		X	⌉	⌉	⌉	X		⌉	⌉	⌉	X
9	X	⌉	X	⌉	⌉	X	X	X	⌉	X	X	X		X	⌉	X*	X	X	X	⌉	X	⌉	X
10	X	⌉	X	X	X	X	X	X	X	X	X	X		X	⌉	X*	⌉	X	X	⌉	X	⌉	X*
11	X	X	X	X	X	X	X	X	X	X	X	X		X	⌉	X*	⌉	X	X	X	X	X	X*
12	X	X*	X	X	X	X	X	X	X	X	X	X		X	X	X*	X	X	X*	⌉	X	X	X*

(X) Red means the model can benefit greatly from further development.

(X*) Yellow means that curve fitting of test data contributed to the model's apparent good correlation with experiments.

(⌉) Green implies the model shows features and capabilities that can potentially be developed into a useful design tool.

Figure 2.6 Summary of results for the WWFE-II [65]. Each row presents predicted tests results for a single test case. The left half of the table presents simulation results for the twelve tested theories before accessing experimental data related to the test. The right half presents simulation results after experimental results were provided. Some theories then improved their predictions after accessing additional data related to the test, shown on the right half. Theories were evaluated by organizers based on the quantitative and qualitative assessments and on a judgment on the degree of maturity, degree of correlation with test data, robustness, implementation into software and usefulness for designer. The green color implies good prediction, the red color means prediction needing improvement and the yellow color means that it was not possible to judge how the theory can be relied upon in the absence of experimental data

2.5.2 Macro damage mechanics

MADM studies a material's overall behavior while damage is modeled by internal variables characterizing the damage growth level, such as crack density growth [4]. The field of MADM is also known as Continuum Damage Mechanics (CDM). CDM requires an evolution law for damage variables [68]. Two main kinds of continuous damage models have mainly been developed in the literature. Nucleation and propagation damage models at the microscopical [69] and also phenomenological damage models based on internal variables to represent damage state have been explored [70]. Damage growth level modeling requires damage laws able to describe how, and at which rate, damage features grow through the material [26, 71]. A better understanding of the real damage mechanisms through experimental observation can be used to devise more accurate damage laws.

2.5.3 Micro damage mechanics

The field of MIDM aims explicitly accounts for the FRC microstructure and damage at the microscopic scale for different kinds of micro-failure mechanisms [4]. Micro-damage mechanics models are often numerically implemented through computational mechanics. Thanks to the constantly increasing available computing power and the development of damage oriented frameworks and tools, computational mechanics appears to be the mostly adapted field to tackle the complexity of FRCs damage problems [12]. However, numerical implementations of micro-mechanical models often require consideration of all details of the microstructure (fiber, matrix and interface) which implies that a very fine grid should be used in the case of FEM (Finite Element Method) for example. Performing an extensive stress analysis of a functional composite part at the fiber level in order to compute the macro properties is still a drastically expensive task which can hardly be routinely performed [72].

eXtended Finite Element Method: X-FEM

FEM is an efficient means for numerically solving equations simultaneously. Researchers have used the method to simulate damage through element deletion process [73] or stiffness degradation methods [74]. It is possible to model UD composites using FEM, either whole plies [51] or even single-fibers with matrix around, using extended FEM [4, 26, 42]. Gonzalez et al. modeled a carbon or glass fiber / epoxy composite under transverse compression at the fiber scale using FEM and showed the impact of interface strength on the damage mechanisms of such a composite. 2D experimental data from various publications was explored against simulations performed by the team. The inter-facial strength and residual stresses were taken as parameters and cohesive elements were used to model the interface. The model succeeded in qualitatively reproducing partial experimental results from various authors, although material parameters, among which the inter-facial bonding strength, were not available in the experimental references and were taken from other references [12].

Meshfree methods: Peridynamics

Figure 2.7 summarizes the conceptual differences between the traditional, local formulation of continuum mechanics and Peridynamics. The Peridynamics theory reformulates the fundamental equations of continuum mechanics in such a way that they can be applied whether a discontinuity is present in the body or not. Instead of using differential equations to express equilibrium, which mathematically breaks down when a discontinuity occurs, Peridynamics uses an integral formulation of equilibrium. As a consequence, the crack initiation and growth problems are included in the Peridynamics' model and do not require additional relations, which are necessary in traditional fracture mechanics to determine different phenomena such as crack initiation, growth velocity, shape and direction. Mesh free numerical methods, such as Peridynamics, can model damage at the micro level thanks to the increasingly available computational power.

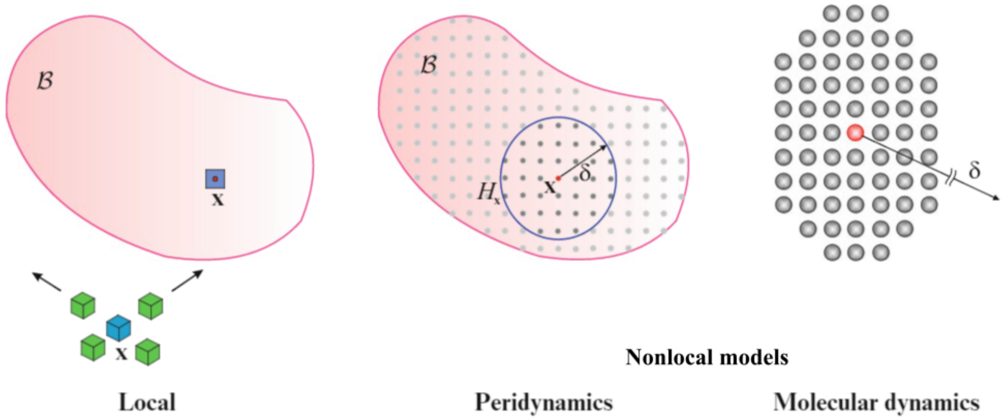

Figure 2.7 The left drawing shows the traditional local formulation of continuum mechanics, the material is a continua in which each elementary volume interacts with its closest neighbors only. The drawing on the right represents Molecular Dynamics models which allows any material point to interact with any other one wherever it is in the material, as long as the inter-atomic potential allows it. The drawing on the middle shows the Peridynamics model, in which each material point can interact with any other material point as long as it is inside its family H_x. The family represents any material point within a sphere of radius δ, also called the horizon [75]

2.5.4 Mode mixity

During inter-facial debonding of a single-fiber under transverse loading, crack propagation is not happening under the same mode at any point of the interface. While some areas are under pure Mode I opening and others under Mode II opening, the inter-facial crack might be growing under mixed mode in other areas [26]. It has been established by Liechti et al. that the fracture toughness G_c of a bi-material interface strongly depends of the mode mixity ψ [76], meaning that $G_c(\psi)$. Varna et al. [77] showed that:

- when the angle $2\theta_d^- \rightarrow 0$, G_c tends toward G_{Ic}, the mode I fracture toughness
- the angle $2\theta_d^- \rightarrow \alpha^*$, G_c tends toward G_{IIc}, where α^* represents the maximum limiting angle for a debond with a negligible contact zone, and G_{IIc} is the mode II fracture toughness

Thus, mode mixity for each area of the interface must be determined experimentally at each time step and requires a method to measure the displacement of matrix material points in the vicinity of a fiber [9].

2.6 DIC applied to damage observation in FRCs

2.6.1 DIC and FRCs

Historical developments of DIC techniques show that subset-based DIC emerged first in 1982 [78]. Since then local DIC algorithms selection and parameters, i.e. shape functions, correlation criterion, subset size selection and interpolation schemes, have been improved. These improvements provided confidence in results obtained using this method [56–58]. Thanks to its easy numerical implementation, high accuracy and efficiency, local DIC has been adopted and used in most commercial systems, making it the mostly used method for practical and experimental mechanics applications. DIC is thus becoming a popular method for in-situ mechanically loaded material samples in different scenarios, *e.g.* accurate full field measurements [79–83], parameter extraction [79], multi axial loadings [80, 81], and damage assessment [82, 83]. It has also been proved to be efficient in characterizing various moduli of composites containing short fibers' displacement fields [84].

2.6.2 μDIC and FRCs

Micro digital image correlation (μDIC) has already been applied to FRCs in order to measure displacements and compute strains at the fiber scale [59, 61]. Canal et al. [61] first used μDIC to investigate strain fields in a unidirectional E-glass / epoxy FRC under transverse compression. Submicron alumina particles were used as a speckle pattern and observed under a SEM to capture images. The study showed the potential for applying μDIC to displacement measurement at the surface of FRCs. Figure 2.8 presents displacement measurements from Canal et al's work. The team was able to accurately measure strains at low magnification, but reported difficulties and a low accuracy when using high magnification. Strain concentrations around fibers for example are hard to identify at that magnification level. The authors pointed out that a higher magnification and speckle pattern with smaller features should have been necessary in order to better capture local strains around fibers [61]. Mehdikhani et al [59] pursued that line of work a few years later by performing a similar experiment and DIC analysis but using a specimen loaded using a three-point bending setup. The authors tried to improve the method used to deposit submicron particles. It was possible to detect strain concentrations due to fibers. The authors reported difficulties to measure small-scale

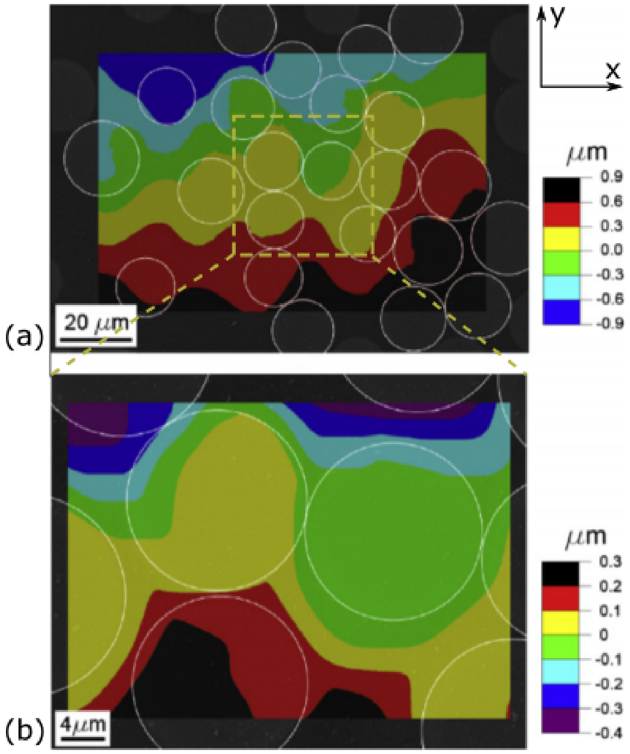

Figure 2.8 Figure (a) presents a contour plot of the vertical displacement for a carbon fiber / epoxy composite under compression along the y direction at a magnification of x2000. Figure (b) presents the central area of Figure (a) with a magnification of x6000. Edges of each fiber were highlighted using an image processing software. Specimens were covered with submicron alumina particle before testing, images snapped during the test were then analyzed using DIC to obtain displacement measurements [61]

concentrations. The averaging and smoothing happening during strain computations out of the measured displacement also has an effect on small-scale concentrations accuracy [59].

Both authors reported difficulties in obtaining accurate measurements in areas of sudden changes in strain and high deformation gradient at the fiber/matrix interface. Both authors employ the use of an additional layer of additional material (alumina particles) which is dispersed at the specimen surface, thanks to a solution which then evaporates (ethanol), in order to generate a speckle pattern which is then used to perform DIC analysis. No damage, and specifically no inter-facial decohesion, was observed during these experiments [59, 61]. While the in-plane responses of FRCs were quantitatively assessed in the literature, the out-of-plane behavior of the matrix around a single-fiber was found to have been solely qualitatively investigated [9].

CHAPTER 3 LITERATURE ANALYSIS AND OBJECTIVES

3.1 Problem definition

The general objective of this study is to provide accurate 3D full field measurements in a fiber and a bundle of fiber's vicinity while damage is growing and to make these results available and easy to explore by fellow researchers. The literature review revealed, in that regard, that:

- Damage in FRCs initiates and grows through a multitude of scenario under different type of loadings due to their heterogeneous nature. Transverse loading has been reported to be the most critical loading mode for UD FRCs.
- In-situ experimental observations of damage in FRCs are lacking. In-situ experimental measurements of in plane and out of plane displacements in a fiber's vicinity while interfacial debonding are not available.
- It has been shown that the fracture toughness $\mathrm{G_c}$ of the fiber / matrix interface is dependent of the mode mixity ψ which is itself dependent on the debond angle. The debond angle was experimentally measured by image processing of in-situ images of a single fiber debonding under transverse loading.
- μDIC has already been applied to FRCs. Authors reported difficulties measuring strains around small concentrations (fibers). μDIC applied to FRCs while damage is happening were not found in the literature.
- DIC analysis can be used to provide quantitative data related to displacement fields. However DIC is not suited for the extraction of damage features (cracks) as the tracking method fails in the vicinity of discontinuities.
- Most studies of damage in FRCs are in 2D. μCT observations of a single fiber composite while damage is evolving showed that strong fiber protrusions were observed, this behavior has been attributed to X-rays affecting epoxy and causing inelastic behavior in the fiber's vicinity. Out of plane measurements of a FRCs' free surface while damage initiates and grows were not found in the literature. Out of plane behavior at the fiber level and its impact of damage mechanisms have not been quantitatively studied.
- Commercial FRC test analysis is hindered by a limited knowledge of the fiber / matrix interface properties. The IFSS cannot help model a fiber / matrix inter-facial debonding

as it is happening under mixed mode. Measurement techniques of inter-facial properties are still limited, especially for commercial FRCs. In addition, modeling of inter-facial debonding at the fiber level for different bonding strength (different fiber / matrix couples) is still an issue.

- 3D full field measurements of FRCs or single-fiber reinforced composites can be used to improve modeling of inter-facial debonding of fiber / matrix couples. These results can also be used to better understand initiation damage mechanisms and growth at the fiber level or benchmark micro-mechanical damage models.

3.2 Research objectives

Based on the thesis objectives outlined in the Introduction and the Literature review, the following specific objectives have been defined and led to three published/submitted journal papers, namely:

1. **Provide full field stereoscopic displacement measurements and compute strains for different fiber / matrix single fiber composites for which adhesive bonding strength is known under transverse loading.**
   A single fiber composite specimen will be manufactured. Different matrix and fibers will be combined to manufacture specimens with different fiber / matrix inter-facial adhesive bonding strengths, which are known. Stereoscopic DIC will be used to measure 3D displacements on the fiber's free surface and its vicinity in situ.

2. **Provide a method to extract quantitative information about damage features from in situ images. Provide quantitative information about damage features for each specimen.**
   Stereoscopic DIC can provide accurate measurements of displacement fields in the fiber's vicinity. DIC will not provide measurements of a crack's size during a test. An additional tool will be designed to process available data to provide accurate measurement of damage features during the test.

3. **Measure stereoscopic full displacement and strain fields in the vicinity of a bundle of carbon fibers.**
   The stress field around a fiber within a bundle of fibers and for a single fiber composite are different. A specimen containing a bundle of carbon fibers will be manufactured and tested in conditions similar to single fiber specimens. In plane displacement and strain

fields along with out of plane depth measurements will be provided in a comprehensive data package.

4. **Provide extensive data (full in-plane and out-of-plane displacement and strain fields) about each experiment in an understandable manner for fellow researchers.**
   Specimen geometries, mechanical properties and fiber / matrix adhesive bonding strengths will be provided in an extensive data package. Force applied, cross-head displacement and full stereoscopic displacement and strain fields will be provided. The data package must be easy to explore and use by researchers in the mechanics' community.

CHAPTER 4 OBJECTIVES AND RATIONALE

The specific objectives defined in Chapter 3 were addressed in one published and two submitted journal papers.

4.1 Article 1: In-situ full field measurements during inter-facial debonding in single fiber composite under transverse load

This article provides in situ stereoscopic full field measurements for four different types of single fiber specimens having different inter-facial bonding strengths. The method to manufacture specimens and measure the displacement during each test is presented along with all DIC parameters used for measurements. Full field in plane strain field and out of plane displacement fields were presented and studied in the article. A fully comprehensive data package was hosted on the Zenodo platform and is provided along with the publication. This article fulfills the first and second specific objectives, which is to provide full field stereoscopic displacement measurements and compute strains for different fiber / matrix single fiber composites and share the data in a usable manner.

This article was published in the journal "Experimental Mechanics", DOI:10.1007/s11340-018-0429-9 in August 2018. This journal "*addresses research in design and implementation of novel or enhanced experiments to characterize materials, structures, and systems; with the goal of publishing articles extending the frontiers of experimental mechanics at both large and small scales.*". The journal was deemed relevant to publish this paper as these results were considered to extend the frontier of experimental mechanics by providing measurements at the microscale.

Specimens design, preparation, testing and data analysis was performed by the author of this thesis. The author worked jointly with Rolland Delorme on the preparation of the experimental setup.

4.2 Article 2: Hybrid image processing approach for crack area detection and tracking using local Digital Image Correlation results

This paper introduces an image processing method which uses DIC results and raw in situ images as inputs in order to directly calculate the crack path and area. The method was tested against manual measurements done using an image edition software and provides accurate results. It was applied in this publication to the first paper's experimental results and completes previously shared experimental results with information about damage. Damage features measurements (i.e. inter-facial debonding cracks) were found to be in agreement with strain field behavior and known bonding strengths. The code used in this publication was open sourced and is available online to be used by fellow researchers. This article fulfills the third objective, which is to provide a method to extract quantitative information about damage features from in situ images.

This publication was submitted to the Engineering Fracture Mechanics journal in November 2018. The journal "*covers a broad range of topics in fracture mechanics to be of interest and use to both researchers and practitioners*" and was deemed relevant to publish this paper as it presents a method which could be of interest for crack analysis based on local DIC results.

This paper was written in collaboration with the *Institut for Visualization and Interactive Systems* at the University of Stuttgart (VISU). VISU provided their expertise regarding image processing and image processing tools in addition to the spatio-temporal crack growth visualization available in the paper. The author of this thesis provided the method to be used, implementation of the code on single fiber experimental results and analysis of results.

4.3 Article 3: In-situ full field out of plane displacement and strain measurements at the micro-scale in single-reinforcement composites under transverse load

This article provides in situ full field in plane displacement and out of plane depth measurements for three different kinds of single fiber / epoxy specimens and for a bundle of carbon fiber / epoxy specimen. The method to manufacture specimens and measure displacement during each test is presented along with all DIC parameters used for measurements. The single fibers used in this work are about five times smaller than those analyzed in the publication described in section 5. Single fiber results are compared with results from the first publication (Section 5) and differences in behavior between strong and weak bonding couples were validated. The carbon fiber bundle was analyzed at different scales in order to understand how damage evolves for a large bundle of a hundred carbon fibers, a small bundle containing five fibers and an isolated carbon fiber. Out of plane inter-facial crack growth is shown to play an important role in damage of FRC under transverse loading, similarities between carbon fibers inter-facial debonding and strong single fiber inter-facial debonding are highlighted. A fully comprehensive data package was hosted on the Zenodo platform and is provided along with the publication. This paper fulfills the fourth objective, which is to measure stereoscopic displacement fields for commercial FRC size fibers.

This publication was submitted to the Experimental Mechanics journal in October 2018. This journal "*addresses research in design and implementation of novel or enhanced experiments to characterize materials, structures, and systems; with the goal of publishing articles extending the frontiers of experimental mechanics at both large and small scales.*". The journal was deemed relevant to publish this paper as these results were considered to extend the frontier of experimental mechanics by providing measurements at the microscale.

Specimens design, preparation and data analysis was performed by the author of this thesis. Damien Texier, a co-author of this publication, provided help and his expertise in using the LSCM and micro tensile testing equipment available at the Ecole de Technologie Supérieure in Montréal. Specimen testing was performed with the assistance of Damien Texier.

4.4 Long term availability of raw experimental data in experimental fracture mechanics initiative

This thesis provides extensive experimental data which can be of use for fellow researchers. Specific attention to the availability of raw data in experimental fracture mechanics and tools used to make it available were thus studied. The corresponding authors of the eleven most cited papers, related to experimental fracture mechanics, for every year from 2000 up to 2016, were kindly asked about the state of the raw experimental data associated with each publication. For the 187 e-mails sent: 22.5 % resulted in outdated contact information, 57.8 % of the authors did receive our request and did not reply, and 19.8 % replied to our request. The availability of data is generally low with only 11 available data sets (6 %). The survey showed that current methods used to make data available are limited as most researchers could not provide raw data due to: inaccessible institutional e-mail address, lack of long term storage, retired authors or that the data would be hard to understand and use by other researchers. A publication associated with this survey provides a list of steps to follow in order to make raw experimental data available for long term and to make data understandable and usable by fellow researchers.

A publication associated with this work was published in Engineering Fracture Mechanics, DOI:10.1016/j.engfracmech.2018.04.030 in June 2018. The experimental data associated with the first and third publications of this thesis (Sections 5 and 7) followed the steps provided in this publication to ensure long term availability of data.

CHAPTER 5 ARTICLE 1: IN-SITU FULL FIELD MEASUREMENTS DURING INTER-FACIAL DEBONDING IN SINGLE FIBER COMPOSITE UNDER TRANSVERSE LOAD

I. Tabiai, R. Delorme, D. Therriault and M. Lévesque, (2017).
Published in: Experimental Mechanics in August 2018.

5.1 Abstract

The fibre/matrix inter-facial damage mechanisms of fiber-reinforced composites (FRCs) are investigated for single-fiber composites under transverse load. A stereoscopic digital image correlation (SDIC) setup is used to analyze *in-situ* quasi-static tests of single-fiber standard dog-bone specimens. *Macro-fibers* (0.9 mm diameter) with radically different inter-facial bonding with the epoxy matrix are used. Damage appears to initiate with fiber debonding at the free surface along the tensile direction. The crack then propagates around the interface while slightly growing along the fiber until a lateral crack initiates on the debonded free surface, provoking specimen failure. The final failure mechanisms appears to be different for strong and weak fiber/matrix bonding. SDIC is used to provide precise measurements of displacements, strains, and out-of-plane displacement during the whole test. Quantitative differences in the displacement fields are measured in the cases of strong and weak bonding between the fiber and matrix. SDIC with macro-fibers is shown to be a promising technique to provide a better understanding of the damage mechanisms in a single-fiber composite and to determine inter-facial toughness of a specific fibre/matrix couple in order to perform accurate modeling of damage in FRCs. Displacement, strain, and confidence field results for each pixel from each experiment and at each time step are also provided for detailed comparison with simulation results.

5.2 INTRODUCTION

At the microscopic scale (*i.e.,* $\leq$ 100 µm, referred to herein as *microscale*), a unidirectional (UD) carbon fiber reinforced composite (FRC) can be represented as a bundle of unidirectional parallel fibers, having diameters ranging from 5-10 µm surrounded by a homogeneous matrix [7]. FRCs mechanical properties, such as strength, are strongly affected by the fiber/matrix interface, which ensures load transfer between the constituents [4].

It has been reported that damage leading to failure in FRCs can initiate and grow according to a multitude of scenarios [4]. Failure is defined as breaking, through crack propagation of a single specimen into two or more parts that cannot bear any additional load. Although FRCs offer high mechanical properties in the longitudinal direction, their mechanical properties are significantly poorer in the transverse direction [4]. Fibers oriented transversely with respect to the applied load can debond from the matrix [12]. Under these circumstances, stresses are no longer fully transferred from the matrix to the fibers, thus increasing the stress in the matrix and further propagating cracks [29]. Cracks favor growth along fibers and are reported to be the most common type of damage in FRCs under transverse loading [28].

Plies submitted to transverse loading exhibit matrix debonding and cracking along the fibers [4]. This phenomenon is reported to occur under mixed-mode conditions [85]. It has also been established that the fiber/matrix interface fracture toughness (G_c) is highly dependent on the debonding mode [9].

Composite damage mechanics have been studied using two main approaches: micro and macro-damage mechanics [4,20]. Macro-damage mechanics relate stiffness changes to internal variables (*e.g.,* crack density) corresponding to damaged states [68]. The field of micro-damage mechanics explicitly accounts for damage at the microscopic scale by predicting the onset and progression of cracks [12]. Such models require knowledge of stress or displacement fields at the micro-scale and of the constituents constitutive theories. The finite element modeling (FEM) technique has been used to model damage through element deletion [73] of stiffness degradation methods [74] at the microscopic scale. These techniques are however limited by the need to generate a new mesh every time the FRC's geometry evolves due to damage [4]. This situation can lead to spatial discontinuities in the vicinity of damage at the micro scale [86].

Cohesive zone modeling [26] and eXtended finite elements (XFEM) [71] have been developed to circumvent these difficulties. Cohesive elements in a FEM obey a cohesive traction law used to allow specific elements to deform while transmitting stresses until a certain stress-strain threshold is reached. Experimental data revealing the behavior of different interfaces and materials during damage initiation can be used to calibrate such laws. XFEM numerically enables a local enrichment of approximation spaces by adding an enrichment term to the standard finite element approximation. Experimental data can also be used in this case to improve the enrichment terms. Quantitative data from the fiber-matrix interface is thus critical for micro-mechanical damage models.

Commercially available composites are constituted of numerous, closely packed fibers. This configuration induces complex tridimensional stress states in the fibers and matrix, even if an overall uni-axial stress field is applied [4, 87]. In contrast, specifically engineered single-fiber composites subjected to mechanical loads yield more manageable stress fields and can be used to study specific damage mechanisms [9, 17, 27, 35].

A variety of single-fiber composite tests have been developed to characterize the fiber/matrix inter-facial shear strength (IFSS) (*e.g.,* the pull-out, push-out, three fiber and microbond tests) [35]. These methods measure an average value of the inter-facial shear strength [36]. The fragmentation test involves a polymer specimen in which a fiber is embedded. The specimen is pulled along the fiber's direction until the fiber is broken into parts of approximately equal lengths. This test is not designed to explore transverse damage mechanisms since the fiber is loaded along its longitudinal axis. The IFSS is then derived from the critical length and the fiber strength. This testing method requires an accurate fiber strength value which is itself dependent on the fiber's diameter and length [32]. In addition, this test does not consider the effect of friction during the debonding process [36].
The pull-out test involves a fiber partially embedded in resin that is then pulled. The maximal force recorded during the test is then used to compute the IFSS [23, 32, 36, 39]. This test does not account for friction effects and does not explore transverse damage mechanisms.
The three fiber test, push-out, and microbond tests are variations of the pull-out test with similar limitations [36]. These tests rely on single-fiber composites and are designed to determine a stress value above which fiber debonding occurs. This stress value is computed from the force applied on the fiber [4, 23, 26, 41]. The IFSS is thus an average parameter while the debonding phenomenon itself is local since different opening modes are occurring along the fiber/matrix interface [23]. Another issue with results obtained from these tests is that friction and chemical bonding are hardly separable. [9, 23, 26, 32]. In addition, none of these tests are designed to test a fiber embedded in a polymer under transverse loading, which is the most critical damage mechanism in FRPs [4].

To better understand the deformation and damage mechanisms at the interface's vicinity the complete strain field around a fiber must be obtained [41]. *In-situ* experiments of single-fiber composites submitted to transverse loads have been conducted by a number of authors using various measurement methods [9, 41, 51, 61, 88–91]. However, most of these experiments measured features about damage or local displacements only, such as the debonding crack size or growth rate; to the best of our knowledge, they did not provide full displacement fields at the fiber/matrix scale. In addition, single-fiber testing does not provide a stress state similar to the one in a commercial composite, at the fiber/matrix interface [92].

Digital Image Correlation (DIC) is an optical method for computing 2D and 3D displacement fields based on cross-correlation. The method requires a random grey level pattern that can either exist naturally on the specimen or be produced artificially (*e.g.,* speckle pattern created with paint droplets). To the best of our knowledge, DIC at the microscopic scale (μDIC) has rarely been applied to bulk FRCs to measure displacements and strains around the fiber/matrix interface using optical microscopes [9, 41, 93] or scanning electron microscopes (SEM) [59, 61, 94] while damage is occurring.

Haldar et al observed damage mechanisms in Palmetto woods at scales ranging from one centimeter to hundreds of micrometers [95]. The study links full-field measurements and multiscale damage mechanisms. For FRCs, authors often reported difficulties obtaining accurate measurements at the fiber/matrix interface or crack edges because of the scale at which DIC is performed, especially after damage initiation [41, 59, 61].

The purpose of this work is therefore to provide detailed and accurate full-field measurement results of inter-facial debonding in single-fiber composites made of different fibers, namely a fiber with a strong adhesive bonding and a fiber with weak no adhesive bonding with the matrix. Our intention is to provide researchers involved in micro-mechanical damage modeling with reliable and complete benchmark data to identify and validate their single-fiber damage models. The full-field measurement results are summarized in a complete (from test start until specimen failure) database of interface mechanical behavior between four couples of fiber/matrix materials. The data provided can easily be compared with FEA results, for example, and the error in displacement or strain between modeling results and our experimental results can be computed for each material point on the observed surface. Please note that this study focuses on large single-fiber composites that were engineered to provide the most accurate DIC measurements.

This paper is organized as follows: Section 5.3 introduces the different materials and samples used. Section 5.4 presents the *in-situ* tensile test setup along with the DIC data acquisition. Section 5.5 presents the strain computed from the displacement full-field measurement results obtained from the experiments. Section 5.6 presents the two main damage sequences observed for different fiber materials and provides additional insights about the method used as well as its limitations.

Raw images, displacement/strain fields as image matrices and load data applied on the specimen are also provided in the online data package [96].

5.3 MATERIALS

5.3.1 Specimen manufacture

The composite samples tested in this work contained a single-fiber embedded inside a standard ASTM D638 Type I dogbone sample. Figure 5.1-a schematically shows the manufactured composite samples. Commercially available galvanized steel fibers having a diameter of 0.9 mm were purchased from Duramax. Polytetrafluoroethylene (PTFE) monofibers having a diameter of 0.99 mm were acquired from Zeus Inc. Two different polymer resins were used as matrices: *(1)* 10 parts by mass of Epon™ 862 epoxy resin with 4 parts of Epikure™ 3274 as a curing agent, and *(2)* the previous mixture with an additional 3.5 parts of elastomer-modified epoxy, to improve its ductility (acquired from Momentive Performance Materials Inc). The composites were designed to ensure accurate measurements with the available μDIC setup and to trigger different damage mechanisms. Note that it was not possible to manufacture carbon or glass epoxy composites since our μDIC setup could not deliver accurate measurements for fiber diameters ranging from $1-50\,\mu\text{m}$.

Figure 5.1-b schematically shows molds used to produce ASTM D638 Type I dogbone samples featuring a single metal or PTFE fiber oriented perpendicularly to the tensile loading direction. The molds were 3D-printed using a fused deposition modeling (FDM) printer. Once prepared, the resin/curing agent mixtures were degassed, poured into the mold, degassed again, and left to cure for 24 hours at room temperature.

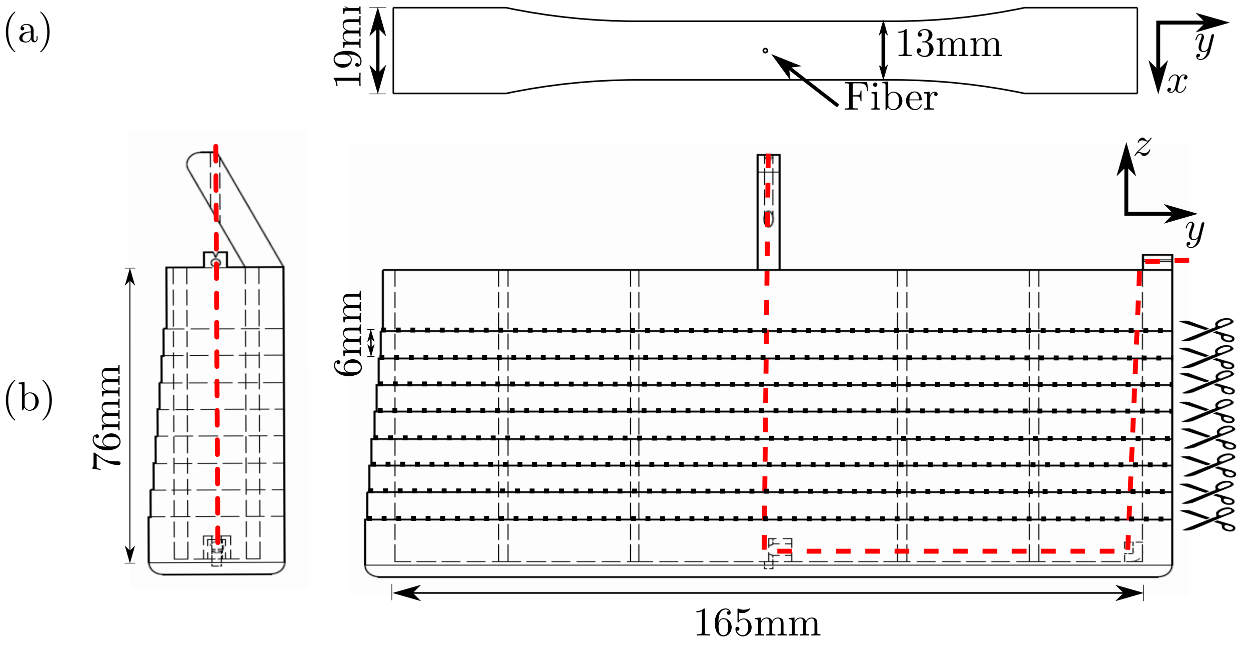

Figure 5.1 **(a)** ASTM D638 specimen with an embedded fiber along the z direction. **(b)** Computer aided design (CAD) of the 3D-printed mold. The dotted path in red shows how the fiber was held to the mold. The mold was cut using an abrasive waterjet cutting machine to provide individual ASTM D638 Type I specimens with a single-fiber perpendicular to the tensile direction once the epoxy was cured

The molds were subsequently cut using an abrasive waterjet cutting machine along the scissor lines shown in Figure 5.1-b. This process was selected to prevent damage that could have been induced by other material cutting techniques [97]. Both specimen sides were then polished with silicon carbide abrasive papers of grits 320, 640, 800 and 1200, consecutively, to provide a smooth surface on which to apply the speckle pattern required for DIC.

5.3.2 Material properties

Four ASTM D638 Type I specimens made of the two epoxies studied, without any embedded fibers, were manufactured and mechanically tested according to ASTM D638 standard to measure their values of Young's modulus and Poisson's ratio. A stereoscopic DIC setup was used to measure displacement on the specimens' surfaces during the tests and to compute strains. The stress was computed using the load from the tensile machine's load cell (50 kN load cell mounted on a MTS Insight ® electromechanical testing machine). The load cell used is rated for a maximal error of 0.64 % for load values higher than 50 N.

Six galvanized steel wires 25.4 cm long were subjected to tensile tests to obtain the material's Young's modulus according to ASTM A370-A4. The edges of the galvanized steel wire were glued to cardboard pieces in order to improve clamping inside the grips. Galvanized steel fibers were chosen for their high bonding strength with epoxy [98]. The PTFE wire properties were obtained from the manufacturer's material datasheet. PTFE is a non-reactive synthetic polymer with a very low coefficient of friction (0.020-0.2 according to the manufacturer) [99] and its surface energy is not sufficiently high to bond with epoxy [100]. Thus, a PTFE fiber inside an epoxy matrix can only be held through compressive forces due to the difference in coefficients of thermal expansion (CTE) between the matrix and fibers.

Table 5.1 lists the mechanical properties of the constituents used as fibers and matrices in these experiments. Although the materials studied are not commercial composites (e.g., carbon-epoxy composites), the four matrix-fiber combinations investigated cover a wide range of behaviors, in which industrial composites should lie.

5.4 METHODS

5.4.1 In-situ tensile test procedure

A manually controlled 3-axis high-precision linear stage carrying the VIC3D micro (version 7.2.4) stereo-microscope system acquired from Correlated Solutions Inc. was placed in front of a MTS Insight ® electromechanical testing machine equipped with a 25 kN load cell.

Figure 5.2-a shows a schematic representation of the setup. The 3-axis precision stage was used to track the fiber's movement out of the cameras' frame. The mechanical test was paused during the stage movements to obtain clear pictures. The duration of each pause was approximately 3 minutes. A ring light around the stereo-microscope lens bringing light from a fiber optic halogen illuminator was used to illuminate the samples. All tests were performed under quasi-static conditions. Each specimen was loaded in displacement-controlled mode at a speed of 0.05 $^{\mathrm{mm}}/_{\mathrm{min}}$. This work presents the results for one single specimen for each fiber/matrix couple. Figure 5.2-b shows the specimen with the direction along which it was mechanically loaded.

5.4.2 Data and image acquisition

The force measured by the load cell and the tensile machine's cross-head displacement were acquired at a frequency of 2 Hz. A picture was acquired by both cameras at each acquisition. The computer to which the cameras were connected was also equipped with a National Instruments data acquisition device to acquire the cross head displacement and force from the load cell at the exact moment each picture was acquired. The region covered by the cameras was approximately 7 mm × 6 mm, with a resolution of about 2.5 $\frac{\mu\mathrm{m}}{\mathrm{px}}$.

The precision stage used to move and support the stereo-microscope was subject to vibrations following manipulation. To ensure that vibrations would not affect captured images, the experiment was paused for an average of 3 minutes each time it was necessary to manipulate the precision stages in order to keep the fiber in the field of view.

Table 5.1 Elastic and thermal material properties of the constituents studied. The galvanized steel wire and PTFE properties were obtained from the manufacturer's data sheet. The properties for epoxy and modified epoxy were obtained by testing the materials. The epoxy and modified epoxy CTE values were measured using a thermomechanical analysis machine (TMA)

Material	Young Modulus (GPa)	Poisson's ratio	CTE (/^{o}C)
Epoxy	2.5 ± 0.9	0.46	60.6×10^{-6}
Modified epoxy	2.8 ± 0.3	0.44	67.6×10^{-6}
Galvanized steel wire	200	0.29	12×10^{-6}
PTFE wire [67]	$0.39 - 0.60$	0.36	$126 - 180 \times 10^{-6}$

5.4.3 Digital Image Correlation

Speckle pattern

A thin layer of white acrylic spray paint (Ultra 2X spray paint, Painter's Touch ®) was applied on each specimen. A mist of black paint was then applied on the white layer with an airbrush equipped with a 150 µm tapered nozzle.

Speckle pattern quality was assessed with the commercial software VicSnap. The software compares the displacement field obtained by DIC for an artificially deformed image for which the imposed deformation is known [56]. The larger eigenvalue of the covariance matrix of the correlation equation is used to obtain the confidence margins, $\mathcal{C}$, for the displacements estimated by DIC for each pixel [56].

The speckle pattern was improved until the smallest possible confidence margins for the Area Of Interest (AOI), which is the area analyzed by the DIC algorithm, was reached. It is possible to improve the speckle pattern by simply removing the paint and re-applying it on the specimen.

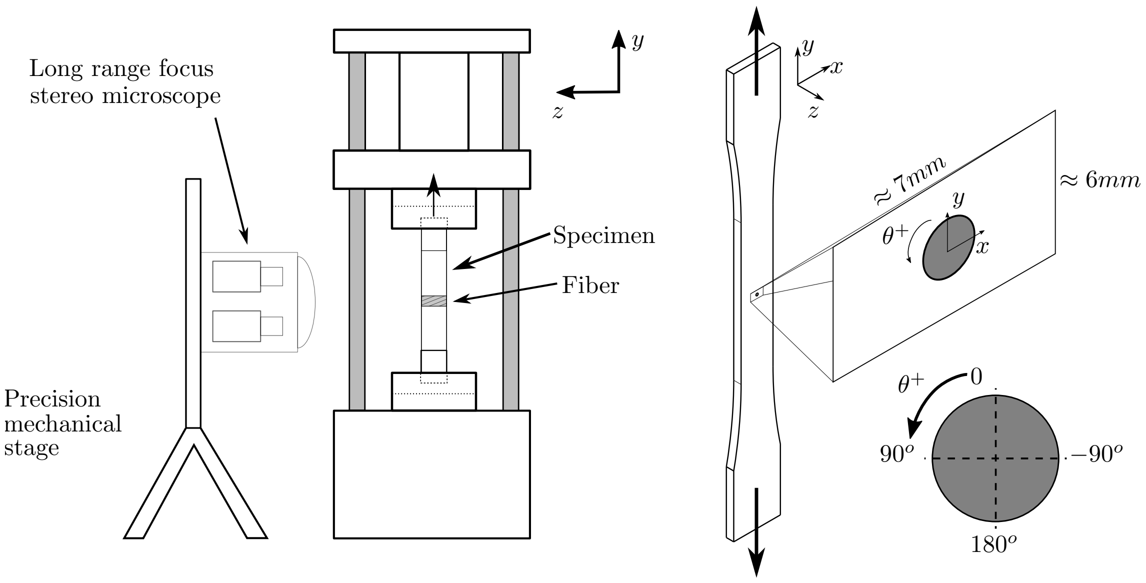

(a) (b)

Figure 5.2 **(a)** Schematic representation of the 3-axis high precision linear stage supporting two cameras with a long range focus stereo microscope used to track the fiber during the test. The optical setup was installed in front of the electromechanical testing machine. **(b)** Isometric view of the specimen. The arrows show the tensile direction. The fiber is visible as a circle in the middle of the specimen. The cameras observe the specimen in the xy plane

DIC software parameters

Subset size The commercial package VIC3D [60] used in this work is based on a subset based approach. The subset size is conditioned by the paint dot size since the subset should contain numerous dots to yield accurate DIC results [59]. A large subset would not be adequate to capture strain gradients around small geometrical features, such as the fiber. A subset as small as possible was therefore sought. The subset sizes selected for each specimen are provided in Table 5.2, as well as the main DIC parameters (subset, step and correlation type) used for each test.

Step size The step size is defined as the spacing of the points that are analyzed during correlation. The displacement of the pixels in between is obtained by interpolation. A step of 2 means that one pixel out of two is tracked, with the displacement of the others being interpolated [60]. A step of size 2 was chosen to minimize the area lost around the crack and to minimize smoothing effects around discontinuities created by interpolation [56]. An optimized 8-tap interpolation scheme was used to obtain sub-pixel interpolation. Lagrangian strains were computed using a filter size of 15 pixels to avoid over-smoothing the experimental data while computing strains.

Several images of an unloaded speckled specimen were taken to evaluate the noise of the experimental setup. Experimental noise is mostly due to the acquisition hardware and environmental conditions [101]. These parameters led to displacement variations inferior to 10^{-5} mm and strain variations lower than 0.02%.

The stereo-microscope was adjusted and calibrated for distortion and in-plane and out-of-plane displacement measurements before each test. The focus, aperture, and lighting setup were first adjusted on both cameras. The angle between cameras, called the stereo-angle, was then centered so that both cameras remained in focus and centered on the same area even when the zoom was changed. The setup was also calibrated for distortion because

Table 5.2 Subset, step, and type of correlation (direct or incremental) parameters selected for each analysis

Matrix	Fiber	Subset	Step	Correlation type
Epoxy	PTFE	81	2	Direct
Modified epoxy	PTFE	81	2	Direct
Epoxy	Galvanized steel	85	2	Direct
Modified Epoxy	Galvanized steel	55	2	Direct

of the high magnification lens used in the stereo-microscope. Eight pairs of stereo-imaged flat speckle patterns printed on a glass slide provided by Correlated Solutions were taken as the speckle pattern was shifted using the 3-axis high-precision linear stage carrying the stereo-microscope. The Distortion Correction function available in VIC3D was then used to compute the distortion and correct it for each test. A calibration target printed on a glass slide, provided by Correlated solutions, was then used to determine the values of the extrinsic (e.g., stereo angle, distance between cameras) and intrinsic (e.g., sensor center, focal length, skew) setup parameters [60]. The detailed values and results for each calibration are also provided in the additional dataset [96].

We present the results for only one specimen for each matrix-fiber couple since we managed to achieve a single successful test after numerous attempts.

5.5 RESULTS

5.5.1 Interface bonding strength effect on macroscopic behavior

Table 5.3 presents the maximum stress ($\bar{\sigma}_{\text{max}}$) and strain at failure ($\bar{\varepsilon}_{\text{rupture}}$) values reached while testing each fiber/matrix couples tensile test specimen. The stress ($\bar{\sigma}_{\text{crack}}$) and strain ($\bar{\varepsilon}_{\text{crack}}$) values at which it is possible to visually distinguish the inter-facial crack between the matrix and fiber are also shown. Final rupture was provoked by a crack growing out of the fiber/matrix interface through the matrix. It appears that a stronger bonding between matrix and fiber (epoxy with galvanized steel or modified epoxy with galvanized steel) significantly improves the global strain at specimen rupture, as $\bar{\varepsilon}_{max}$ is higher for the specimens with galvanized steel fibers (from 7.5% to 9.8% for epoxy and from 6.5% to 8.8% for the modified epoxy). The galvanized steel fiber bonding strength with both matrices thus appears to be higher than the PTFE one.

5.5.2 Strain evolution

Results for PTFE fiber/epoxy, galvanized steel/epoxy, PTFE/modified, and galvanized steel /modified epoxy composites are shown in Figures 5.3, 5.4, 5.5 and 5.6, respectively. Contour plots for ε_x and ε_y strains, as well as the out-of-plane displacements U_z are presented for each fiber/matrix couple, for three different time steps: before any damage was visible, at the onset of inter-facial damage and at the onset of crack kinking. The ε_x, ε_y and U_z contour plots are shown in the non-deformed coordinate system and each pixel is colored according to the magnitude of ε_x, ε_y or U_z. VIC3D's Rigid body motion removal function was used since the stereo-microscope was translated to track the fiber during the test [60]. The reference coordinate axis is provided in Figure 5.2.

For the purposes of this work, a pixel's tracking is considered lost when the confidence region for that pixel is higher than an arbitrary threshold of 0.050 pixels [56]. Untracked pixels cease to be colored (see Figures 5.3, 5.4, 5.5 and 5.6).

Before the onset of damage

The maximum of ε_y was localized at the top and bottom of the fibers' interface for all specimens (Figures 5.3a-ε_y, 5.5a-ε_y, 5.6a-ε_y), except for the galvanized steel/epoxy (Figure 5.4a-ε_y) composite for which the maximum was located at the bottom of the fiber only. As the load increased, ε_y built up in the -45^o, 45^o, -135^o and 135^o areas near the interface, forming a cross shape around the fiber (Figures 5.3b-ε_y, 5.4b-ε_y, 5.5b-ε_y, 5.6b-ε_y). It can also be seen that ε_y localized at the top (0^o) and bottom (180^o) areas in the interface. The maximum of ε_y is about 4 to 5 times higher than the global strain $\bar{\varepsilon}$ applied for all specimens.

Significant differences in the ε_x field can be observed between PTFE and galvanized steel fiber specimens. On one hand, ε_x appears to be positive in the fiber's visible surface and matrix around it for the galvanized steel fibers specimens. Strains in the matrix away from the fiber seem to be 1 % lower than that in the fiber (Figure 5.4a-ε_x, 5.6a-ε_x).

On the other hand, ε_x is different inside the fiber's visible surface area and its vicinity for the PTFE fibers composites. Figures 5.3a-ε_x and 5.5a-ε_x show that ε_x is tensile on the transverse edges of the PTFE fibers (less than 1% strain along x) while it is compressive in the matrix (about -3% strain along y). The fiber appears to be compressed by the matrix along the transverse direction for the PTFE specimens, while it does not appear to be compressed by the matrix for the galvanized steel fiber composite specimens.

Table 5.3 Maximum stress ($\bar{\sigma}_{\text{max}}$) and strain ($\bar{\varepsilon}_{\text{rupture}}$) values reached while testing each specimen and the stress ($\bar{\sigma}_{\text{crack}}$) and strain ($\bar{\varepsilon}_{\text{crack}}$) values at which it is possible to visually distinguish the inter-facial crack between the matrix and fiber. Galvanized steel fiber specimens significantly improved the strain at rupture (by 2.3% in both cases)

Matrix	Fiber	Bonding	$\bar{\sigma}_{\text{crack}}$ (MPa)	$\bar{\sigma}_{\text{max}}$ (MPa)	$\bar{\varepsilon}_{\text{crack}}$ (%)	$\bar{\varepsilon}_{\text{rupture}}$ (%)
Epoxy	PTFE	None	25.0	26.5	3.0	7.5
Modified epoxy	PTFE	None	18.9	20.6	2.7	6.5
Epoxy	Galvanized steel	Strong	26.3	26.8	3.4	9.8
Modified epoxy	Galvanized Steel	Strong	17.3	21.8	2.7	8.8

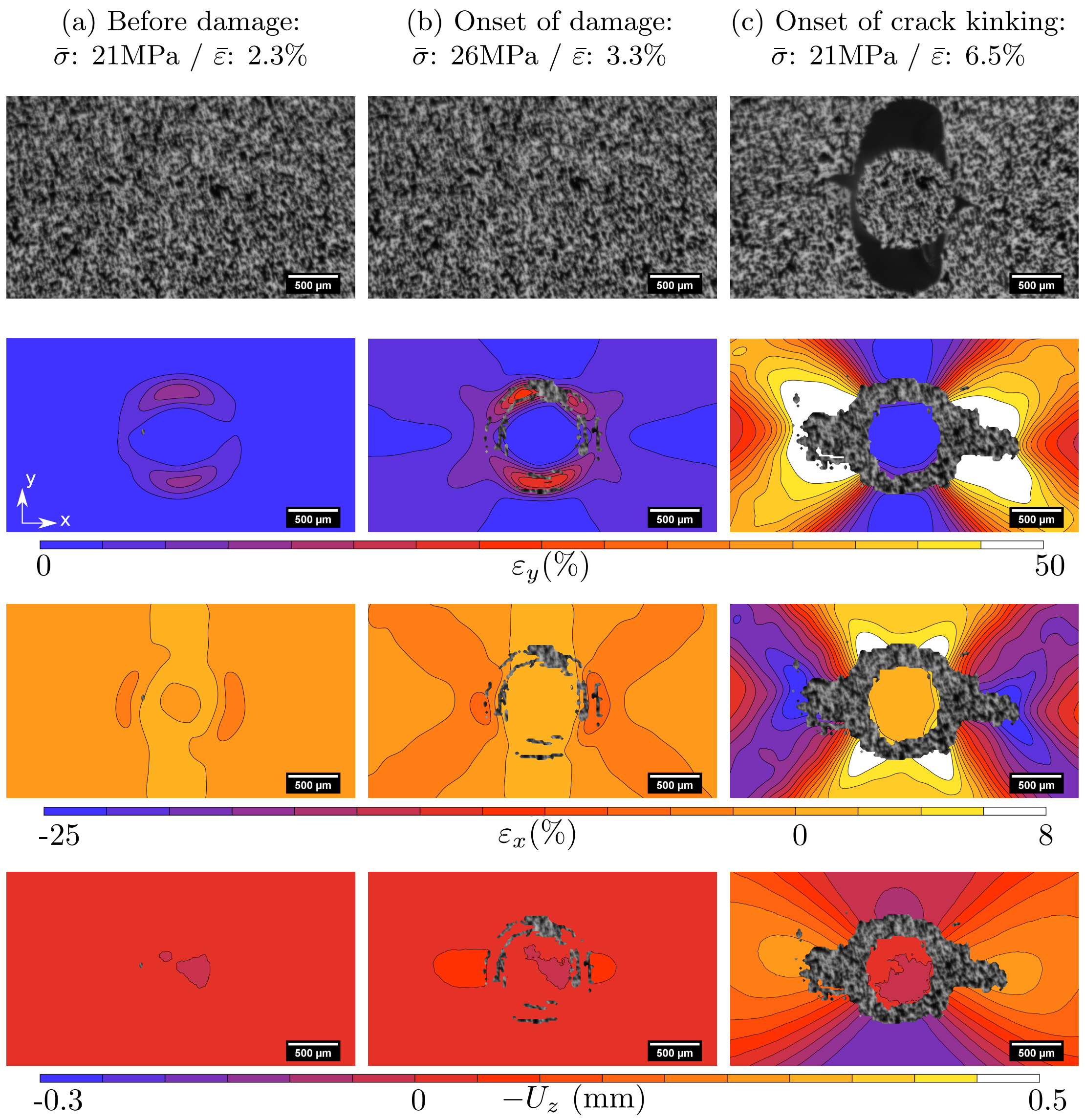
(a) Before damage:
$\bar{\sigma}$: 21MPa / $\bar{\varepsilon}$: 2.3%

(b) Onset of damage:
$\bar{\sigma}$: 26MPa / $\bar{\varepsilon}$: 3.3%

(c) Onset of crack kinking:
$\bar{\sigma}$: 21MPa / $\bar{\varepsilon}$: 6.5%

Figure 5.3 **PTFE fiber/epoxy** composite loaded in tension in the y direction. Column (a) includes images taken before an inter facial crack appeared between the fiber and matrix. Column (b) includes images taken at onset of inter-facial cracking. Column (c) refers to an image taken at the apparition of one or several cracks growing in the matrix out of the inter-facial crack. The global stress and strain values for each column are provided at the very top of the figure. The first row shows the raw images. The second and third rows present the strain contour plots in the y and x directions, and the last row presents the out-of-plane displacement U_z

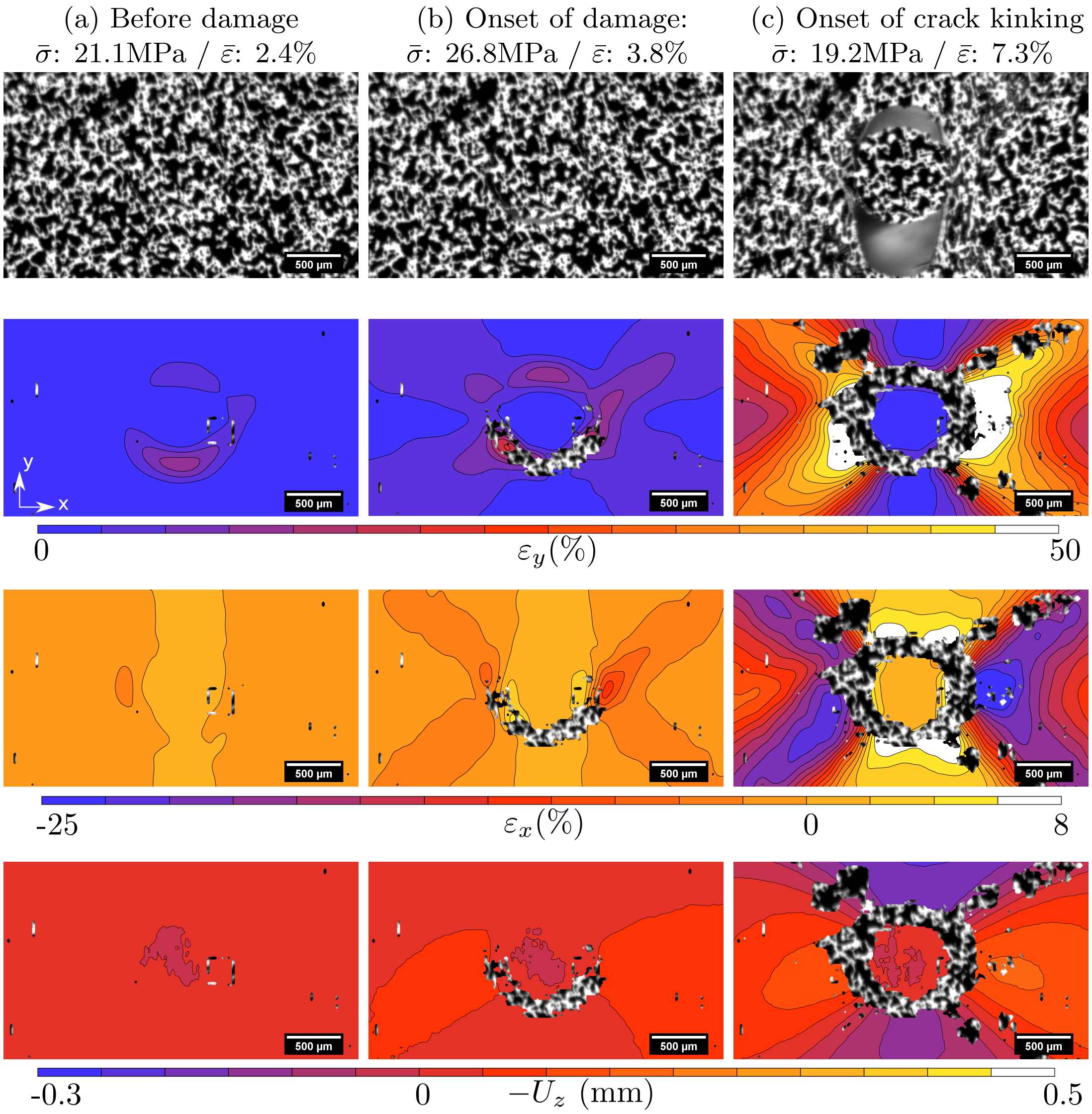
(a) Before damage $\bar{\sigma}$: 21.1MPa / $\bar{\varepsilon}$: 2.4%

(b) Onset of damage: $\bar{\sigma}$: 26.8MPa / $\bar{\varepsilon}$: 3.8%

(c) Onset of crack kinking $\bar{\sigma}$: 19.2MPa / $\bar{\varepsilon}$: 7.3%

Figure 5.4 **Galvanized steel fiber / epoxy** composite loaded in tension in the y direction. Column (a) refers to an image taken before an inter facial crack appeared between the fiber and matrix, column (b) refers an image taken at the onset of inter facial crack and column (c) refers to an image taken at the apparition of one or several cracks growing in the matrix out of the inter facial crack. The global stress and strain values for each column are provided at the very top of the figure. The first row shows the raw images, the second and third rows present the strain contour plots in the y and x directions while the last row presents the out of plane displacement U_z

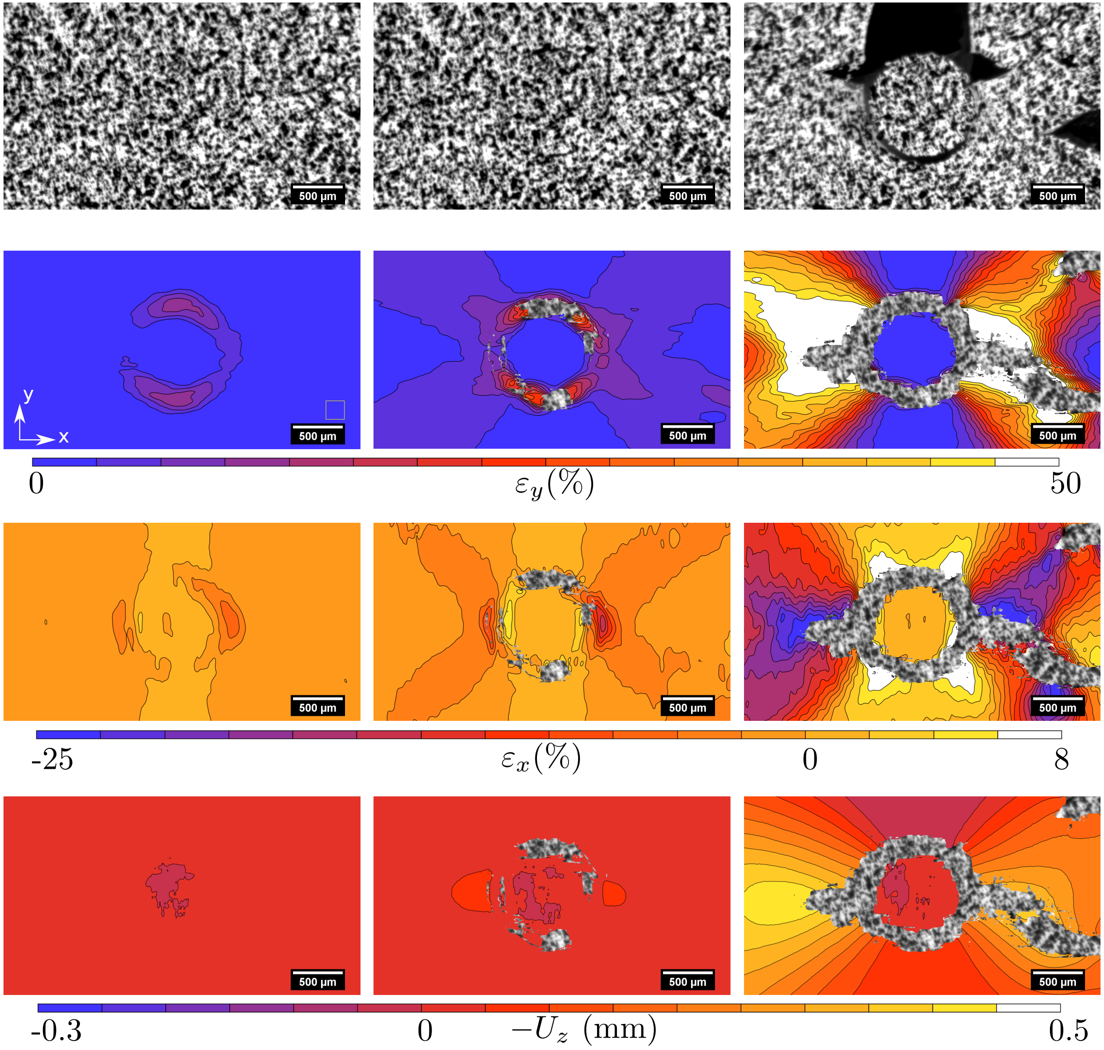

(a) Before damage: $\bar{\sigma}$: 15.1MPa / $\bar{\varepsilon}$: 1.8%

(b) Onset of damage: $\bar{\sigma}$: 20.1MPa / $\bar{\varepsilon}$: 3%

(c) Onset of crack kinking: $\bar{\sigma}$: 16.4MPa / $\bar{\varepsilon}$: 5.5%

Figure 5.5 **PTFE fiber/epoxy modified with elastomer adduct** composite loaded in tension in the y direction. Column (a) includes images taken before an inter-facial crack appeared between the fiber and matrix. Column (b) includes images taken at the onset of inter-facial cracking. Column (c) includes images taken at the apparition of one or several cracks growing in the matrix out of the inter facial crack. The global stress and strain values for each column are provided at the very top of the figure. The first row shows the raw images. The second and third rows present the strain contour plots in the y and x directions and the last row presents the out-of-plane displacement U_z

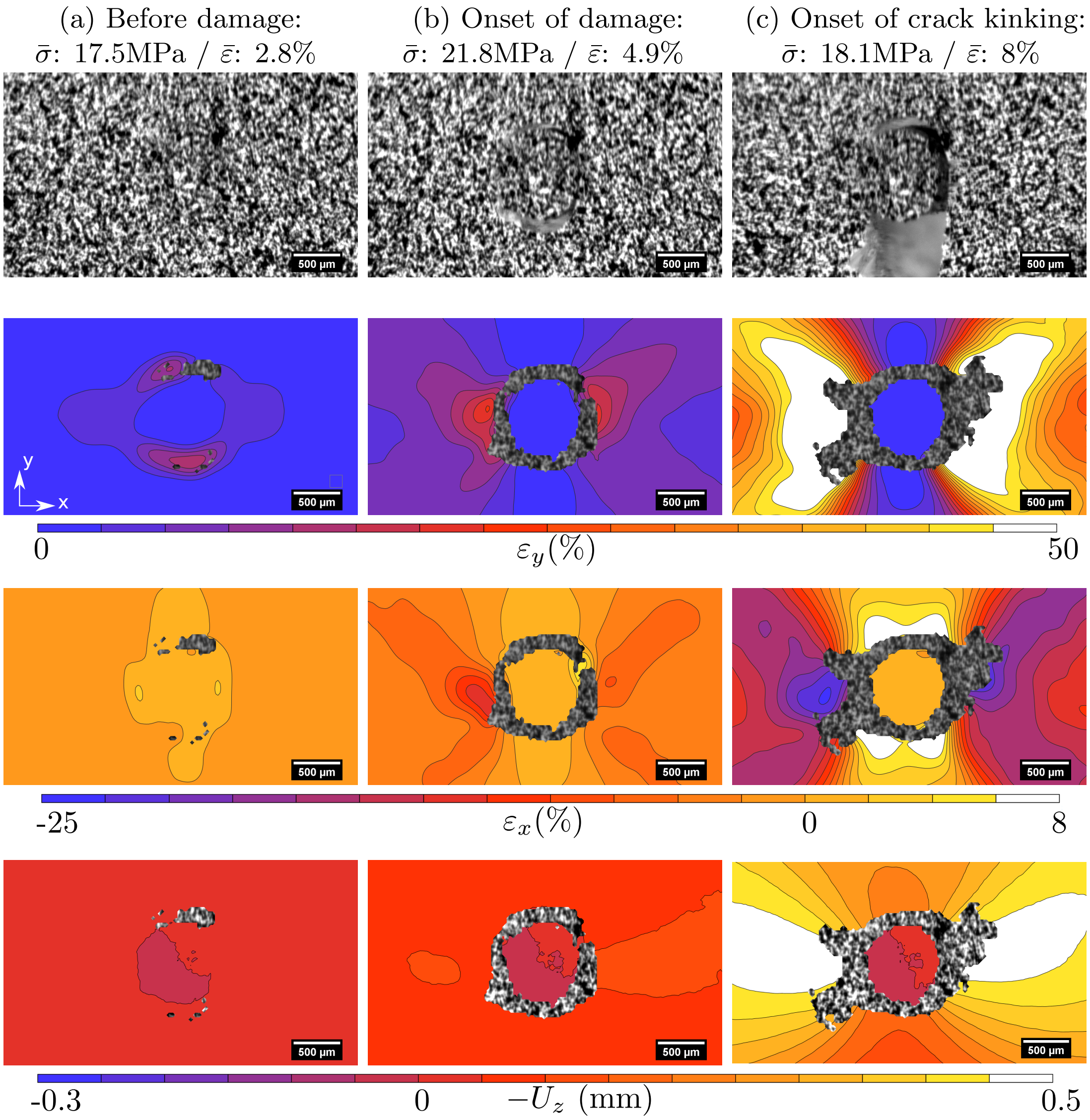

Figure 5.6 **Galvanized steel fiber/epoxy modified with elastomer adduct** composite loaded in tension in the y direction. Column (a) includes images taken before an inter-facial crack appeared between the fiber and matrix. Column (b) includes images taken at the onset of inter-facial cracking. Column (c) includes images taken at the apparition of one or several cracks growing in the matrix out of the inter facial crack. The global stress and strain values for each column are provided at the very top of the figure. The first row shows the raw images. The second and third rows present the strain contour plots in the y and x directions, and the last row presents the out-of-plane displacement U_z

Figures 5.3b-ε_x, 5.4b-ε_x, 5.5b-ε_x and 5.6b-ε_x also show that ε_x grew in a shape similar to that of ε_y. The transverse stress develops into a cross shape similar to that observed for the ε_y strain.

The shear strain, not shown here (available in the dataset [96]), was maximal at -45^o and 135^o of the interface and was about twice the global strain (from 1 to 6%) for all specimens. The minima were located at 45^o and -135^o and the value was about the opposite of the shear strain at the 135^o and -45^o. Note that DIC tracking for pixels in the interface area was lost before a crack was visible anywhere in the AOI, for all specimens (Figures 5.3b, 5.4b, 5.5b and 5.6b). The density of pixels for which tracking was lost is higher in the top (0^o) and bottom (180^o) areas of the interface than in the left and right areas.

From the onset of damage until the onset of crack kinking

An inter-facial crack was clearly visible around the fiber for all specimens (Figures 5.3b, 5.4b, 5.5b and 5.6b). At this point, all damage appeared to be located at the fiber/matrix interface and no crack was yet growing in the matrix. Damage initiated with fiber debonding with an inter-facial crack growing on the top or the bottom area of a fiber (*i.e.,* 0^o or 180^o), where ε_y was previously maximum. The inter-facial crack appeared in the top area for the PTFE/epoxy and PTFE/modified epoxy specimens (Figures 5.3b and 5.5b), in the bottom area for the galvanized steel/epoxy specimen (Figure 5.4b) and simultaneously in the top and bottom areas for the galvanized steel/modified epoxy specimen (Figure 5.6b).

Figures 5.3c, 5.4c, 5.5c and 5.6c show that the inter-facial cracks steadily grew around the fiber, until total fiber debonding. The inter-facial crack also widened at the bottom and top areas for the PTFE/epoxy and galvanized steel/epoxy specimens (Figures 5.3c, 5.4c). It only appeared to widen in the top area for the PTFE/modified epoxy composite (Figure 5.5c) and only in the bottom area for the galvanized steel/modified epoxy composite (Figure 5.6c). At this point, the inter-facial cracks kinked into the matrix; cracks growing on the edges of the inter-facial crack also appeared in the matrix. The figures also show that the maxima of ε_y and ε_x localized at the tip of the kinking crack (or cracks), in all cases.

The local strain measured within the fiber might not capture the high strain gradient existing in the fiber. Displacement results, available in the additional data package [96], were measured every other pixel. Displacement values of pixels in between measurement pixels were interpolated. Lagrangian strains were, however, computed using a filter size of 15 pixels, which is the smallest possible value in the VIC3D software. Consequently, strain values might not be quantitatively representative of high gradient strains existing in the fiber.

From crack kinking to specimen failure

The mechanism by which the inter-facial crack kinked into the matrix appears to be different for the galvanized steel fiber specimens and PTFE fiber specimens. In the case of PTFE specimens, ε_y and ε_x were located at the 90^o and -90^o positions of the interface (Figures 5.3b and 5.5b). The crack was then only growing at the interface. The minimum out-of-plane displacement was also located in that same area, meaning that striction occurred in the left and right areas around the fiber. The contraction of material due to high strains and striction eventually triggered the apparition of cracks in the matrix, at 90^o and -90^o, as shown in Figures 5.3c and 5.5c.

The damage process was similar in the galvanized steel specimens, except for the area where the crack kinked out of the interface. In this case, the crack appeared on the sites where the shear strain ε_{xy} appeared to be maximal, around 45^o, -45^o, 135 or -135^o, as shown in Figures 5.4c and 5.6c.

The kinking cracks eventually grew transversely through the whole specimen and triggered its complete failure.

5.5.3 Virtual extensometers

Figure 5.7 plots an averaged strain near the fiber/matrix interface that would be measured by a virtual extensometer as a function of the applied global strain $\bar{\varepsilon}$. The local strain, ε^l, was computed by subtracting the displacement of two pixels and by dividing it by their original distance. The selected points were about one subset away from the fiber/matrix interface.

Figure 5.7a shows the local averaged strain results computed with the virtual extensometer aligned along the x direction in the matrix near the interface, $\varepsilon^l_{x_m}$. This virtual extensometer measured the strain applied by the matrix on the fiber along the x direction. On the x axis, the selected points for the virtual extensometers appear to move closer one to another in the case of the PTFE specimens, during the whole test. For $\bar{\varepsilon} = 2\%$, specimens with PTFE fibers exhibit a higher compression applied on the fiber by the matrix. The compression is lower for specimens reinforced with a galvanized steel fiber. PTFE is two orders of magnitude more compliant than galvanized steel, which explains this difference.

Figure 5.7b shows the virtual extensometer aligned along the y direction in the matrix near the interface, $\varepsilon^l_{y_m}$, which provides insights on the inter-facial crack opening in the y direction. Results show that debonding occurred sooner and at a faster rate for the PTFE/modified epoxy couple, when compared to the debonding of other specimens. At a global strain of 2%, $\varepsilon^l_{y_m}$ already reached 11% for the PTFE/modified epoxy specimen, while it was only 2 to

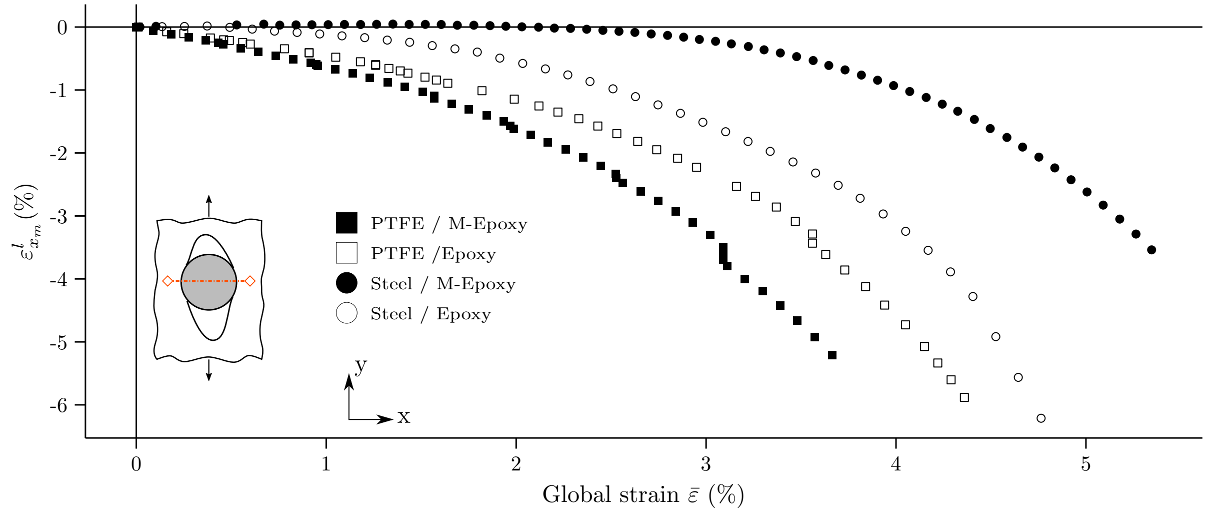

(a)

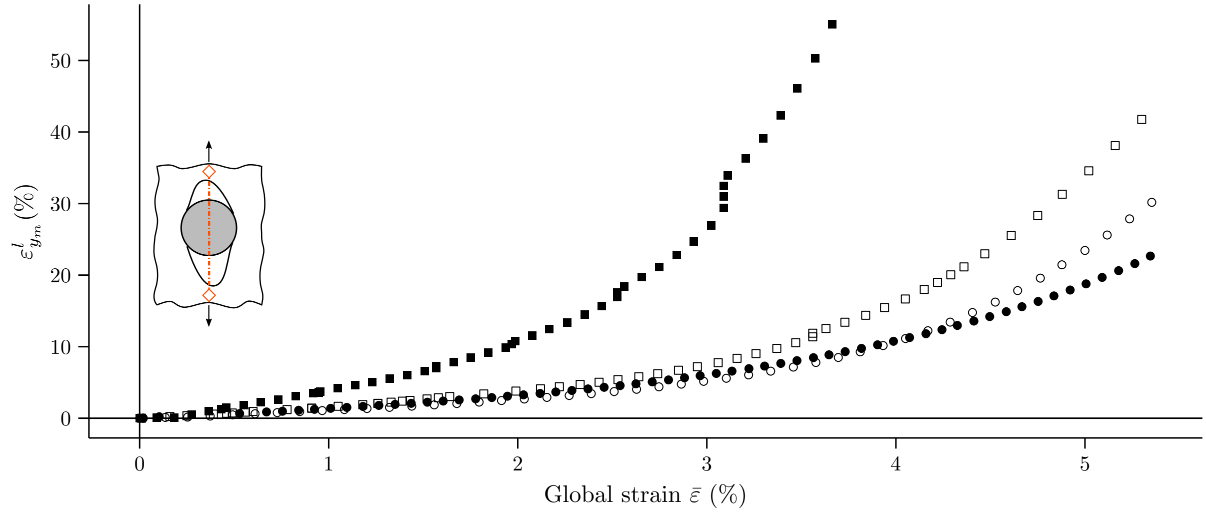

(b)

Figure 5.7 $\varepsilon^{l}_{x_m}$ and $\varepsilon^{l}_{y_m}$ are shown as a function of $\bar{\varepsilon}$ for the four couples of materials tested. $\varepsilon^{l}_{x_m}$ and $\varepsilon^{l}_{y_m}$ were obtained respectively by applying a virtual extensometer around the fibre/matrix interface in the x and y directions. **(a)**: $\varepsilon^{l}_{x_m}$ measures the strain applied by the matrix on the fiber along the x direction. The initial length of the extensometer is about $\approx$ 1.2mm. The compression applied by the matrix became higher at lower $\bar{\varepsilon}$ for specimens with a PTFE fiber. **(b)**: $\varepsilon^{l}_{y_m}$ measures the strain applied by the matrix on the fiber and the opening of the inter-facial fiber, along the y direction. The initial length of the extensometer is about 1.4mm. Specimens with a PTFE fiber appear to debond faster along the y direction for smaller values of $\bar{\varepsilon}$

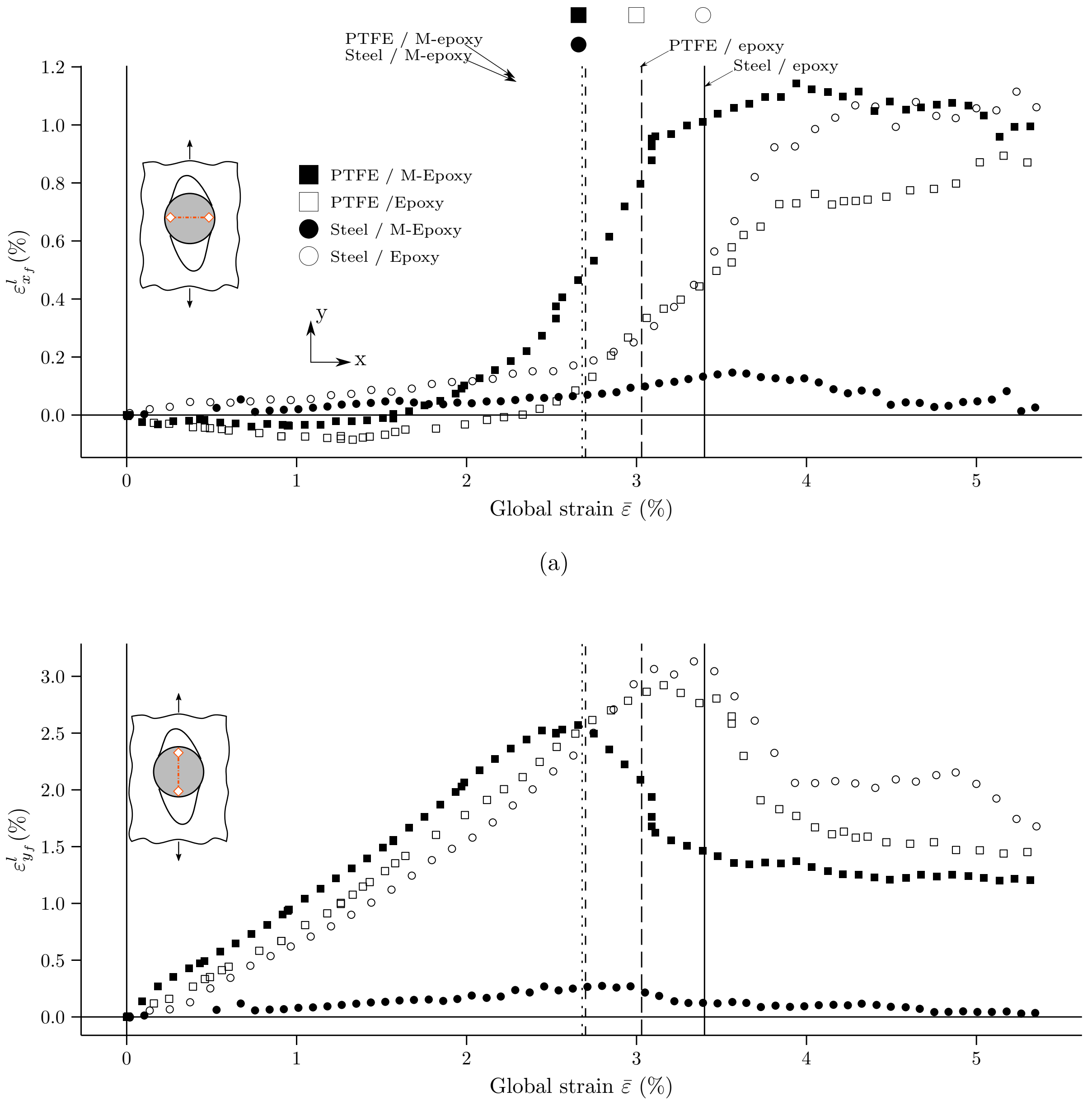

(a)

(b)

Figure 5.8 $\varepsilon^l_{x_f}$ and $\varepsilon^l_{y_f}$ are shown as a function of $\bar{\varepsilon}$ for the four couples of materials tested. $\varepsilon^l_{x_f}$ and $\varepsilon^l_{y_f}$ were obtained respectively by applying a virtual extensometer inside the fibre in the x and y directions. **(a)**: $\varepsilon^l_{x_f}$ measures the strain inside the fiber, along the x direction. The initial length of the extensometer is about 0.7 mm. The evolution of $\varepsilon^l_{x_f}$ appears to be linked with the growth of the inter-facial crack. **(b)**: $\varepsilon^l_{y_f}$ measures the strain along the y direction inside the fiber. The initial length of the extensometer is about 0.7mm. $\varepsilon^l_{y_f}$ grows for all specimens until the appearance of an inter-facial crack. $\varepsilon^l_{y_f}$ then drops slightly and remains stable on a plateau level

3% for the other specimens. Specimens with a steel fiber appear to debond slower than the specimens with PTFE.

Figure 5.8a plots the strain measured by a virtual extensometer setup inside the fiber, $\varepsilon^l_{x_f}$, as a function of the global strain. The figure shows that, for a global strain lower than 2%, the steel fibers experienced tensile strains of 0.1%, while the PTFE fibers were submitted to compressive strains. For $\bar{\varepsilon} > 2\%$, $\varepsilon^l_{x_f}$ increased with a rising applied strain, for all specimens. It can be seen, however, that the increase is much less pronounced for the composite with a PTFE fiber and modified epoxy. $\varepsilon^l_{x_f}$ increased until it reached a plateau. Once the first inter-facial crack was monitored (identified by a vertical dotted line in Figure 5.8a). $\varepsilon^l_{x_f}$ then remained stable for all specimens at around 1%, until the end of the test.

Figure 5.8b plots the vertical virtual extensometer inside the visible surface area of the fibers, $\varepsilon^l_{y_f}$, as a function of $\bar{\varepsilon}$. The figure shows that fibers were, overall, submitted to a tensile strain field that increased linearly with the applied strain $\bar{\varepsilon}$. It should be noted that $\varepsilon^l_{y_f}$ was considerably lower in the galvanized steel/modified epoxy sample than in the others. $\varepsilon^l_{y_f}$ then reached a maximum value close to the load for which a transverse crack was detected in the specimen. It is interesting to note that the maximum $\varepsilon^l_{y_f}$ occurred at around the same value for the specimens made of pure epoxy (about 3% local strain at 3.4% global deformation). Then, once the first inter-facial crack was detected, $\varepsilon^l_{y_f}$ decreased steadily until it reached a plateau. Further observation of the results from the dataset [96] (similar to those presented in Figures 5.3b, 5.4b, 5.5b and 5.6b) around these time steps shows, for all specimens, that the drop in the strain measured by the virtual extensometer is linked to the growth of the inter-facial cracks.

5.5.4 Out-of-plane evolution

Figures 5.3-U_z, 5.4-U_z, 5.5-U_z and 5.6-U_z show contour plots of the out-of-plane displacement for the four configurations studied. The out-of-plane displacements are presented relative to the fiber, for which the out-of-plane displacements were set to 0. U_z was below the noise level everywhere in the observed area for $\bar{\varepsilon} \leq 2\%$. The out-of-plane displacement between the fiber and matrix was not yet above the noise level for all specimens. Once the average stress levels shown in Figures 5.3a-U_z, 5.4a-U_z, 5.5a-U_z and 5.6a-U_z were reached, the difference in out-of-plane displacement between the matrix surrounding the interface and the fiber became significant (higher than 0.03mm). The figures show that the out-of-plane displacement behavior is divided into three areas growing at different rates: above/below the fiber and to the left/right of the fiber. At the onset of damage (Figures 5.3b-U_z, 5.4b-U_z, 5.5b-U_z and 5.6b-U_z), the minimum out-of-plane displacement was localized on the left/right sides of the

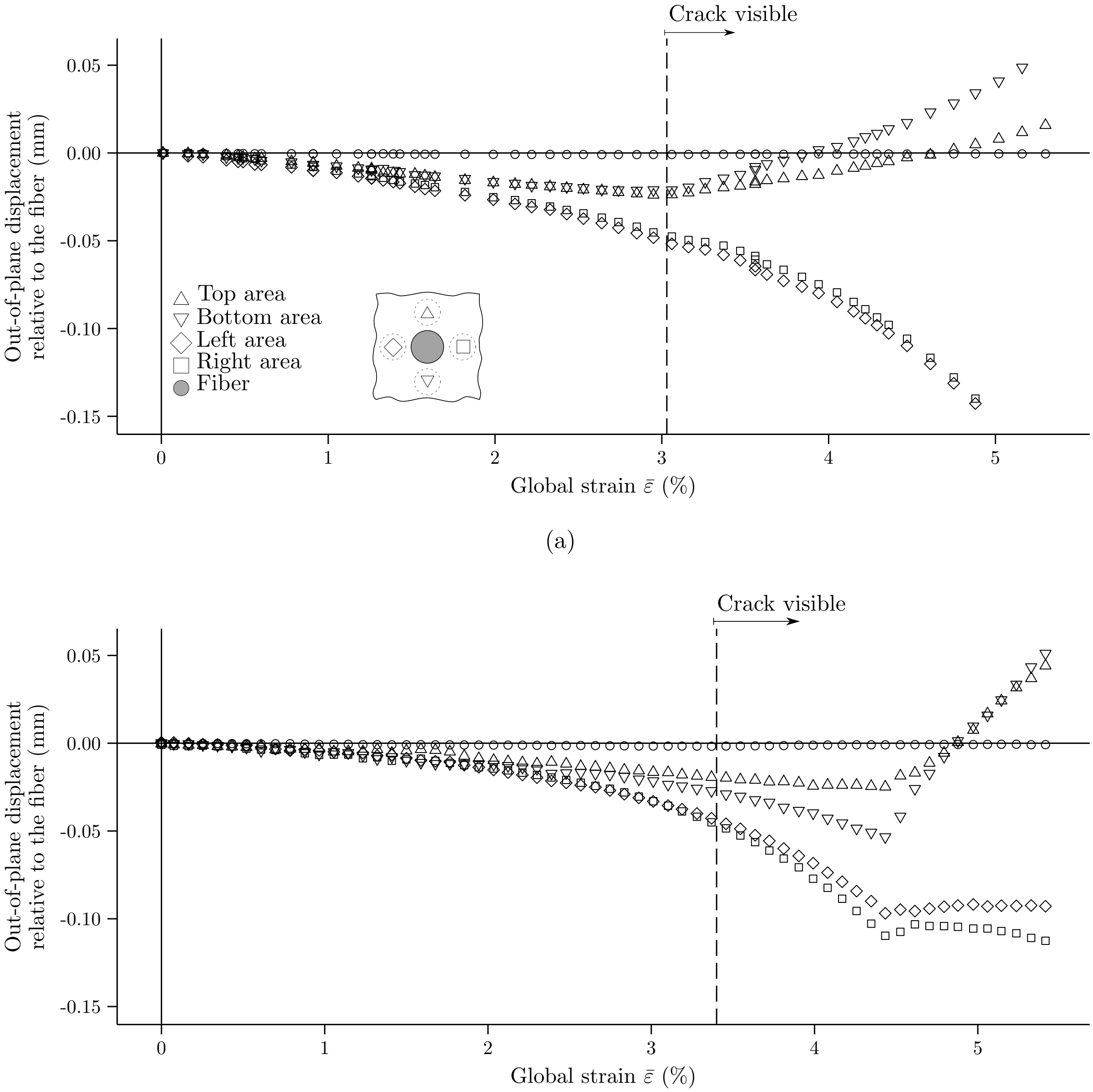

(a)

(b)

Figure 5.9 Out-of-plane displacement of the fiber and areas surrounding it for **PTFE/epoxy** and **galvanized steel/epoxy** specimens. The pixels from four circular areas directly on top, bottom, left, and right sides of the fiber were selected. Each area's center is about a subset away from the interface and has a diameter of 200µm. The out-of-plane displacement for each area is plotted with respect to the out-of-plane displacement from the pixels in the fiber. Plot **(a)** shows results for the **PTFE/epoxy** specimen while plot **(b)** shows the results for the **galvanized steel/epoxy** specimen. A dashed line is added on each plot to show the global strain level at which the crack becomes visible (as provided in Table 5.3) fiber. The out-of-plane displacements of the above/below areas were still negligible. Towards the end of the test, when the inter-facial debonding crack started kinking into the matrix (Figures 5.3c-U_z, 5.4c-U_z, 5.5c-U_z and 5.6c-U_z), the minimum out-of-plane displacement was still located in the left and right sides of the fiber, near the lateral cracks. The out-of-plane displacements of those areas were lower than those of the fiber, in all cases. The out-of-plane displacements of the above and below areas were lesser than those of the fiber in the case of the modified epoxy specimens. They were higher however than those of the fiber in the case of epoxy specimens.

Figures 5.9a and 5.9b present quantitative measurements of the out-of-plane displacement relative to the fiber, of four areas around the fiber, for the PTFE/epoxy specimen and the galvanized steel/epoxy specimen, respectively. Circular areas having a diameter of 200µm about half a subset away from the interface on the top, bottom, left, and right sides of the fiber were used to obtain each area's out-of-plane displacement. The dashed vertical lines in Figures 5.9a and 5.9b show the global strain values at which an inter-facial debonding crack was visible first in the top and/or bottom areas (see Table 5.3). The left and right-hand sides' out-of-plane displacements steadily decreased during the whole test until a crack grew in their vicinity. The out-of-plane displacements in areas above and below the fiber also appeared to decrease, at a slower rate than the left and right-hand side areas, for both specimens. The inter-facial crack appeared first in top and bottom areas for the PTFE/epoxy specimen (Figure 5.9a), which resulted in an immediate change in the slope of the bottom and top out-of-plane displacements. At around 4% global strain, the top and bottom areas were rising above their initial height. A change in the out-of-plane displacement rate in all areas maye be seen at the global deformation level at which the crack became visible. However, the left and right areas' out-of-plane displacements decreased at a faster rate once an inter-facial crack appeared. For the galvanized steel/epoxy specimen (Figure 5.9b), the change in the out-of-plane displacement rate of the top and bottom areas was delayed and only occurred at 4.2% global strain. The crack was visually noticeable at around 3.4% global strain on the bottom interface only. It seems that at 4.2% global deformation, the bottom inter-facial crack is 100µm wide and reached the 90^o to -90^o edges. No inter-facial crack was yet visible on the top of the interface. Figure 5.4c shows the specimen with the bottom crack visible at a global strain of $\bar{\varepsilon} = 7.3\%$. Note that a crack in the top area also started growing.

In Figure 5.10, the out-of-plane displacement is also plotted along the y direction as a function of position along the dotted line shown on the figure for galvanized steel/epoxy and PTFE/epoxy specimens. This profile line was extracted from the out-of-plane displacement contour plots presented in Figures 5.4-U_z and 5.3-U_z. Before any damage appeared (Figures 5.4-a and 5.3-a), the matrix out-of-plane displacement is smaller than the fiber's in both cases. At the onset of intefacial cracking (Figures 5.3-b and 5.4-b), DIC tracking sharply degraded for pixels in the interface area due to high strains and to the crack interfering with the subset's original patterns. The tracking was lost at the top and bottom fiber areas for the PTFE/epoxy specimens, while the tracking was lost in the bottom area only for the galvanized steel/epoxy specimen because of the inter-facial crack opening. Figure 5.10 shows that the out-of-plane displacement is smaller for the galvanized steel/epoxy specimen, which means that it experiences more striction than the PTFE/epoxy specimen. At the onset of the inter-facial cracking into the matrix (Figures 5.4-c and 5.3-c), the inter-facial crack is already large in the top and bottom fiber areas. The out-of-plane displacement of the top and bottom areas is now above the fiber for both specimens. Those areas are next to free surfaces, because of the inter-facial crack opening.

Results for the specimens with a modified epoxy matrix are similar and are available in the attached dataset [96].

5.5.5 Fiber/matrix bonding

Figure 5.11 presents the contour plots of the confidence margins for three different time-steps during the galvanized steel fiber/epoxy specimen test. A value of zero means a perfect match for the pixel's subset; higher values suggest the appearance of new surfaces in the observed region (*i.e.* a crack) [56]. Figures 5.11-a and 5.11-b were taken before any crack was visible during the test. In the fiber/matrix interface area, it is assumed that $\mathcal{C}$ can be used to identify the inter-facial debonding crack path.

Figure 5.11-a shows that cracks were clearly visible for an overall strain of $\bar{\varepsilon} = 1.2\%$ for the galvanized steel/epoxy specimen. The areas where $\mathcal{C}$ is maximal are the areas where the crack starts growing later on during the test. It is thus possible to predict the crack path using $\mathcal{C}$ before damage is even visible.

While the crack initiation path can be assumed using the $\mathcal{C}$ variable for a global applied strain of $\bar{\varepsilon} = 1.2\%$, it becomes barely visible on the camera image later on during the test for $\bar{\varepsilon} = 3.4\%$ (Figure 5.4-a).

5.6 DISCUSSION

5.6.1 Experimental limitations

The limitations of the experimental setup which are presented here, are mainly related to the observation equipment. The image obtained by the stereo-microscope cannot be completely

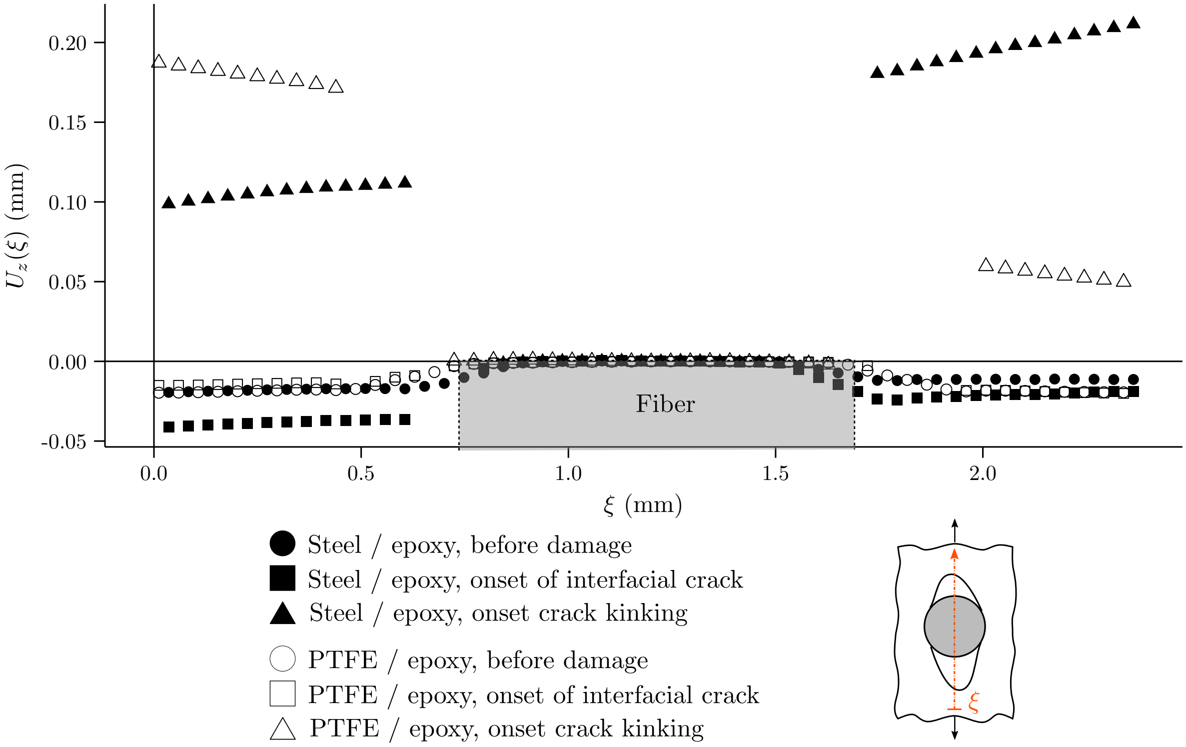

Figure 5.10 Out-of-plane displacement along a vertical line as a function of the position on the line, for the galvanized steel/epoxy and PTFE/epoxy specimens. The out-of-plane displacement is presented at the same time steps presented in Figures 5.3 and 5.4: before any damage, at the onset of the inter-facial crack and at the onset of inter-facial crack kinking. The variable ξ represents the position along the profile line. The out-of-plane displacement relative to the fiber is represented by $U_z(\xi)$. The figure shows that there is a significant difference in out-of-plane displacement between the fiber and the top and bottom areas in the fiber's vicinity. At the onset of crack kinking, the difference is about 0.15mm

used for the DIC analysis. The edges of the acquired images (about 6 mm × 7 mm) show optical distortion, which reduces the region of interest. The region of interest was always centered on the fiber and is about 3 mm × 3.5 mm. The out-of-plane measurements are also limited by the setup's depth-of-field (about two millimeters). Pixels having large out-of-plane displacements are gradually lost as they leave the plane-of-focus. Out-of-plane inter-facial tunnelling (crack growth along the fiber) is reported to happen during debonding along the fiber [9, 27]. The current setup cannot capture such behavior. An alternative to the current optical setup would have been the use of a confocal stereo-microscope with a computer-controlled precision mechanical stage. Such a setup would have extended the range of out-of-plane measurements, allowing for further observations of debonding along the fiber. A computer controlled precision mechanical stage would have facilitated stitching to observe a larger region of interest without blurring the image edges.

Due to the randomness of the speckle pattern and the inability to evaluate its performance before finishing the experiment, several tests were performed for each fiber/matrix couple. Only the most successful test for each fiber/matrix couple was presented. The best projection error and confidence $\mathcal{C}$ results were used to select the most successful test.

The method presented in this publication cannot be used to investigate carbon or glass fibers in commercial FRPs. The speckle pattern features must be smaller than the material's features, such as fibers, to measure displacements with DIC. The features obtained using the available airbush were too large to investigate commercial composites. A finer speckle creation technique could be developed to address this issue.

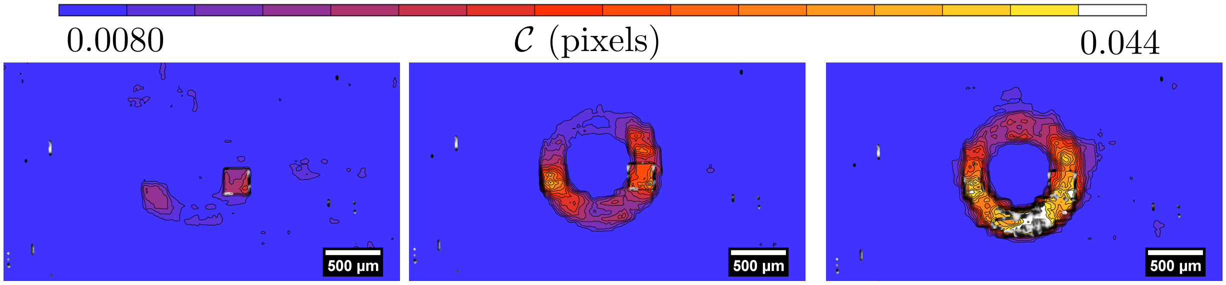

(a) $\bar{\sigma}$: 12.4MPa / $\bar{\varepsilon}$: 1.2% (b) $\bar{\sigma}$: 20.9MPa / $\bar{\varepsilon}$: 2.4% (c) $\bar{\sigma}$: 26.1MPa / $\bar{\varepsilon}$: 3.4%

Figure 5.11 Contour plots of the $\mathcal{C}$ variable for two time-steps early during a test on the **galvanized steel/epoxy** specimen. The crack growing in the interface can be detected when the global strain level is around 1.2% by using $\mathcal{C}$. The crack growth path can thus accurately be forecast

5.6.2 Advantages of the experimental setup

The out-of-plane displacement obtained by using two cameras appears to provide useful data pertaining to crack initiation and growth. In the case of PTFE specimens, a change in out-of-plane displacement is clearly noticeable around the global strain level at which the inter-facial crack appears (Figure 5.9a). In the case of galvanized steel specimens, a change in out-of-plane displacement appears once the inter-facial crack becomes visible (Figure 5.9b). The crack becomes visible at 3.7% global strain in the case of galvanized steel/epoxy, while a change in tendency of out-of-plane displacement is only visible at around 4.2% global strain.

Our assumption is that this delay may be attributed to out-of-plane crack growth along the fiber, in the case of the galvanized steel/epoxy specimen. It would be possible to validate this assumption by means of a 3D observation of the same experimental problem or via simulation.

5.6.3 DIC analysis results available online

CSV files containing the displacement, height, strain, and confidence $\mathcal{C}$ value for each pixel, at each time-step, can be exported from the DIC analysis results. The force from the load cell and the displacement from the electromechanical testing machine for each time-step are also included in the CSV file, for each specimen. Finally, a "readme PDF" file explaining the format in which the data is structured is also provided as an addition to this paper [96]. The calibration parameters obtained after calibrating each test are also included with the additional dataset. The images used for the calibration process are also provided in the additional dataset.

This data can be used exhaustively to explore the deformation field in the fiber's vicinity in order to obtain the interface fracture toughness. Doing so serves to compare simulation results against experimental data or to compare experimental results from other fiber/matrix couples against these.

5.7 Conclusion

Fibre / matrix inter-facial debonding was observed using a long range focus stereo-microscope. Accurate measurements of the displacement and strain field in the fiber's vicinity were obtained through DIC analysis for different fiber/matrix combinations. Damage occurred in three distinct steps: *(i)* initial debonding at the top and bottom of the fiber free surface; *(ii)* debonding crack growth on the transverse areas at the 45^o, -45^o, 135^o and -135^o angles around the fiber; *(iii-PTFE)* specimen failure caused by crack kinking in the matrix at the 90^o and -90^o areas, where the fiber was horizontally compressed and heavy out-of-plane striction was experienced in the case of PTFE specimens; or in the case of galvanized steel specimens, *(iii-steel)* specimen failure caused by crack kinking in the matrix at the 45^o, -45^o, 135^o or -135^o.

Damage initiated at the fiber/matrix interface at the location where an out of plane displacement difference between the fiber and matrix was the highest and where ε_y was maximal (0^o and 180^o). 3D full-field displacements in the fiber's vicinity and in the fiber's visible area were measured while damage was occurring. The results are available online as an additional package for simulation and comparison purposes.

The crack size growth and displacement fields were measured for four different fibre/matrix material couples and revealed quantitative differences. PTFE provides debonding behavior without chemical bonding. Galvanized steel provides the behavior in the case where a strong bonding between the fiber and matrix is present. Based on our results, it can be concluded that the use of *macro-fibers* and DIC is a promising technique to provide the displacement fields in the fiber's vicinity. These may subsequently be used to evaluate the inter-facial fracture toughness of a fibre/matrix couple quantitatively.

The stress state around each fiber is different in a commercial composite since the fiber volume fraction is much higher than in a single-fiber composite. This simple case can be used to calibrate inter-facial properties for a simulation of a similar problem. The results also show that damage to a single-fiber composite is related to fiber debonding along the fiber and is thus a 3D problem. Modeling of such a problem must be in 3D in order to consider all the problem's components.

CHAPTER 6 ARTICLE 2: HYBRID IMAGE PROCESSING APPROACH FOR AUTONOMOUS CRACK AREA DETECTION AND TRACKING USING LOCAL DIGITAL IMAGE CORRELATION RESULTS APPLIED TO SINGLE FIBER INTER-FACIAL DEBONDING

I. Tabiai, G. Tkachev, P. Diehl, S. Fry, T. Ertl, D. Therriault and M. Lévesque, (2018).
Submitted to: Engineering Fracture Mechanics on November 13$^{\text{nd}}$, 2018.

6.1 Abstract

Local digital image correlation is a popular method for accurate full fields displacement measurements. However, the technique struggles at autonomously tracking emerging and propagating cracks. We proposed a hybrid approach which utilizes image processing techniques in combination with local digital image correlation to autonomously monitor cracks in a mechanically loaded specimen. Our approach can extract and track crack surfaces, extract the crack path in the reference configuration and provide a volume-based visualization of the crack growth. This approach was applied to single-fiber composite experimental results with inter-facial debonding from the literature. Results quantitatively show that strong inter-facial fiber / matrix bonding leads to slower inter-facial crack growth, delays inter-facial crack growth in the matrix, requires higher loadings for crack growth and shows a specific crack path distinct from the one obtained for weak interfaces. The approach was also validated against a manual approach where a domain scientist extracts a crack using a polygon extraction tool. The method can be used on any local digital image correlation results involving damage observations.

6.2 Introduction

Digital image correlation (DIC) tracks displacement fields from images acquired during mechanical loading. DIC experimental setups are usually composed of a single digital image camera (2D DIC) or two cameras (stereoscopic DIC) and a mechanical loading setup. Displacements, measured in pixels, are determined by matching deformed images to a reference, or a previous image. Full displacement field measurements can then be used to compute strain fields. DIC has become a popular method for accurate full strain and displacement field measurements [79–83], parameter extraction [79], and damage assessment [82, 83]. Reviews by Hild et al. [102] and Pan et al. [103] provide an extensive DIC experimental mechanics applications overview.

Several DIC algorithms have been developed since the 1980s, with the subset based DIC (local DIC) [56] and finite element-based DIC (FE-based global DIC) [57] being the most widely used. Global DIC algorithms usually discretize the specified Region of Interest (ROI) into elements connected by nodes, which are then traced back in the target image. All nodal displacements are thus obtained simultaneously [58]. Global DIC has strongly improved during the last decade, with some changes directly aiming at increasing its ability to handle discontinuities within the ROI. In 2008, Réthoré et al. [104] developed an extended global DIC algorithm with crack shape optimization. The team applied the eXtended Finite Element Method (X-FEM) methodology to measure displacements. Based on the finite element shape functions' partition of unity property, the method is able to detect straight and crooked cracks through a crack shape optimization algorithm [104,105]. To the best of our knowledge, global DIC has yet to be implemented into commercially available software.

The subset based DIC method correlates the intensity (grey levels) distribution of small pixels' subsets between a deformed and a non-deformed image to determine the displacement field [106]. The subset size is defined as the set of pixels contained within a square centered on the pixel currently being tracked. The image's grey levels distribution is usually created artificially by coating the surface with random paint patterns. These patterns are usually generated by spraying aerosol paint. The subset size is conditioned by the paint dots' size since the subset should contain a recognizable pattern to yield accurate displacement fields [59]. Local DIC has been adopted and used in most commercial systems, making it a widely used method for experimental mechanic applications.

Commercially available DIC software, like VIC3D (Correlated Solutions), define *confidence margins*, $\mathcal{C}$, from a pixel's correlation equation largest covariance matrix eigenvalue [56]. A confidence of zero means that a subset in the deformed image was perfectly matched to a subset in the initial image. [60]. This situation mostly occurs for purely rigid body motions. Deformed images' subsets are likely to distort and it is expected that $\mathcal{C}$ increases with the strain. Displacement measurements for pixels with a $\mathcal{C}$ above a certain threshold are usually discarded since the error is considered to be too large with respect to the corresponding non deformed subset. This pixel's tracking is therefore lost. Most commercial DIC software struggle when computing fields close to cracks and are thus ill-suited to accurately, and autonomously, detect the exact crack shapes, size or growth rate.

Autonomous crack detection methodologies have also been developed using image processing techniques (see the review by Mohan et al. [107]). Most applications are related to crack detection in concrete. These techniques are limited by the crack propagation direction i.e.

crack detection when its propagation occurs in the transverse direction is less accurate than when it evolves along the longitudinal direction [108, 109]. The review by Mohan et al. also showed that DIC was used in conjunction with image processing algorithms to estimate or forecast the crack's position [110–112]. Iliopoulos et al. [110] used the DIC results to estimate cracks' width. The authors found that the crack's width was overestimated due to the fact that DIC results are not sufficiently accurate close to these discontinuities. Helm [113] proposed a modified DIC implementation in which the ROI is redefined to exclude cracks, at each time step. The method requires a quasi-regular dots pattern as a speckle pattern, which produces a much more regular correlation function. Small deviations in the correlation function, meaning cracks, are thus easily detectable. However, this speckle pattern also increases possible errors during the correlation process because the texture of the subset is not sufficiently different. Other methods, such as Acoustic Emission or Ultrasonic Pulse Velocity are required to obtain quantitative data related to the features of the crack [45].

The field of damage mechanics deals with the effects of damage on a material's mechanical response. Large international efforts are deployed to explore and understand damage mechanisms in Fiber Reinforced Composites (FRCs) [4]. Damage observations in FRCs can provide a fundamental understanding of underlying phenomena or be used to validate predictive models. The World Wide Failure Exercise (WWFE) is an international process that evaluates the predictive capabilities of a number of damage models [64]. The latest edition led to the conclusion that key experimental data is critically lacking to provide meaningful benchmark for certain loading cases and damage mechanisms [65].

More specifically, unidirectional FRCs (UDFRCs) submitted to tri-axial loadings sustain damage in the form of transverse cracks initiated through fiber/matrix interfacial debonding at a free surface [4, 9]. This phenomenon was studied by Martyniuk et al. through X-Ray Computed Micro-Tomography (μCT). Accurate inter-facial crack size, growth rate and debonding angle measurements were all performed manually [9].

These types of crack measurements can serve as benchmarks to micro-mechanical damage models. Cohesive zone modeling [26] or X-FEM [114] are often used to model damage and crack growth in materials. Accurate measurements related to damage features could be used for both methods. More specifically, X-FEM enriches Finite Element (FE) shape functions in discontinuities areas and experimental data about crack growth can be used for that purpose. Moreover, the use of cohesive elements requires the a priori knowledge of the crack path, which can be obtained from experiments.

This paper presents a hybrid approach where local texture features derived from camera images via image processing are combined with commercial DIC software data to autonomously identify crack areas. This approach consists in using the DIC results as a filter to determine possible areas where a crack grows. The exact crack shape is then obtained by combining image processing algorithms, a set of morphological operations and an entropy function. The crack can be detected independently of its shape, or growth path, and this work is performed at a very small computational cost thanks to the DIC results that restricts the image processing algorithm search areas.

We have applied our algorithm to study crack propagation in a single-fiber composite where the fiber was submitted to a transverse load. The experimental data used in this work was obtained by Tabiai et al. [1] and consists of local DIC measurements in the fiber's vicinity while damage is growing around it.

Section 6.3 recalls the experimental setup for both experiments analyzed in this work. Section 6.4 provides background information on DIC's limitations with respect to crack monitoring. Image processing techniques used in the hybrid method are addressed in Section 6.4.2. The hybrid approach and its application are exemplified with a single DIC image involving damage in Section 6.5. The crack path visualization in the reference frame, the crack area growth and the volume-based rendering for both specimens analyzed using the hybrid method are presented in Section 6.6. The parameters used and their impact on crack extraction's accuracy are studied in Section 6.7. Finally, Section 6.8 concludes this work and presents outlooks.

6.3 Experimental Methods

6.3.1 Experimental setup

The experimental data presented herein was obtained from [1]. The complete raw experimental data is available on Zenodo and can be obtained for further analysis [96].

Specimens

The specimens analyzed in this work were composites containing a single-fiber embedded into a standard dog bone specimen and aligned through its thickness. The specimen's configuration is presented in Figure 6.1.

The matrix was a thermoset epoxy having a Young's modulus of 2.5 GPa and a Poisson's ratio of 0.44 [1]. Two different materials were used as the fiber [1]: a 0.90 mm galvanized steel wire and a 0.99 mm Polytetrafluoroethylene (PTFE) monofiber. PTFE is a non-reactive synthetic polymer with a very low coefficient of friction (0.020-0.2 according to the manufac-

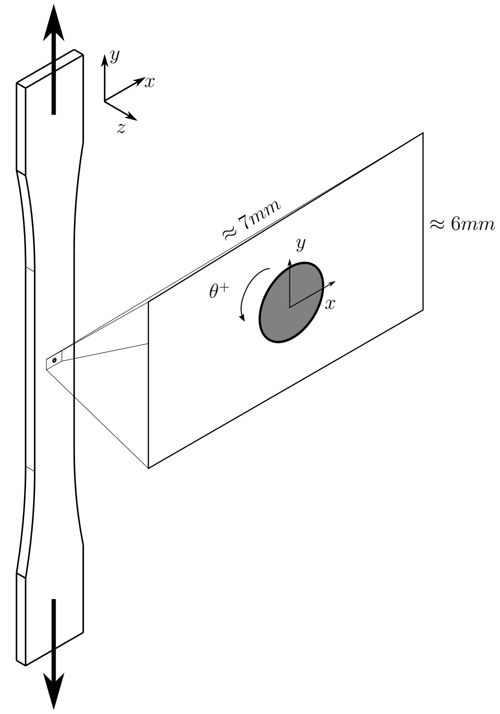

Figure 6.1 Tensile test specimen used. The arrows show the tensile direction. The fiber is visible as a circle in the middle of the specimen. The cameras observe the specimen in the xy plane in an area of 7 mm × 6 mm

turer) [99] and its reported surface energy is not sufficiently high to bond with epoxy [100]. Thus, a PTFE fiber inside an epoxy matrix can only be held through compressive residual forces generated after manufacturing due to the difference in coefficients of thermal expansion (CTE) between the matrix and fibers. Galvanized steel fibers were chosen for their high bonding strength with epoxy [98]. These two different fiber / matrix couples are expected to exhibit different damage evolutions that can be quantitatively evaluated by analyzing damage features.

Tensile test setup

Each specimen was setup in an *Insight MTS* electromechanical testing frame mounted with a 25 kN loadcell. A three-axis precision stage carrying a *VIC-3D*™ stereo-microscope system (acquired from *Correlated Solutions Inc*) was placed in front of the tensile testing machine to acquire stereo images. Figure 6.1 schematically shows the observed specimen area.

6.3.2 Displacement field measurement by local subset based DIC

Speckle pattern

A thin layer of white acrylic spray paint (*Ultra 2X spray paint*, *Painter's Touch ®*) was applied on the specimens' polished side. A mist of black paint was then applied on the white layer to produce a suitable speckle pattern.

The speckle pattern's quality was assessed with the commercial software *VicSnap* (version 8-b245, acquired from *Correlated Solutions Inc*). The software compares the displacement field obtained by DIC for an artificially deformed image for which the imposed deformation is known [56]. The speckle pattern was modified by changing the average dot size and their distribution until the smallest possible confidence margins for the Area of Interest (AOI) was reached. The pattern was improved by removing the paint and re-applying it on the specimen.

DIC software parameters

The DIC algorithm provided by the commercial package VIC3D [60] relies on two main parameters:

Subset size A large subset would not be adequate to capture strain gradients around small geometrical features, such as the fiber [60]. A subset as small as possible was therefore sought.

Table 6.1 Subset and step parameters selected for each analysis

Matrix	Fiber	Subset	Step
Epoxy	PTFE	81	2
Epoxy	Galvanized steel	85	2

Step size The step size is defined as the spacing between analyzed pixels. A step of 2 means that one pixel out of two is tracked. The other pixel's displacement is interpolated [60].

Spatial calibration The stereo-microscope was adjusted and calibrated for distortion, in-plane and out of plane displacement measurements, before each test [56, 60].

The three-axis precision stage was used to move the stereo-microscope image acquisition setup to keep the fiber in the cameras' frame while the specimen was mechanically loaded.

The three-axis precision stage's positions was manually adjusted with the precision rails. Table 6.1 lists the main DIC parameters (subset, step and correlation types) used for each test.

6.4 Background

6.4.1 Damage and crack tracking with DIC limitations

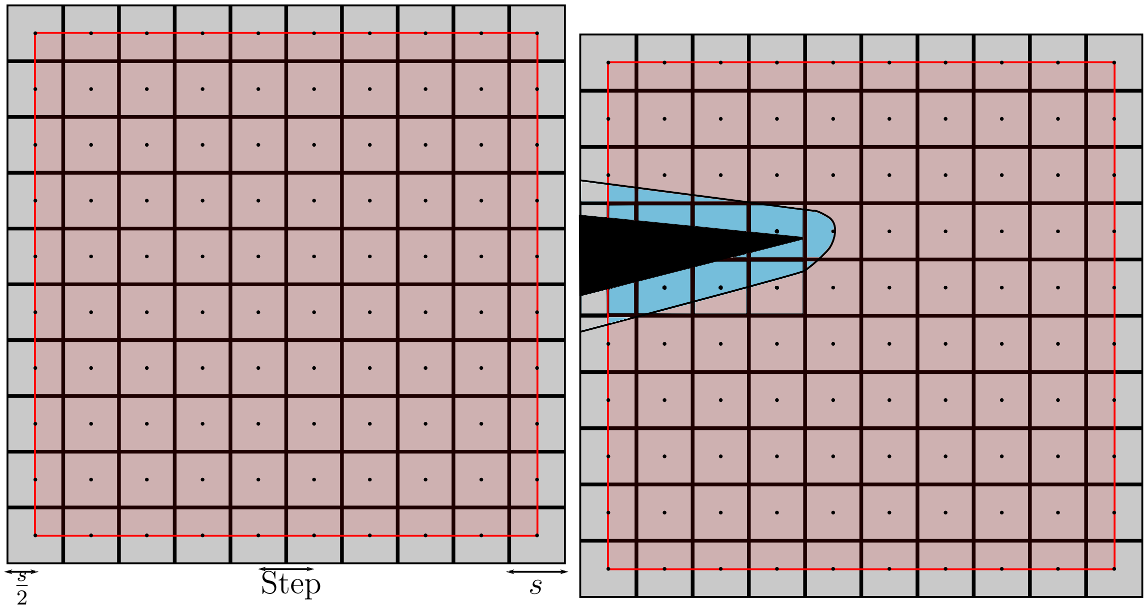

(a)

(b)

Figure 6.2 Schematization of the influence of the crack on DIC accuracy. (a) represents an undeformed surface under observation. The large gray square represents the surface that was covered with a speckle pattern. The grid drawn is used to show the subset size. The black dot at each subsets' center represents the tracked pixel. Since a whole subset is necessary to track a single pixel, the interpolation area is delimited by the red area. (b) represents the same surface once a crack (represented here in black) grew in the material. Subsets for which the speckle pattern is modified by the crack are represented in blue. These subsets can no longer be tracked because the speckle pattern has significantly been modified

Figure 6.2 schematically shows how pixels about half a subset size away from the AOI's edge and those in crack's vicinity cannot be tracked. Figure 6.2a shows that pixels must be surrounded by a subset so that the speckle within its initial subset can be recognized. Subsets on the AOI's edge do not have enough pixels surrounding them to be tracked. Figure 6.2b shows a crack in black growing through the AOI and how it affects subsets in its surrounding. The confidence $\mathcal{C}$ for subsets located in the crack's surroundings increase with its growth, which induces loss of tracking. Moreover, tracking is usually lost around a crack due to the large strains encountered in this area, even if the speckle pattern is unaltered. Crack tracking based solely on $\mathcal{C}$ delivers crack areas over-estimations.

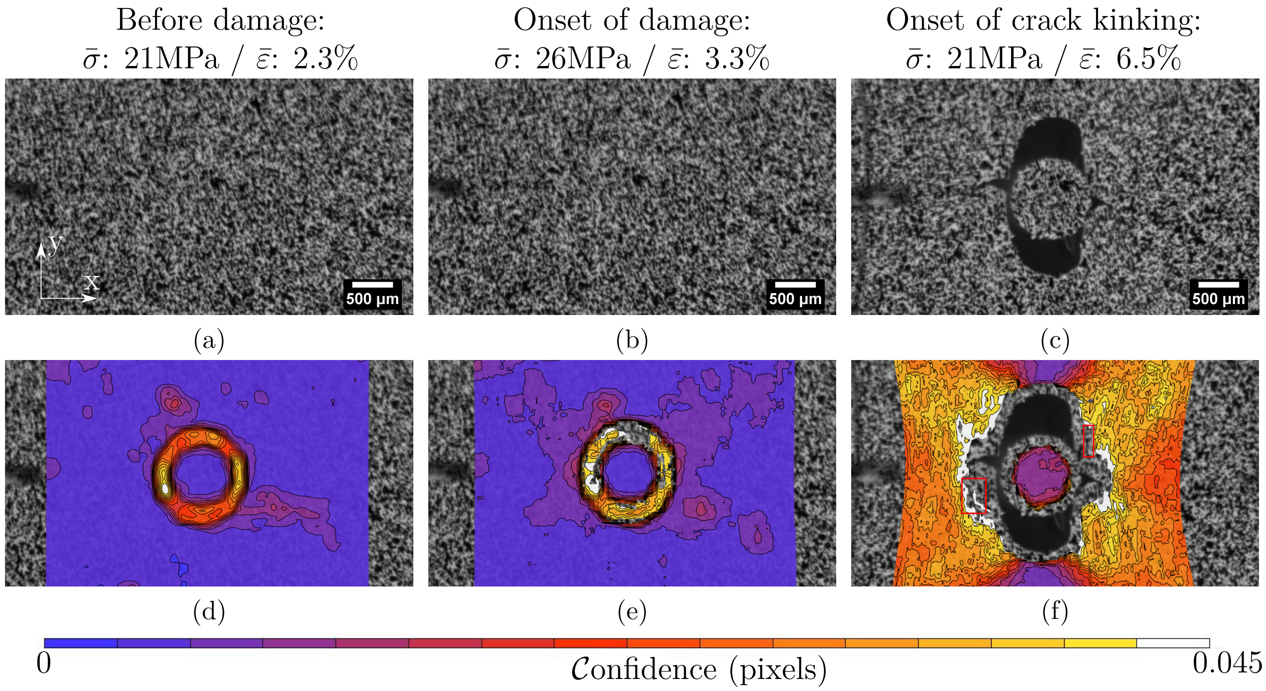

(a) (b) (c)

(d) (e) (f)

Figure 6.3 PTFE fiber / epoxy composite loaded in tension along the y direction: (a) before damage, (b) at the onset of visually distinguishable damage, and (c) at the onset of crack kinking. The first row shows raw images taken by the camera and the second row the corresponding confidence margins $\mathcal{C}$ provided by the DIC software. The red rectangles in image (f) show pixels for which tracking was lost due to the large strains present in this area. $\bar{\sigma}$ is the nominal stress applied by the machine on the specimen and $\bar{\varepsilon}$ is the nominal strain applied on the specimen and was computed by dividing the crosshead's displacement over the specimen's ungripped length.

6.4.2 Image Processing Methodology

Morphological operations [115] transform a binary image (*i.e.*, image of zeroes and ones) by applying operators to every pixel and its neighbors. A pixel's neighbors are defined by a so-called structuring element, which is itself a small (*e.g.*, 3×3) binary image centered around the target pixel.

The two most basic morphological operations are dilation and erosion. Dilation assigns each pixel the maximum value among its neighbors (including itself), which for the case of a binary image means assigning 'one' if and only if there is at least one non-zero pixel among the neighbors. This effectively expands continuous regions of 'ones' outwards. Erosion is the opposite operation using the minimum instead of the maximum, thus shrinking the 'one' regions.

Dilation and erosion operations define the morphological scale space. Applying sequences of dilations or erosions results in expanding or shrinking the shapes in the image, corresponding to moving up or down in the scale space. This can be helpful in removing noise. For example, a series of erosions helps separating small weakly connected regions of 'one' from larger regions.

Morphological thinning [116] is based on the hit-or-miss transformation that considers small subsets around each pixel and compares them to some predefined template. The operation sets to 'one' only the pixels whose neighbors match the structuring element. Continuously applying thinning reduces the binary image to one-pixel-wide skeletons that capture the original image's topology. Morphological pruning [117] defines the structuring elements such that the ends of thin line segments are removed. Pruning is useful for post-processing the topological skeleton by removing small branches that do not significantly contribute to its overall shape.

The discrete entropy H [118] is defined as:

$$H(X) = -\sum_{i=1}^{n} P(x_i) \log_2 P(x_i), \tag{6.1}$$

where X is a discrete random variable with n possible values $X = x_1, x_2, \ldots, x_n$ and a probability mass function $P(x)$. The entropy can be used as a measurement of the distribution's uniformity. In our case, $H(X)$ was computed for pixel values in a small image subset to estimate the image's local heterogeneity. This estimate was maximized when all pixel values are uniformly distributed (*e.g.*, white noise), and was minimized when all pixels have the same value.

6.5 Crack area extraction in single fiber composites

The techniques presented in Section 6.4.2 were applied to an arbitrary image containing a crack acquired during a tensile test on the PTFE / epoxy specimen. Figure 6.9 shows snapshots for the PTFE / Epoxy specimen (a) before damage, (b) at the onset of damage, and (c) at the onset of crack kinking. Each pixel corresponds to approximately 3.1 µm. Figure 6.9 also shows the confidence margins $\mathcal{C} \in [0, 1]$ for the displacements provided by *VIC-3D*™ [60] as a contour plot in the second row. Figure 6.9d shows that the confidence value close to the fiber-matrix interface increases even for small loads, which means that

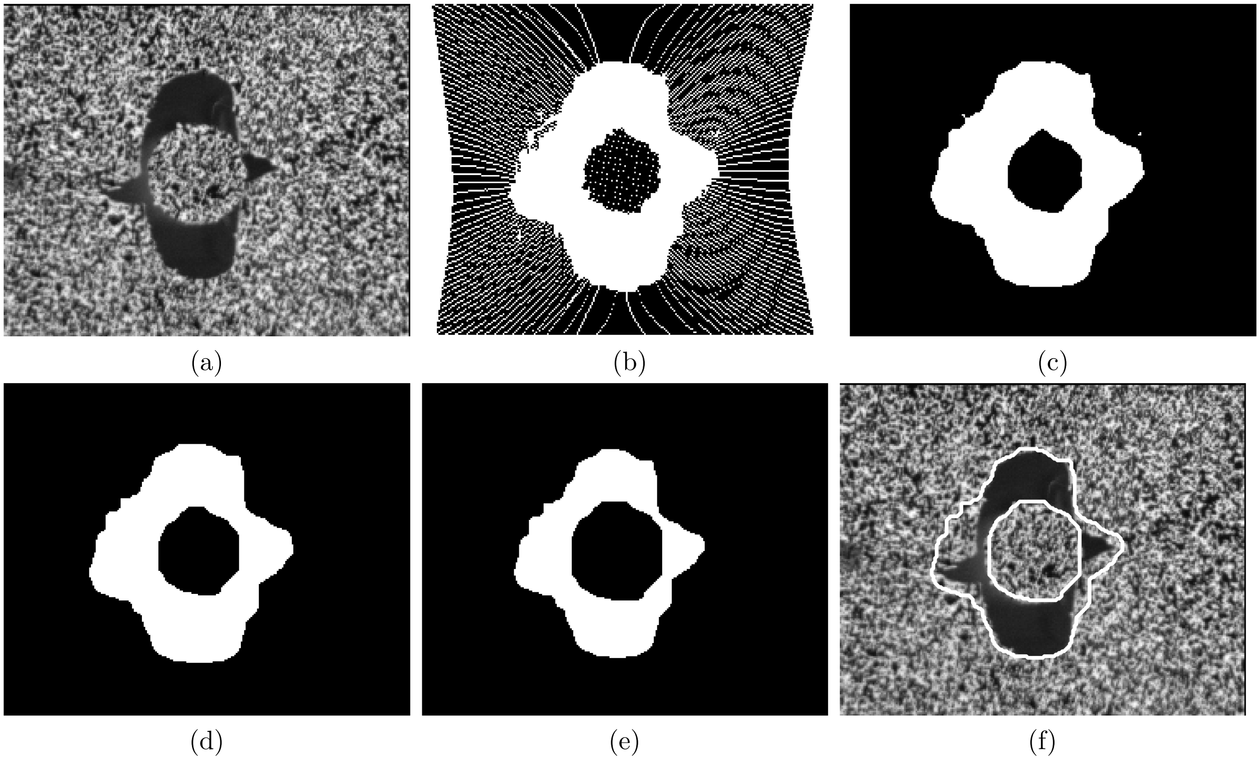

Figure 6.4 Crack extraction using DIC tracking data for the PTFE / epoxy specimen with $\bar{\sigma} = 20.2$ MPa and $\bar{\epsilon} = 6.66$ %: ((a)) Original camera image. ((b)) Pixels in the target frame that were not matched from the reference frame are encoded as white. ((c)) Unmatched pixels after a Gaussian filter and thresholding. ((d)) Image obtained after morphological filtering: small holes and objects are removed. ((e)) Final image after erosion, compensating for the DIC subset size. ((f)) Contour of the final image overlayed over the original camera image. The DIC-based method provides only a rough crack shape estimate and overestimates its area.

significant deformations occurred in those areas. Figure 6.9e and 6.9f show that $\mathcal{C}$ increased in other areas as the load increased.

The chosen image is shown in Figure 6.4a (corresponds to Figure 6.9c) and is used throughout Section 6.4.2 to examplify DIC-based and image processing-based crack extraction algorithms' limitations on our specific experiment.

6.5.1 DIC-based crack extraction

The DIC-based technique assumed that the pixels belonging to the crack are those for which correlation was lost.

A binary image was constructed first by encoding pixels with a match as 'zero' and the unmatched pixels as 'one' (white pixels in Figure 6.4b). Besides the main unmatched area

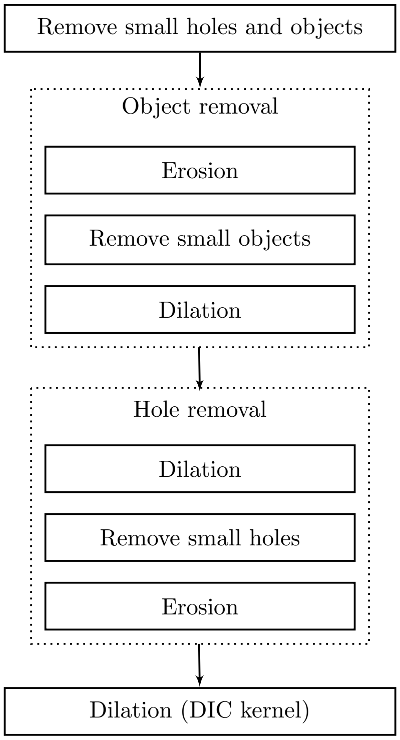

Figure 6.5 An overview of the filtering performed on the unmatched pixels, which were extracted from the tracking data. The filtering was achieved by using morphological operations: objects with small area were removed between erosion and complementary dilation. Holes were removed in the opposite sequence: dilation first, holes with small area, and erosion back

around the crack, the image also contains thin lines of unmatched pixels. These lines result from two neighboring pixels in the reference frame being tracked to the same pixel in the target frame, leaving a nearby unmatched pixel in the target frame. We convolved the image with a Gaussian kernel that removed high-frequency details from the image, effectively blurring it, to remove the untracked pixels. We then thresholded the resulting image, marking as 'one' all pixels with value above 0.5. The overall operation fills in unmatched pixels that are surrounded by mostly matched pixels and produces a locally coherent image without the noise (Figure 6.4c). The image's left and right border exhibit unmatched pixels that result from the fact that the ROI moved away from the camera's frame during the test. These areas can be manually removed by ignoring the regions of unmatched pixels immediately adjacent to the ROI's borders.

The next step consisted in removing noise in the binarized image. This was achieved by performing a set of morphological operations. Figure 6.5 presents an overview of the operations used.

Figure 6.6 Crack extraction using texture features in the original camera images for the PTFE / epoxy specimen with $\bar{\sigma} = 20.2$ MPa and $\bar{\epsilon} = 6.66$ %. ((a)) Local entropy of the camera image. ((b)) Local entropy after thresholding into a binary image. ((c)) Final image after compensating for the local entropy subset size. ((d)) Contour of the final image overlayed over the original camera image. The image based method appears to underestimate the crack area.

Figure 6.7 Crack extraction using the hybrid method for the PTFE / epoxy specimen with $\bar{\sigma} = 20.2$ MPa and $\bar{\epsilon} = 6.66$ %. ((a)) DIC-based crack estimate after a round of dilations. ((b)) Image-based crack estimate using a smaller subset size. Note the false-positive regions produced by imperfections in the speckle pattern. ((c)) Final image after combining the DIC- and image-based estimates. ((d)) Contour of the final result overlayed over the original camera image. The hybrid method appears to produce an accurate crack area estimate.

All continuous regions having a total area below a threshold were removed. This operation removes holes and objects (i.e., small continuous regions of ‘zeroes’ and ‘ones’, respectively). Then, filtering was performed at a different morphological scale (Section 6.4.2). A sequence of erosions was applied, followed by removing small disconnected objects. A complementary sequence of dilations was performed to return back in morphological scale space. The operation was repeated next, but in the opposite direction: applying a sequence of dilations, removing small holes and applying a complementary sequence of erosions. The result is presented in Figure 6.4d.

The resulting crack area requires compensation for the subset size used for DIC. The need for this compensation is illustrated in Figure 6.2b, where pixels lost tracking not only when they were directly in the crack area, but also when the crack was nearby, strongly deforming the

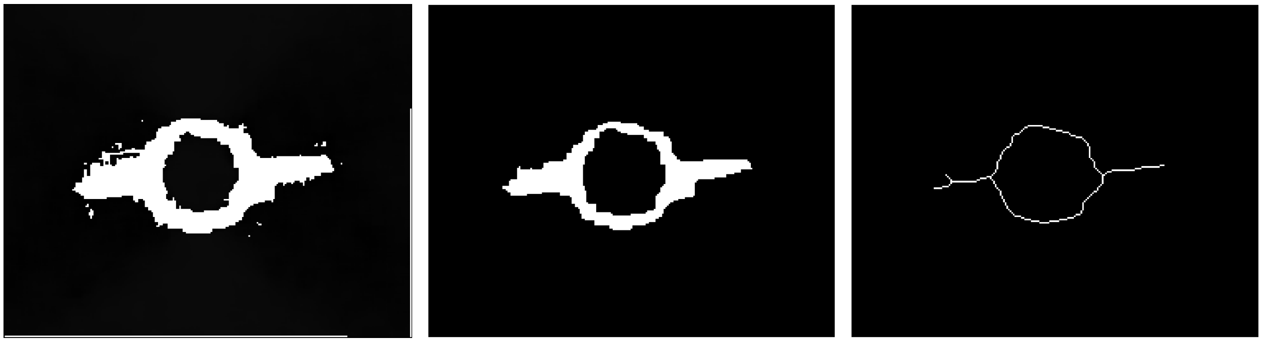
(a) (b) (c)

Figure 6.8 Crack path extraction in the reference frame for the PTFE / epoxy specimen with $\bar{\sigma} = 20.2$ MPa and $\bar{\epsilon} = 6.66$ %. ((a)) Thresholded confidence values $\mathcal{C}$. White represents pixels in the reference frame that lost correlation. ((b)) Results after morphological filtering. ((c)) Final crack path estimate obtained through morphological skeletonization.

material in the crack's vicinity. As a result, the area that lost correlation is larger than the actual crack. Another sequence of erosions was applied, with the number of erosions equal to the half-size of the DIC subset to compensate for losses at the edge of the AOI. The final image represents the estimated crack area (Figure 6.4e, 6.4f). The crack area obtained using DIC-based extraction method overestimates the visible crack area.

Image-based extraction

Our image-based method relies on the visual disparity between the crack and the speckle pattern painted on the specimen. Specifically, it was assumed that the crack areas were roughly homogeneous and that the speckle pattern exhibited a high variance. For this reason, an entropy filter that computes local entropy was applied around each pixel, with a subset size equal to half the DIC's subset size (parameter studied in Section 6.7). The result is shown in Figure 6.6a. It was then binarized with a threshold of 1.0 natural units (studied in Section 6.7). Figure 6.6b shows the binary image. A sequence of dilations, the number of which was equal to the subset's half-size, was then performed to compensate for the filter subset size to obtain the final result (Figure 6.6c and 6.6d).

This image-based method relied on a subset (neighborhood) around a pixel for computation, thus making the subset size an important parameter with a significant effect on the result (similar to how DIC subset size affects the tracking results). If we use a smaller subset, the method detected the shape of the crack boundary more accurately, but became less robust and produced false-positive results, confusing small cracks and the speckle pattern. A false-positive mistakes an area of the image which is not a crack for a crack. For this reason we

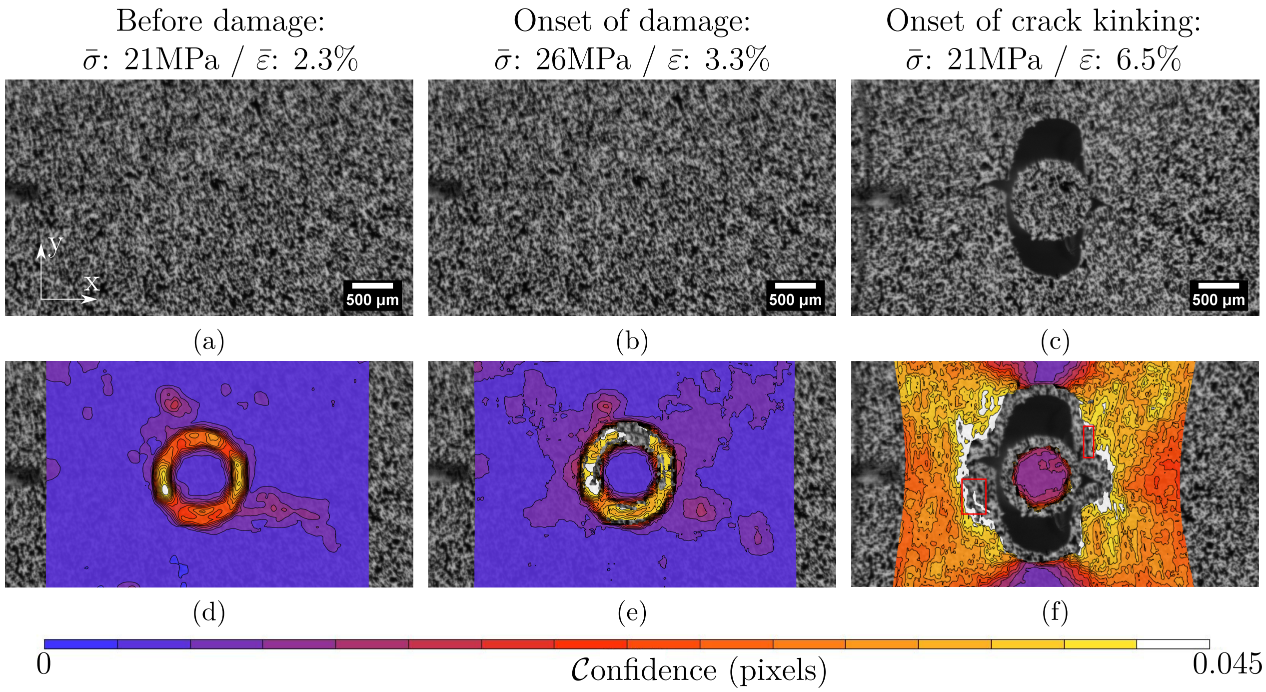
Before damage: $\bar{\sigma}$: 21MPa / $\bar{\varepsilon}$: 2.3%

Onset of damage: $\bar{\sigma}$: 26MPa / $\bar{\varepsilon}$: 3.3%

Onset of crack kinking: $\bar{\sigma}$: 21MPa / $\bar{\varepsilon}$: 6.5%

(a) (b) (c)

(d) (e) (f)

Figure 6.9 PTFE fiber / epoxy composite loaded in tension along the y direction: (a) before damage, (b) at the onset of visually distinguishable damage, and (c) at the onset of crack kinking. The first row shows raw images taken by the camera and the second row the corresponding confidence margins $\mathcal{C}$ provided by the DIC software. The red rectangles in image (f) show pixels for which tracking was lost due to the large strains present in this area. $\bar{\sigma}$ is the nominal stress applied by the machine on the specimen and $\bar{\varepsilon}$ is the nominal strain applied on the specimen and was computed by dividing the crosshead's displacement over the specimen's ungripped length.

opted to combine our image-based and DIC-based methods into a hybrid approach described in Section 6.5.2.

6.5.2 Crack area extraction with the hybrid method

Hybrid crack extraction

Our hybrid crack extraction method which combines DIC-based and image-based analysis is depicted in Figure 6.10. Specifically, image-based crack detection was restricted to the areas near our DIC-based crack identification, which allowed for computing local entropy with a reduced subset size. This results in a more accurate crack shape, while the restricted search area filters out potential false-positive results.

First, we took the DIC-based crack area obtained in Section 6.5.1 and applied a sequence

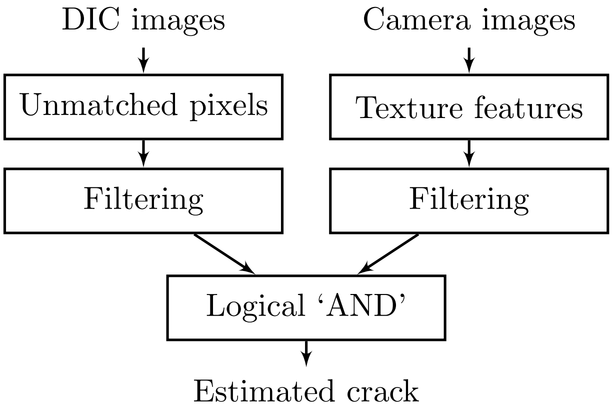

Figure 6.10 An overview of our proposed crack estimation approach. First, the DIC tracking data is used to determine which pixels were not matched from the reference frame. This produces a rough crack shape. Texture features are extracted from the camera image and filtered to obtain an image-based result to refine the DIC crack estimate. Finally, the two images are combined together to obtain a more accurate crack area through a 'AND' boolean operation

of three dilations to expand our search area. The result is shown in Figure 6.7a. Then, an image-based crack area is computed using a smaller subset size (Figure 6.7b, cf. Figure 6.6b). Finally, a logical 'AND' operation was performed: a pixel belongs to the crack if both the image-based and the dilated DIC-based methods classified it as a crack. Finally, the result was compensated for texture filter subset size (similarly to Section 6.5.1) to obtain the final crack estimate in Figure 6.7c, 6.7d. Note that this hybrid method achieved better accuracy than both the pure image-based and the DIC-based solutions, while still avoiding false-positive results.

Crack path in the reference frame

The crack path computation was based on the DIC confidence values $\mathcal{C}$ in the reference frame (as opposed to the crack area extraction, which was performed in the target frame). First, the confidence values were thresholded to obtain a binary image where the lost pixels are encoded as 'ones'. Figure 6.8a shows the binary image obtained after thresholding confidence values. A sequence of binary erosions was performed, followed by removing small disconnected regions of 'zeros' to remove small noise resulting from tracking errors (Figure 6.8b). Next, the crack topology was obtained by extracting its skeleton through continuous morphological thinning, which reduced continuous regions to one pixel. The obtained path was then further filtered with morphological pruning. The resulting topology is shown in Figure 6.8c. Some small irregularities in the shape were still be observed, but overall a crack path estimation in the reference frame in accordance with the one in the deformed frame was obtained.

6.6 Application of the hybrid method to the experimental data set

6.6.1 Crack path visualization in reference frame

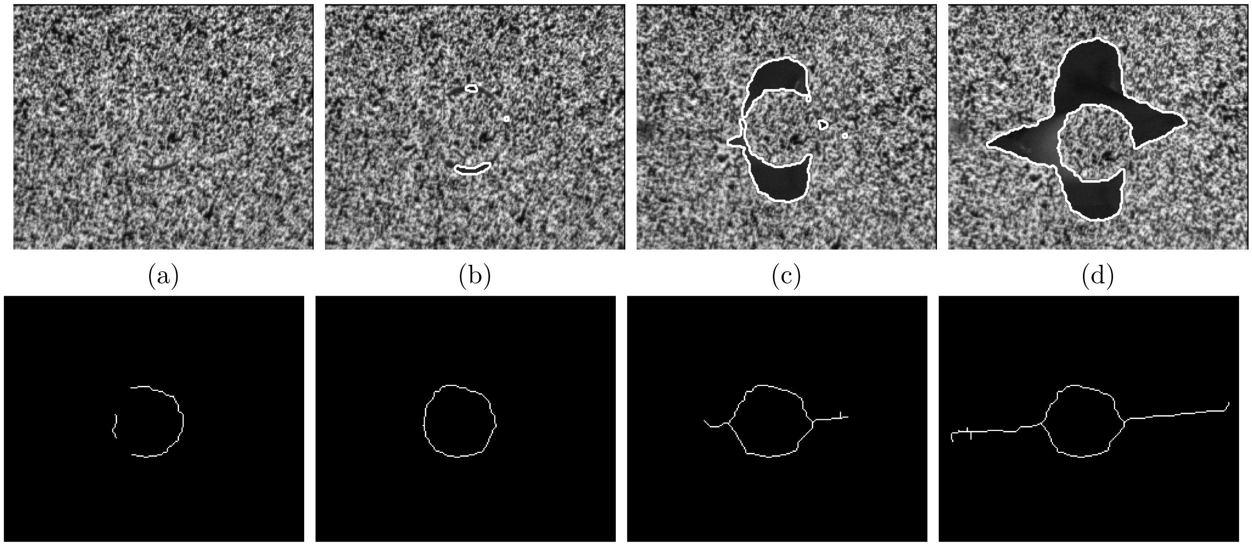

$\bar{\sigma}$: 25.6MPa / $\bar{\varepsilon}$: 9.9% $\bar{\sigma}$: 25.4MPa / $\bar{\varepsilon}$: 4.6% $\bar{\sigma}$: 20.9MPa / $\bar{\varepsilon}$: 6.5% $\bar{\sigma}$: 17.6MPa / $\bar{\varepsilon}$: 7.0%

(a) (b) (c) (d)

(e) (f) (g) (h)

Figure 6.11 Timelapse of the crack area detection and extraction presented for the PTFE / epoxy specimen. Top row: results of the hybrid crack area extraction in the target frame. Bottom row: result of crack path extraction in the reference frame. Images are arranged chronologically, left-to-right. First column: early in the experiment the first visible cracks appear. Second column: first extracted cracks. Third column: crack starts to propagate horizontally. Fourth column: later stages of the experiment.

Figure 6.11 compares the extracted crack area in the target frame (top row) and crack path in the reference frame (bottom row) for the PTFE / epoxy specimen after inter-facial debonding propagated around the fiber. The images are presented in a chronological order, from left-to-right. The first column corresponds to one of the experiment's earliest frames. While it is possible to see the first crack areas, it is not yet possible to reliably detect them due to their small size with respect to image's resolution (Figure 6.11a). Reducing our image-based method neighborhood size (described in Section 6.4.2) could help, but would also introduce false-positive results. However, we can already see the forming crack path in the reference frame (Figure 6.11e). Crack path extraction is solely based on the DIC data, and some pixels already start to loose tracking due to large deformations and thin cracks near the fiber. In the second column, we see one of the earliest frames with a detectable crack area (Figure 6.11b). At this point in time, the crack path in the reference frame is fully formed around the fiber (Figure 6.11f). The third column demonstrates the stage at which the crack starts spreading horizontally. We are able to accurately extract the crack area, as well as detect its horizontal propagation (Figure 6.11c, 6.11g). The last column shows the crack area detected on the picture and crack path in the reference frame detected before specimen failure (Figure 6.11d, 6.11h).

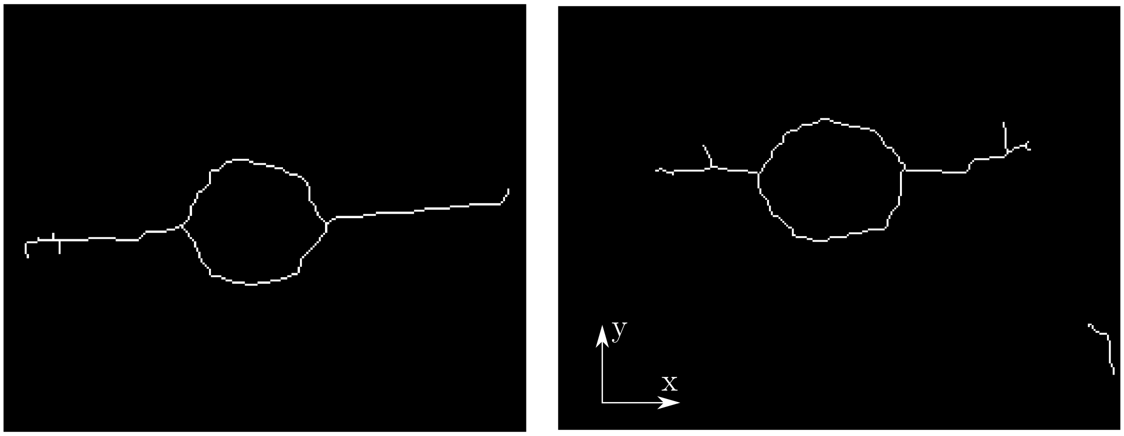

(a) PTFE fiber with epoxy matrix at a global strain level of 7% and global applied stress of 17.5 MPa

(b) Galvanized steel fiber with epoxy matrix at a global strain level of 8.8% and global applied stress of 17.7 MPa

Figure 6.12 Crack path extraction for two different sets of fiber / matrix. The crack path in the reference frame shows how the fracture pattern is affected for different materials. Both cracks are represented using the same scale

Figure 6.12 shows the crack path extracted for the PTFE / epoxy and galvanized steel / epoxy specimens. Without any bonding, the inter-facial crack grows in a symmetrical manner for the PTFE / epoxy specimen, at about the same rate for the crack visible above and below the fiber. This reveals a transverse crack path perpendicular to the applied load direction that crosses the fiber's diameter, as shown in Figure 6.12a. For the galvanized steel / epoxy specimen, inter-facial crack growth does not happen at the same rate for the crack above and the one under the fiber. This might be attributed to the fact that the inter-facial bonding strength might vary around the fiber. Although the crack path is perpendicular to the applied load direction, it is offset in the positive y direction, as shown in Figure 6.12b.

Crack area growth

Figure 6.13 shows, as continuous lines, the crack area determined using our hybrid method. The crack area obtained using the hybrid method for the PTFE / epoxy specimens is plotted

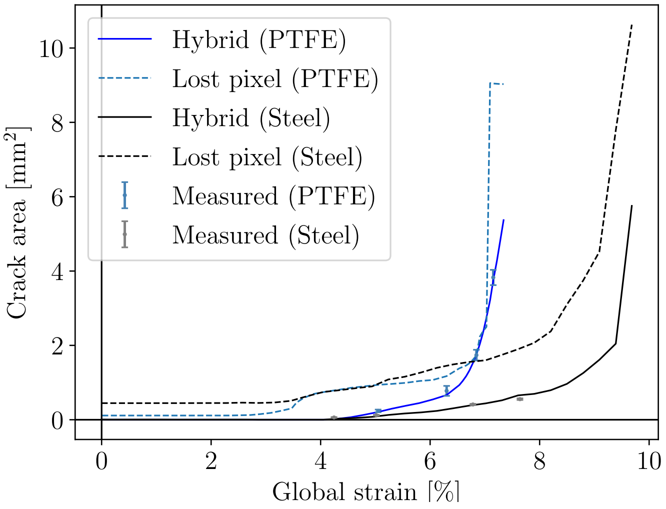

Figure 6.13 Estimated crack area as a function of the applied strain. The area obtained for the PTFE / epoxy and galvanized steel / epoxy specimens are shown as blue and black lines, respectively. Four manual crack size measurements (using the *Polygon selection tool* from the open source *ImageJ 1.51* software) were performed by a domain scientist at arbitrary moments during the test to compare results with the measurements performed using the hybrid method for each specimen. Each manual measurement was performed five times, the average for each measurement is shown as a cross and the standard deviation is represented as an error bar. An estimate of the crack area using the sum of areas covered by pixels for which tracking was lost is also shown as a dotted line

in blue, while that for the galvanized steel / epoxy is plotted in black. The crack area was also manually measured using a polygon selection tool from an image processing software to validate the obtained results (from the open source *ImageJ* software) at four different time-steps, for each specimen. Since crack extraction remains an error-prone task, even for a domain expert, each measurement has been repeated five times. Figure 6.13 reports the average crack area value manually measured for each time-step as well as their 95 % confidence intervals. The manual and hybrid results are reasonably consistent with a maximum error for the hybrid method with respect to the manual measurements of 12%. This error is high at the beginning of the experiment because the crack area is still small, thus, small variations have a relatively higher impact on the method's relative accuracy.

The crack size area estimated from the lost pixels is also reported in Figure 6.13. This crack size estimate obtained with the DIC data overestimates the real crack size. The manual and hybrid method measurements provide the same results and are consistent.

Figure 6.13 shows that the cracks in both the PTFE / epoxy and glavanized steel/epoxy specimens started growing at around the same moment, slightly after an applied global strain of 4 %. The plot shows that crack initiation appears to be independent of the fiber / matrix bonding strength, as it occurs at the same applied global strain for both specimens. The PTFE/epoxy specimen's crack then grows linearly up to 6.5 %. The galvanized steel / epoxy specimen's crack also grows linearly but at a slower rate than that in the PTFE / epoxy specimen. This observation might be due to the stronger bonding between epoxy and galvanized steel / epoxy. A significant increase in the crack growth rate for the PTFE / epoxy specimen can be noticed for a global strain of about 6.5 %. This increase is due to the inter-facial crack growth in the matrix, as shown in Figure 6.11c. The crack then keeps growing until specimen failure is reached for a global strain of about 7.2 %. Inter-facial crack growth in the matrix for the galvanized steel / epoxy specimen appears to be delayed as it only happens for a global strain of about 9.5 %. This suggests that the strong bonding between galvanized steel and epoxy slows the crack growth rate down, which is not the case for the PTFE / epoxy specimen. Inter-facial crack initiation thus appears to be independent of the fiber / matrix bonding properties under transverse load. However, crack growth within the matrix strongly depends on the fiber / matrix bonding properties.

6.6.2 Volume-based rendering of time-dependent crack growth

A volume visualization was produced by stacking extracted two-dimensional crack regions chronologically, along the third dimension. It provides a concise crack growth overview and is presented in Figure 6.16.

Additionally, the crack regions were colored according to the global strain level at which tracking was lost for the pixel.

This volume representation allows to rapidly observe that, for the galvanized steel / epoxy specimen (Fig 6.15), the crack originates above the fiber first, then initiates under it while still growing at the top. The crack remained localized at the fiber's top and bottom areas. For the PTFE / epoxy specimen (Fig 6.14), the crack initiated almost simultaneously at its top and bottom areas, and then grew all around it while symmetrically growing in the matrix time in the transverse direction, at a roughly uniform rate. These images directly show that the galvanized steel / epoxy specimen offered more resistance to crack initiation and growth than the PTFE / epoxy specimen did.

6.7 Discussion

Figure 6.17 shows our method's stability with respect to its parameters. The most impactful parameter is the entropy filter subset size, measured as a fraction of the DIC subset size. Larger sizes increase robustness, but lead to false-negatives, reducing the estimated crack area (Figure 6.17a). In contrast, very small subset sizes result in false-positives, thus overestimating the crack area. Here we found that values ranging from 0.4 and 0.75 produced the most accurate results with respect to our manual measurements.

The second studied parameter is the threshold applied to the image entropy (Section 6.5.1). Smaller threshold values make stronger assumptions about the crack area's visual homogeneity, thus producing a more conservative estimate, and vice versa (Figure 6.17b). The optimal threshold choice, as well as the subset size for the entropy filter, depend on the speckle pattern's quality: a more coarse-grained pattern may require a larger subset size and a smaller threshold value to avoid classifying random imperfections as cracks. We found that a threshold value of 1 yielded accurate results.

The final parameter is the number of dilations applied to the DIC-based crack before using it as a search area for the hybrid method (Section 6.5.2). The value should be sufficiently large to include the whole crack before applying image filters to narrow the selection. Due to inaccuracy of the DIC-based crack, small values result in overly restricted search area, reducing the estimated crack area (Figure 6.17c). Here values of three and above resulted in an accurate estimate.

Overall, the method appears to be fairly insensitive to the choice of parameters, with gradual changes to their values influencing the results in a regular and predictable way. Optimal parameter values can quickly be selected by performing several runs of our method and comparing the results to a crack area manual measurement for an arbitrary time-step.

6.8 Conclusion and Outlook

We introduced a hybrid approach that relies on image processing techniques combined with digital image correlation for tracking and extracting crack surfaces. We validated our methods on crack areas manually measured. This observation suggests that the manual time consuming task for this procedure can be automated. Moreover, the hybrid approach is able to detect smaller crack areas that cannot be easily seen by eye, due to their size.

The crack surface mapping back to the initial configuration is valuable for two different communities. This information could be used by the computational engineering community to advance damage related simulations. This mapping could be used to indicate, for example, where to use cohesive elements to obtain more accurate benchmarks against experimental data. For the experimental mechanics community, this information could be used to gather more insights on how cracks grow and the corresponding crack paths. The volume-based rendering of time-dependent crack growth delivers a concise overview of crack growth. This representation can be used to quantitatively summarize the damage history of a specific fiber / matrix experiment. This representation could be extended to highlight the differences in crack initiation and crack growth between mechanisms in materials with different properties.

Quantitative measurements of inter-facial crack growth rate are provided for each analyzed specimen. Results showed that fiber / matrix inter-facial crack initiation under transverse load appears to be independent of fiber / matrix bonding strength and fiber mechanical properties. Inter-facial crack growth rate and inter-facial crack growth into the matrix are significantly delayed thanks to strong bonding.

This approach was tested on a simpler case with a single-fiber per specimen for which manual measurement would be, although time-consuming for all images, possible. Future works related to this method would be the analysis of experimental cases with a multitude of fibers and micro-cracks simultaneously growing, for which manual measurements would be too complex for an operator.

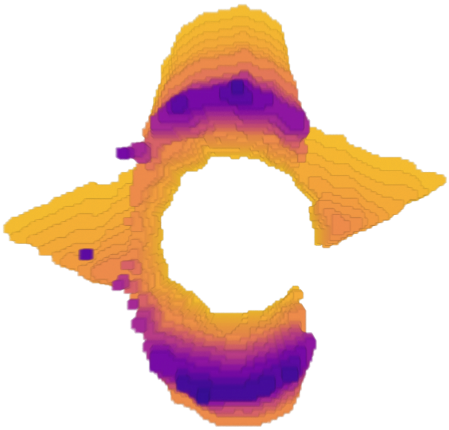

Figure 6.14 PTFE fiber with epoxy matrix.

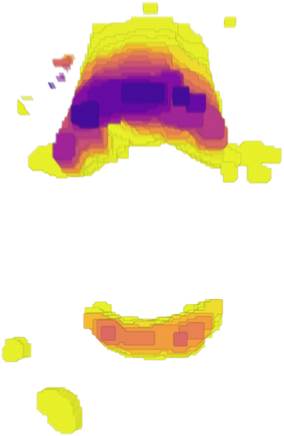

Figure 6.15 Galvanized steel fiber with epoxy matrix.

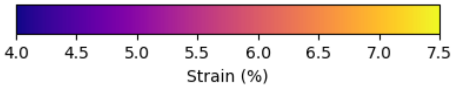

Figure 6.16 Crack growth volume visualization. Extracted crack regions from each frame were stacked on top of each other in the direction perpendicular to the image. The color represents the strain in that frame

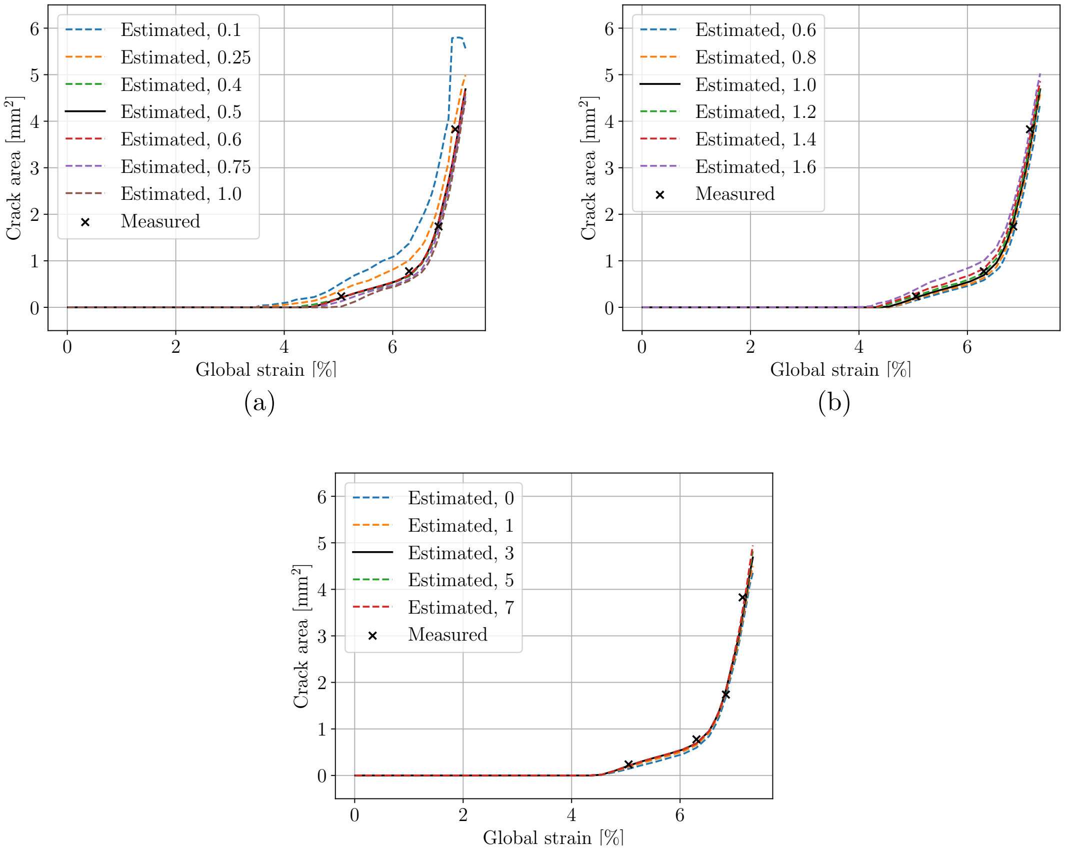

(a) (b)

(c)

Figure 6.17 Sensitivity of the crack area with respect to the proposed algorithm parameters. Results for the optimal parameter value are rendered as a solid line. The estimated crack area is also compared against the value measured manually. **(a):** Crack area estimation as a function of the entropy filter subset size. **(b):** Crack area estimation while varying the threshold value of the entropy image filter. **(c):** Crack area estimation while varying the number of dilations applied to the DIC-based crack area before using it in the hybrid method

CHAPTER 7 ARTICLE 3: *IN-SITU* FULL FIELD OUT OF PLANE DISPLACEMENT AND STRAIN MEASUREMENTS AT THE MICRO-SCAL IN SINGLE REINFORCEMENT COMPOSITES UNDER TRASNVERSE LOAD

I. Tabiai, D. Texier, P. Bocher, D. Therriault and M. Lévesque

Submitted to: Experimental Mechanics on November 8th, 2018.

7.1 Abstract

The fiber / matrix inter-facial damage mechanisms of fiber-reinforced composites (FRCs) are investigated for four different composites containing a single fiber or bundle of fibers under transverse load. A laser scanning confocal microscope (LSCM) is used for micro digital image correlation (µDIC) during *in-situ* quasi-static tests of single-reinforcement dogbone specimens. Three fibers having radically different bonding strength with epoxy in addition to a bundle of about a hundred carbon fibers were tested as reinforcements. For all specimens, damages initiated with fiber debonding at the free surface along the tensile direction. The crack then propagates around the interface while slightly growing along the fiber. The inter-facial crack is shown to grow faster for couples with weak inter-facial bonding. Strong fiber / matrix bonding is shown to stop Mode II transverse inter-facial debonding which significantly delays specimen failure. Analysis of the LSCM micrographs with µDIC is used to provide measurements of displacements, strains, and measure depth during each test. The importance of out of plane displacements in inter-facial debonding is highlighted. Out of plane displacement is shown to play a role in inter-facial crack opening and growth and ought to be considered when studying or modeling damage in FRCs. µDIC is shown to be a promising technique to provide a better understanding of the damage mechanisms at the fiber or bundle scales and to determine inter-facial toughness of a specific fibre / matrix couple in order to perform accurate damage modeling in FRCs. Displacement, strain, and confidence field results for each pixel from each experiment and at each time step are also provided in an extensive data package for detailed comparison with simulation results.

7.2 INTRODUCTION

At the microscopic scale (i.e., $\leqslant 100$ µm, referred to herein as *microscale*), unidirectionally Fiber Reinforced Composites (FRCs) exhibit a heterogeneous microstructure composed of parallel fibers embedded within a polymeric matrix. At the macroscopic scale, FRCs exhibit anisotropic mechanical properties [4]. FRCs' microstructure is responsible for their intricate damage mechanisms: inter-facial debonding, matrix microcracking, fiber breakage, fiber microbuckling, void growth, among others [4, 17–20]. The World Wide Failure Exercise (WWFE) is an international process that evaluated the predictive capabilities of a number of damage predictive models [64]. The first exercise showed a clear lack of faith in the failure criteria in use during the 1990s-2000s, but also no clear evidence that any criteria provided meaningful failure predictions [64]. In 2013, the second edition of the WWFE evaluated twelve failure theories applied to polymeric matrices reinforced by carbon and glass fibers in a variety of composites, geometries and loadings [65]. It focused on triaxial failure criteria. A large scatter and divergence in predictions were observed between simulation results and experiments. The exercise showed that current models can hardly predict every failure mode in 3D [65,66]. Another conclusion of the second WWFE is that key experimental data is critically lacking to provide meaningful assessment for certain loading cases and damage mechanisms [65]. The third edition of the WWFE started in 2015 and is focused on benchmarking 3D damage models against experimental data. The complete results for this edition are yet to be published. Although various damage prediction models are available, their ability to predict damage for different materials, geometries and loadings remains limited [66].

The field of Macro-Damage Mechanics (MADM) studies the material's overall behavior with damage modeled as internal variables characterizing the damage growth level, such as crack density growth [4]. MADM models are often formulated within a thermodynamics framework and macroscopic constitutive equations can often be derived. However, parameters used in MADM are not always directly connected to physical mechanisms [68, 119]. Damage growth level modeling requires damage laws able to describe how, and at which rate, damage features grow through the material [26, 71]. Micro-damage mechanics (MIDM) explicitly models voids and inclusions as part of the microstructure. Constituent material properties are estimated using various methods to obtain averaged quantities [4,120,121]. MIDM models are often numerically implemented through computational mechanics. Thanks to the constantly increasing available computing power and the development of damage oriented frameworks and tools, computational mechanics appears to be the mostly adapted field to tackle the complexity of FRCs damage problems. Computational mechanics implementations of MIDM can handle a FRC with all its heterogeneities and interfaces, explicitly [4, 12, 26, 51, 121]. When transversely loaded with respect to the fibers' direction, damage in unidirectional FRCs initiates through fiber / matrix interfacial debonding at a free surface. This damage mechanism has been reported to be the most critical under transverse loading [4, 9, 122].

A variety of tests have been used to characterize the fiber/matrix interface: the pull-out, the push-out, the three fiber and the microbond tests [4,35]. These methods experimentally measure the averaged fiber / matrix inter-facial shear strength (IFSS). The IFSS measures the Mode II intefacial fracture thoughness [26]. However, inter-facial debonding is a mechanism which has been reported to occur under mixed-mode conditions [4,26,41]. Thus, the IFSS might not be sufficient to completely characterize and validate inter-facial debonding models for FRCs subjected to macroscopically transverse loading [9,26].

Damage for a single fiber composite under transverse loading was investigated by Martyniuk et al [9]. Through X-Ray Computed Micro-Tomography (µCT), the authors demonstrated how tunneling (i.e., inter-facial debonding along a fiber's axis) directly impacted the inter-facial debonding at the specimen's free surface for an E-glass / epoxy single fiber composite. The observations documented and validated damage mechanisms and predictions for theories for which experimental data was lacking. No local or full field displacement measurements were done in that work. Accurate knowledge of the fiber / matrix interface, and its behavior, during damage growth is required to model an experimental case similar to that studied by Martyniuk et al [9].

Most damage observations of single fiber composite and FRCs found in the literature were performed using Scanning Electron Microscopes (SEM) [59,61] or µCT [9,51]. X-rays have been reported to damage epoxy specimens during observation and might change material behavior at the free surface [9]. In addition, out of plane measurements can hardly be obtained with a single detector under a SEM. The Laser Scanning Confocal Microscope (LSCM) technique consists in capturing images at different regular depth intervals, blocking out of focus light at each depth. The method thus enables reconstructing three dimensional structures and out of plane measurements.

Digital Image Correlation (DIC) is an optical method for computing 2D and 3D displacement fields based on a cross-correlation between an initial and a deformed images. The method requires a random grey level pattern that can either exist naturally on the specimen or be produced artificially (*e.g.* speckle pattern created with paint droplets). Micro digital image correlation (µDIC) has already been applied to FRCs to measure displacements and strains at the fiber scale [59,61]. Canal et al. [61] first used µDIC to investigate strain fields in a unidirectional E-glass / epoxy FRC under transverse compression. Submicron alumina particles were dispersed on the specimen's surface as a speckle pattern. A SEM was used to capture images. The study showed the potential for applying µDIC to FRCs' surface displacement measurements, although strain concentrations around fiber bundles were reported as difficult to identify. Mehdikhani et al. [59] pursued this line of work a few years later by performing a similar experiment on an E-glass / epoxy specimen loaded using a three-point bending setup.

The authors improved the method used to deposit submicron particles, which made detection of strain concentrations due to fiber bundles possible. However, the authors reported difficulties measuring displacements in the vicinity of isolated fibers due to the speckle pattern's properties and limitations of the subset based DIC method [59]. No damage, and specifically no inter-facial decohesion, was observed during these experiments [59, 61]. Nevertheless, the matrix' out of plane behavior around a single fiber was not investigated while damage is growing by Martyniuk et al [9]. Other authors have compared local strain fields measured by DIC with numerically predicted fields in FRCs submitted to transverse loads [12,41,51,59,61]. To the best of our knowledge, out of plane measurements and out of plane inter-facial cracks have not been quantitatively studied yet, for single fibers or bundles during damage initiation and growth.

This paper investigates the microscopic damage behavior for three different single fibers, and a bundle of carbon fibers, embedded into the same epoxy matrix under quasi-static transverse loading. The fiber materials used were selected for their different bonding strength with the epoxy matrix. *In-situ* laser scanning confocal microscopy (LSCM) tensile testing was used to document the full field displacement and strain fields obtained through DIC analysis in addition to out of plane measurements. Each single fiber's bonding strength with epoxy is shown to affect inter-facial debonding initiation and growth. The experimental results include full field displacement and strain measurements, out of plane measurements, load cell force and cross-head displacement are provided as an additional dataset prepared to be user friendly and easy to explore. More specifically, the purpose of this study is :

- to provide accurate full field experimental measurements of inter-facial debonding and damage initiation in a fiber's vicinity
- to provide a better understanding of damage initiation and growth in a FRC quantitatively
- to provide full and complete experimental datasets that can be further compared with simulations to improve or benchmark micro-mechanical damage modelling

The full displacement and strain measurements, out of plane measurements, load cell force and cross-head displacement are provided as an additional dataset.

Section 7.3 introduces the materials and samples used. Section 7.4 presents the *in-situ* microtensile test setup used, along with the image acquisition apparatus and DIC settings. Section 7.5 presents the full field strain measurements for each specimen, along with the local strain measurements around reinforcements and the out of plane displacement measurements. Finally, Section 7.6 presents the differences in damage mechanisms, strain fields and out of plane displacements between strongly bonded and weakly bonded specimens, limitations of this work and additional elements deemed relevant for future comparison.

7.3 MATERIALS

7.3.1 Specimen fabrication

A mold was designed to manufacture three types of single fiber composites and a composite reinforced by a bundle of fibers. Figure 7.1a schematically shows the mold's front and right side views. The specimen's geometry was adapted from the ASTM D638 Type V standard geometry to accomodate the micro-tensile machine's geometry [123]. The molds were 3D-printed using a fused deposition modeling printer. The molds contained a path to maintain the reinforcement in place during matrix curing. Each mold was first coated with *Frekote 700-NC* releasing agent. The reinforcement was then inserted into the mold and both its ends were attached on the mold's outside surface. The red dashed line depicted in Figure 7.1a shows the reinforcement's position in the mold.

Ten parts by mass of Epon™ 862 resin was mixed with four parts of Epikure™ 3274 hardener to manufacture the matrix. The mixture was first degassed in a large plate to accelerate degassing for ≈ 30 minutes, poured into the mold, degassed again and then left to cure for 24 h at room temperature. Once cured, each mold was cut following the scissor lines shown in Figure 7.1a using an abrasive-waterjet cutting machine. This process was selected to prevent damage induced by traditional material cutting techniques [97]. Each slice obtained was manually extracted, providing a "dogbone" specimen similar to that shown in Figure 7.1b. Each specimen was then polished with silicon-carbide abrasive papers grit P320, P640, P800, P1200, P2000 and P4000, consecutively for a smooth finish.

7.3.2 Material properties

Four pure epoxy ASTM D638 Type I specimens were manufactured and mechanically tested according to ASTM D638 standard. The specimens were tested using a MTS Insight ® electromechanical testing machine equipped with a 25 kN load cell. Displacements were recorded using a 3D DIC setup (*VIC3D7* setup and software acquired from *Correlated Solutions*). Young's modulus and Poisson's ratio for the tested epoxy were then computed from the tensile test results and are presented in Table 7.1.

Four different reinforcements were used in this study: a single nickel plated high carbon steel fiber (HCS), a single polylactic acid (PLA) fiber, a single polytetrafluoroethylene (PTFE)

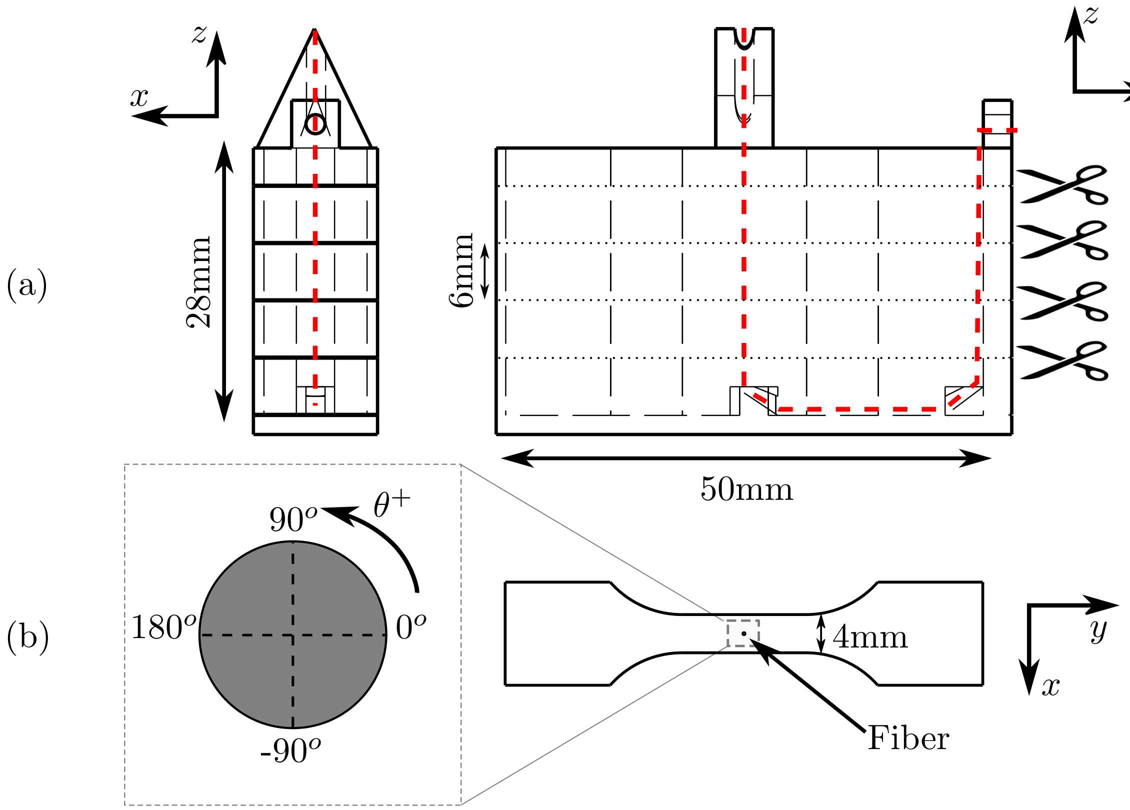

Figure 7.1 **(a)** Computer aided design of the 3D printed mold. The red dashed line shows how the reinforcement was held in the mold. The mold was cut using an abrasive-waterjet cutting machine along the scissor lines to obtain individual 6 mm thick dogbone specimens containing a single reinforcement transverse to the tensile direction. **(b)** Modified ASTM D638 Type V specimen with an embedded transverse fiber. Load is applied along the y direction

fiber and a bundle of carbon fibers (CF). The HCS fibers were a 200 µm diameter wires manufactured by *D'addario and company Inc.* The PLA-4032D fibers were manufactured using the solvent assited 3D-printing method [125] with a 200 µm diameter nozzle. The fiber's final diameter was 180 µm due to material evaporation after extrusion. The material was acquired as pellets from *Nature Works LLC*. The PTFE fibers were 711 µm diameter monofiber filaments and were acquired from *Zeus Inc.* Note that we did not succeed at acquiring PTFE wires having the same diameters as the other fibers. A bundle of fibers was cut from an Injectex GF420-E01-100 carbon fabric manufactured by *Hexcel*. Fiber diameters were measured using a LSCM for 30 fibers and the average diameter was found to be 7.5 µm $\pm$ 0.2. The CF were impregnated with the resin and hardener mixture prior to being deposited into the mold to improve bonding and minimize defects within the bundle.

Table 7.1 lists the elastic properties measured or obtained from each manufacturer. PTFE is a non-reactive synthetic polymer with a very low surface energy of 19 $^{\text{dynes}}/_{\text{cm}}$. This surface energy is not sufficiently high to create bonds with epoxy [100]. A surface energy higher than 30 $^{\text{dynes}}/_{\text{cm}}$ is usually required to bond with a cured epoxy [126]. Thus, a PTFE fiber inside an epoxy matrix can only be held through compressive forces due to the difference in coefficients of thermal expansion (CTE) between the matrix and fibers, and epoxy's shrinkage resulting from its curing process [5]. PLA's surface energy is slightly higher than PTFE's, 38 $^{\text{dynes}}/_{\text{cm}}$, which is sufficient to create a weak bonding with epoxies [127]. HCS has a surface energy of several hundred dynes and strongly adheres to epoxy [100]. An average surface energy for unsized carbon fibers was reported to be about 70 $^{\text{dynes}}/_{\text{cm}}$ [124, 128]. No sizing was applied on the CFs.

7.4 METHODS

7.4.1 Experimental setup

The experimental setup used in this work is schematically shown in Figure 7.2. Digital images with a resolution of 4096×4096 px^2 were acquired with a *LEXT OLS4100* Laser Scanning Confocal Microscope, manufactured by *Olympus* ©, while the specimen was loaded using a 5 kN *Kammrath and Weiss* micro tensile device. The specimen was deformed step-by-step with a regular macroscopic displacement increment ΔV of approximately 50 $\frac{\mu\text{m}}{\text{min}}$. At each step, the cross-head's displacement was held, and sufficient time was allowed ($\approx$ 1 min) prior to image capture to let the specimen fully relax. The load was continuously recorded during

Table 7.1 Studied materials elastic properties. Epoxy and PLA's Young's Modulus and Poisson's ratio were measured experimentally according to the ASTM D638 standard, a 95 % confidence interval was used. The PTFE and HCS's properties were provided as a range by their respective manufacturers

Material	Young's Modulus (GPa)	Poisson's ratio	Surface energy (dynes/cm)
Epoxy	2.45 ± 0.90	0.46	45
PTFE	$0.390 - 0.600$	0.46	19
PLA	2.70 ± 0.69	0.36	38
HCS	200	0.29	Strong
CF	-	-	70 [124]

the mechanical tests. The LSCM was equipped with a dual confocal system to limit out of plane measurements artifacts for composites with different reflecting characteristics.

Speckle pattern

Under the LSCM, local topographic variations induce local changes in reflectivity, depicted as grey levels using the laser intensity micrographs with sufficient contrast for DIC analysis [56, 60]. After being mirror polished with silicon-carbide grit paper up to P4000 grit, each specimen was gently polished manually in random directions for a dozen seconds around the fiber with P2400 and P1000 grit papers to produce random and very fine scratches intercepting together to form the speckle pattern.

Polishing was carried out incrementally and observed under the LSCM at each step to ensure that: (i) no large scratches were observed on the Region of Interest (ROI), (ii) a sufficiently large array of grey levels was visible in the ROI to distinguish every subset. Table 7.2 lists the observed area, scale, and height pitch for each specimen. The height pitch is the step used between two depth scans of the LSCM and represents the precision of the out of plane measurements' precision.

Selection of DIC parameters

A subset is a square zone centered around a given pixel the software is currently tracking and its size is expressed as a number of pixels. In subset based DIC, a subset from the initial image

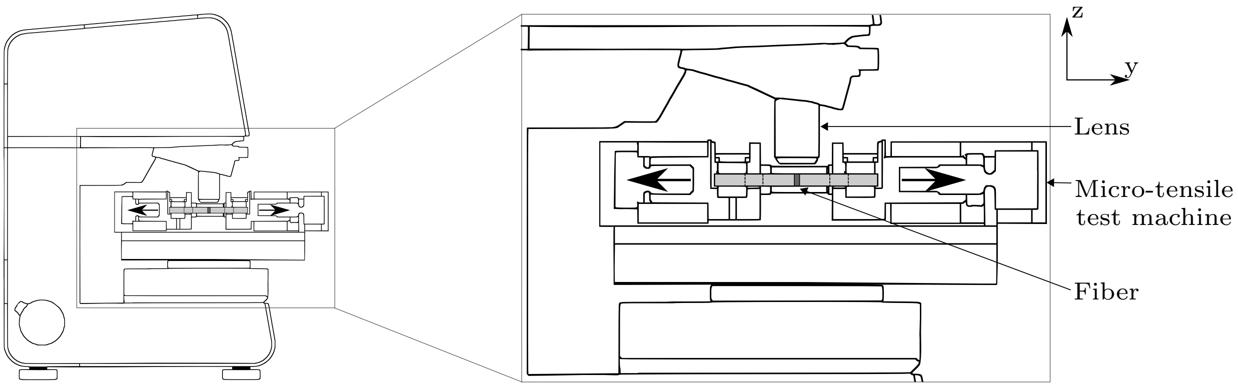

Figure 7.2 Schematic illustration of the LSCM paired with the microtensile device for in-situ full field strain measurements. The specimen is mounted into the micro-tensile test machine which is installed on the LSCM plate. The microscope's lens is then aligned with the fiber. The load is applied along the y direction and is shown with two black arrows.

(reference image) is compared with subsets from the current image (deformed image) until a subset better matching the initial image is found. Subsets are compared using a correlation function. The larger eigenvalue of the covariance matrix of the correlation equation is used to obtain the confidence margins, $\mathcal{C}$, for the displacements estimated by DIC for each pixel [56]. This value is representative of the error between a reference and deformed subset [60]. This information can then be used to measure the subset's displacement at a subpixel resolution, and thus the whole ROI's displacement field.

The step size is defined as the spacing between the points analyzed during correlation. Displacement values for pixels that are not tracked by the software (between two consecutive steps) are interpolated between tracked pixels, assuming a continuous displacement gradient [60]. A step of 2 means that one pixel out of two is tracked, with the displacement of the others being interpolated [60]. A step of size 2 was chosen to minimize the area lost around the crack and to minimize smoothing effects around discontinuities created by interpolation [56].

Lagrangian strains were computed using a filter size of 5 pixels to avoid over-smoothing the experimental data while computing strains. The strain computations use a filter size of 5 pixels. With the step set to 2, this means that the total smoothing area due to strain computation is of 10 pixels.

At some point, a subset distortion is so large that the confidence is too large to ensure pixel tracking. Features like the apparition of cracks typically lead to a loss of tracking [60]. A subset was considered untracked when the confidence margin exceeded an arbitrary threshold value of 0.1, as defined in *VIC3D*. Pixels for which tracking was lost were represented as white in the contour plots.

Large steps lead to faster computation, when compared to smaller steps, but decrease the measurements accuracy. However, small steps can induce large noise in strain computations. The optimal choice of subset and step is therefore a trade-off between the above mentioned

Table 7.2 Fiber diameter, size of the area observed and scale for each specimen studied. The height pitch, height step between two out of plane measurements, is also provided

Specimen	Fiber diameter (µm)	Observation area (µm × µm)	Scale ($\frac{\text{px}}{\mu\text{m}}$)	Height pitch (µm)
Epoxy / PTFE	711	2560×2560	1.6	5.00
Epoxy / PLA	180	1280×1280	3.2	2.00
Epoxy / HCS	200	1280×1280	3.2	2.00
Epoxy / CF	7.5 ± 0.2	256×256	16.0	0.06

beneficial and detrimental effects [56, 60]. Table 7.3 lists the subsets and steps that were used for displacement measurements using the subset suggestion tool available in VIC2D commercial software. The program computes the ideal subset size for an optimal match confidence of 0.01 pixel [60].

Out of plane measurements were simultaneously recorded when capturing the laser intensity micrographs for in plane full field measurements. A stabilization algorithm was applied on each image to remove the microscope's rigid body motion during the experiment prior to DIC analysis.

7.5 RESULTS

7.5.1 Single fiber

ε_x, ε_y and ε_{xy} contour plot time-lapses for the PTFE / epoxy, PLA / epoxy and HCS /epoxy specimens are respectively shown in Figures 7.3, 7.4 and 7.5. The reference coordinate axes used (x, y and z) are presented in Figures 7.1 and 7.2. Strain measurements were provided in PLA fibers while it was not possible to accurately measure strains in the HCS and PTFE fibers due to their highly reflective surfaces that saturated the fibers with white pixels.

Strain evolution

Strain component ε_y localized at the 90° and -90° areas for the PTFE / epoxy specimen (see Figure 7.3a). For the PLA / epoxy specimen, ε_y localized around the 0° and 180° inter-facial areas (see Figure 7.4a). The maximum ε_y recorded at this location was about twice the applied strain for the PTFE / epoxy specimen and more than seventeen times higher for the PLA / epoxy specimen. Figure 7.3a also shows that a crack appeared at the top and bottom of the PTFE / epoxy interface for $\bar{\varepsilon} = 0.5$ %. An inter-facial crack is also clearly visible at the top of the PLA fiber, where ε_y localized (Figure 7.4a). The HCS / epoxy specimen also exhibits a large inter-facial crack extending from 135° to -90° (Figure 7.5a). The ε_x and ε_{xy}

Table 7.3 Subset and step parameters selected for each test analysis

Fiber	Subset	Step
PTFE	91	3
PLA	99	3
HCS	99	3
CF bundle	93	3

strain components (Figures 7.3a, 7.4a, and 7.5a) are relatively smaller, when compared to ε_y at the beginning of the tests.

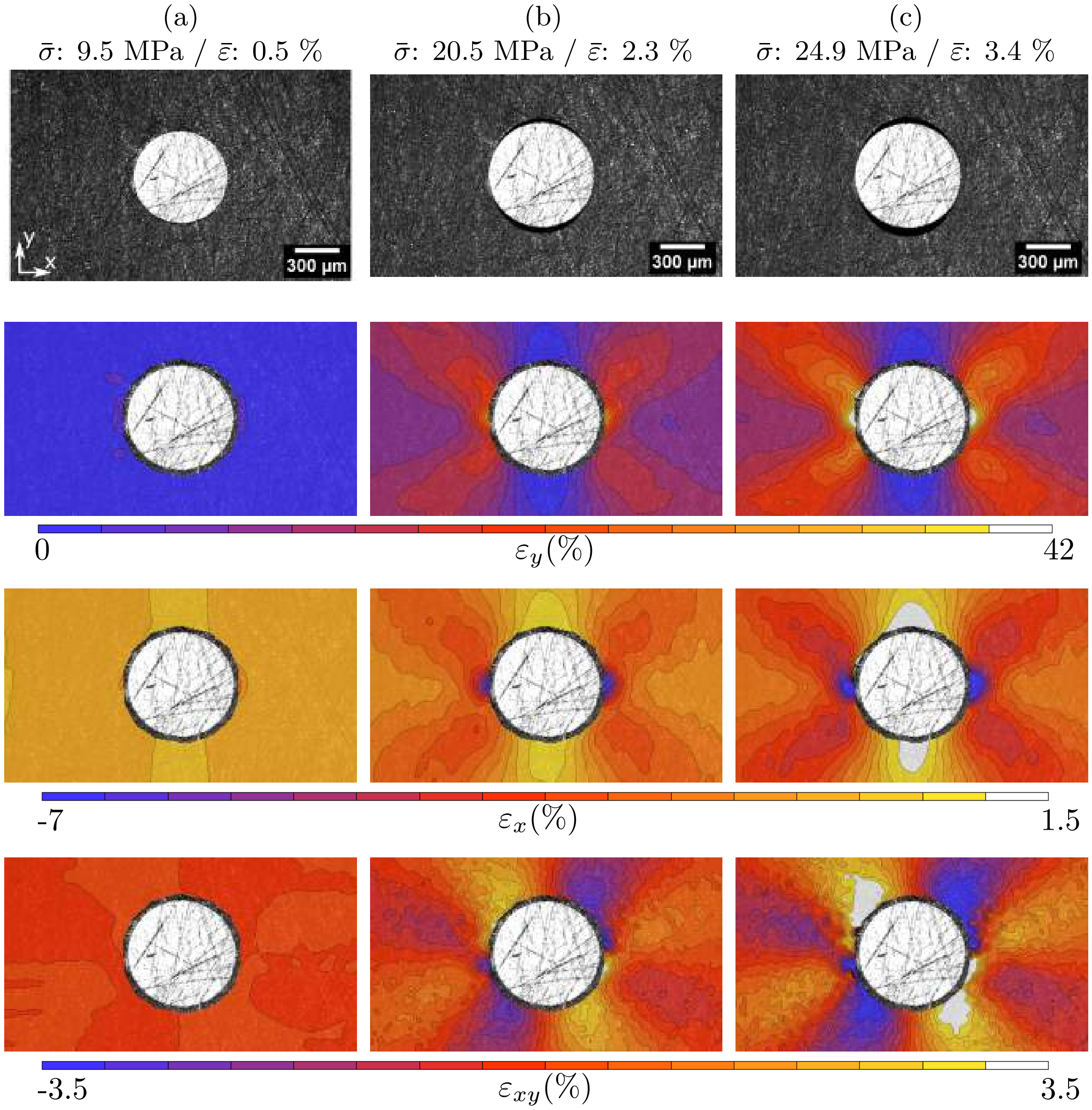

Figure 7.3 **PTFE/epoxy** single-fiber composite loaded in tension in the y direction. Column (a) includes images taken before an inter-facial crack appeared between the fiber and matrix. Column (b) includes images taken after an inter-facial crack appeared. Column (c) includes images taken before DIC tracking was lost. The global stress and strain values for each column are provided at the very top of the figure. The first row shows the raw images. The second and third rows present the strain contour plots in the y and x directions, and the last row presents the shear strain xy

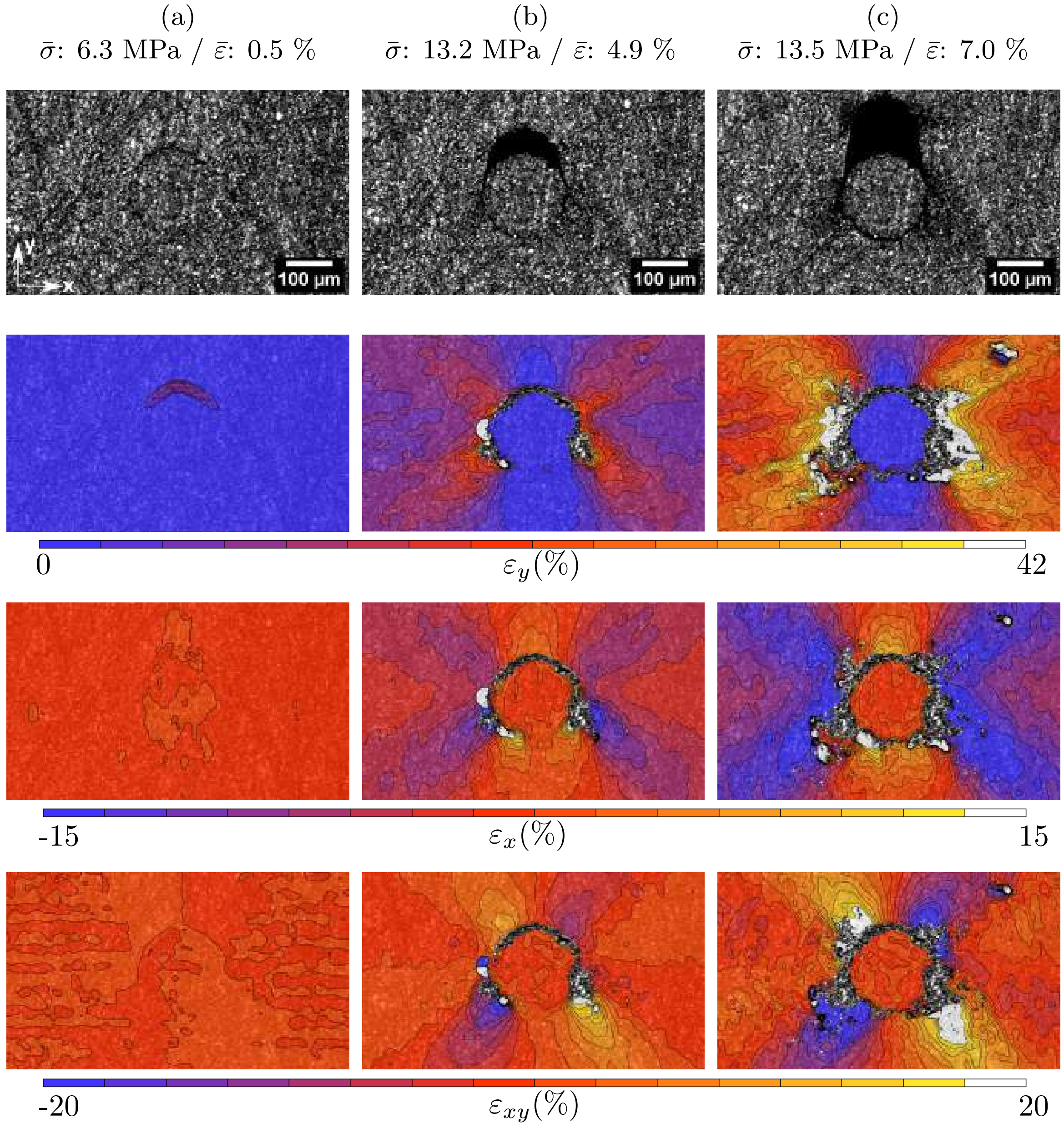

Figure 7.4 **PLA/epoxy** single-fiber composite loaded in tension in the y direction. Column (a) includes images taken before an inter-facial crack appeared between the fiber and matrix. Column (b) includes images taken after an inter-facial crack appeared. Column (c) includes images taken before DIC tracking was lost. The global stress and strain values for each column are provided at the very top of the figure. The first row shows the raw images. The second and third rows present the strain contour plots in the y and x directions, and the last row presents the shear strain xy

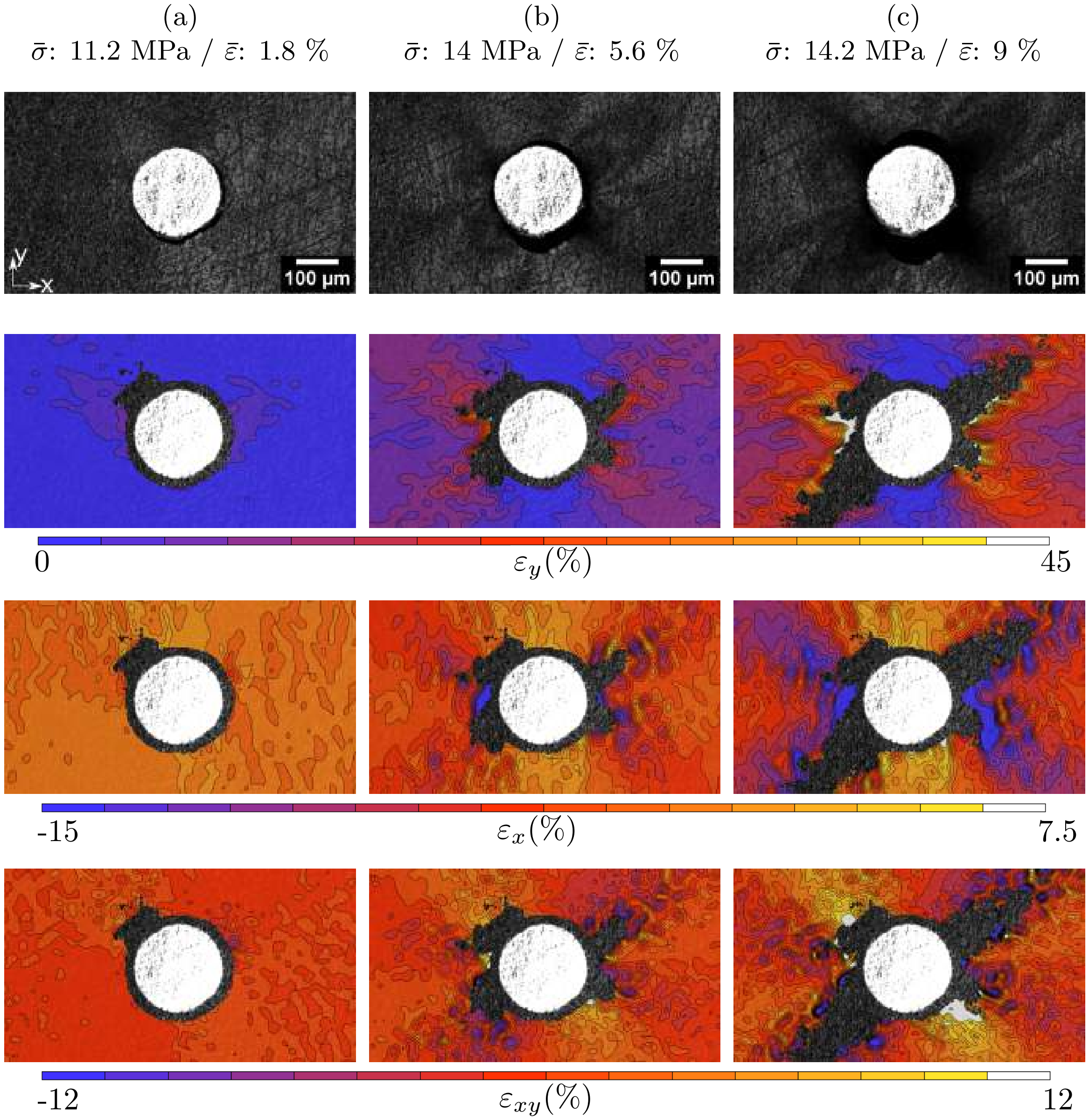

Figure 7.5 **HCS/epoxy** single-fiber composite loaded in tension in the y direction. Column (a) includes images taken before an inter-facial crack appeared between the fiber and matrix. Column (b) includes images taken after an inter-facial crack appeared. Column (c) includes images taken before DIC tracking was lost. The global stress and strain values for each column are provided at the very top of the figure. The first row shows the raw images. The second and third rows present the strain contour plots in the y and x directions, and the last row presents the shear strain xy

As the load increases, the inter-facial crack located at the top and bottom of the PTFE fiber keeps growing. Figure 7.3b shows how ε_y builds up into a cross shape centered on the PTFE fiber with the highest ε_y strain located along the diagonals (45°, 135°, -135°, and -45°). The ε_y maximum eventually localized at the interface along the +90° and -90° inter-facial areas. ε_x also forms a cross shape around the fiber, with its peak located at the top and bottom of the fiber. The cross shape encompasses a gradient of compressive strains, with the maximum (-7 %) precisely localizing at the -90° and +90° areas around the interface. ε_{xy} is symmetrically distributed around the fiber with its maximum (3.5 %) localized around the -135° and +45° areas, while the minimum (-3.5 %) is located around the 135° and -45° areas. ε_{xy} is close to 0 next to the 0° and 180° areas around the fibers while the extrema are located around the 45°, 135°, -135° and -45° inter-facial areas. Figure 7.3c shows that the ε_y, ε_x and ε_{xy} fields exhibit a similar shape as the load increases. Both cracks (0° and 180°) keep growing with that at 180° becoming slightly longer.

The PLA specimen's inter-facial crack opened at 0°. The top crack is about 60 µm long in Figure 7.4b. An inter-facial crack is also growing all around the fiber. The top crack reached a length of up to 130 µm for a global strain applied of 7 %, as shown in Figure 7.4c. Short lateral cracks are visible in the matrix next to the interface at -100° and 100°. Other cracks, which are opening in Mode I, are also visible along the top inter-facial crack's right hand side. DIC tracking is gradually lost along the crack path. The behavior of ε_y for the PLA fiber is similar to that described for the PTFE / epoxy specimen: the strain levels are similar, except for the maximum, which is spread over larger areas between [45°;135°] and [-135°;$-$45°] around the interface (Figure 7.4c).

The ε_x strain field in the PLA fiber is similar to that observed in the PTFE / epoxy specimen. Although the minimum of ε_x (-9 %) is also located around the interface at the 90° and -90°, the area over which it spreads is larger than that observed in the PTFE / epoxy specimen. The ε_{xy} field for the PLA / epoxy specimen is also similar to that observed for the PTFE / epoxy sample. Figure 7.4c shows that, although the crack is visible all around the fiber, only the top inter-facial crack keeps growing and is as wide as the fiber itself, for $\bar{\varepsilon} = 7.0$ %.
By opposition, for the HCS / epoxy specimen, untracked pixels appeared early on during the test. The area over which untracked pixels appeared throughout the test is the cross shaped area over which ε_x was the most compressive and ε_y was high for the other specimens, as shown in Figures 7.5b and 7.5c. The ε_y, ε_x and ε_{xy} strain fields have distributions similar to those measured in the PLA / epoxy and PTFE / epoxy specimens.

Tangential strain

We define ε_y^T as the averaged ε_y strain measured over two discs on the right (-90°) and left (90°) hand side of each fiber. Figure 7.6 shows ε_y^T measurements around the fiber, for each specimen. While the top and bottom crack open under Mode I, the cracks on the left and right sides of fibers open under Mode II, as shown by the ε_y fields presented in Figures 7.3, 7.4, and 7.5. ε_y^T represents tangential opening which induces Mode II opening [9]. ε_y^T growth rate is similar for every sample up to around 3.5% global strain. After this threshold, ε_y^T grows rapidly in the PLA / epoxy and PTFE / epoxy specimens, while its growth is significantly slower in the HCS / epoxy specimen. This behavior suggests that tangential debonding occurred much faster in the PLA / epoxy and PTFE / epoxy specimens than in the HCS / epoxy specimen, which is consistent with the inter-facial strength reported in Table 7.1.

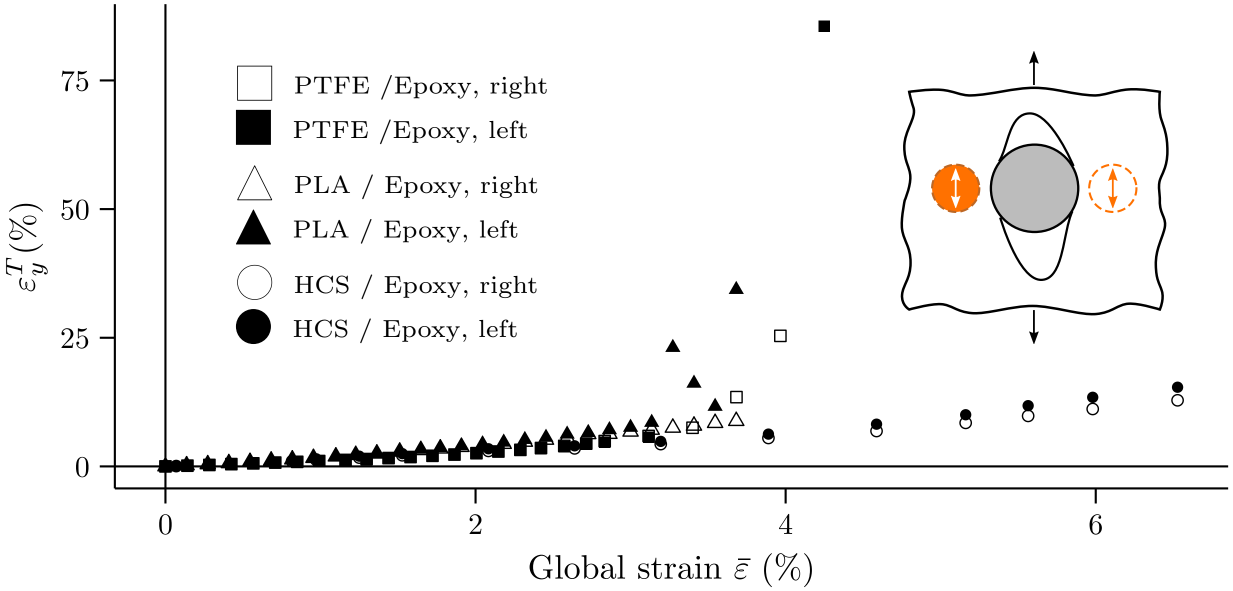

Figure 7.6 The average strain ε_y^T is plotted for two positions around the fiber, for each specimen. The average strains of pixels within two discs about half a subset away from each fiber were computed and plotted. Each disc is about 2/3 of the size of the fiber it is next to. ε_y^T growth rate is about the same for all three specimens before 3% global strain. It then strongly increases for the PLA / epoxy and PTFE / epoxy specimens, while it increases steadily for the HCS.

Virtual extensometers

Figure 7.7 shows the strain that would have been measured by an extensometer located near the fiber / matrix interface as a function of the global strain $\bar{\varepsilon}$. Two pixels were selected about a subset away from the fiber / matrix interface, in the x and y directions, for every specimen. The local strain was computed from the pixels displacement as: $\varepsilon^l = \frac{\Delta L}{L_0}$, where L_0 is the initial distance between the two selected pixels and ΔL the distance variation between both pixels. ε^l_y was measured along the y direction, and ε^l_x along the x direction. ε^l_y provides insights on the inter-facial crack opening along the y direction.

Figure 7.7a shows the strain measured by the virtual extensometer aligned along the y direction near the fiber / matrix interface. Although ε^l_y grows with about the same rate for every specimen, its opening rate in PTFE / epoxy and PLA / epoxy specimens accelerates after around 1% while it remains constant for the HCS specimen up to about 3%. Note that ε^l_y's opening rate is slitghly faster in the PLA / epoxy specimen than that measured in the PTFE / epoxy specimen. This behavior is consistent with the PTFE / epoxy bonding strength. After $\bar{\varepsilon} \approx 2.5$ %, ε^l_y in the PTFE / epoxy specimen significantly increases up to 40%, opening much more and faster than what is observed in the PLA / epoxy specimen. The ε^l_y strain rate in the HCS / epoxy and the PLA / epoxy specimens gradually increases quasi linearly, with the opening rate for the PLA / epoxy specimen faster than that of the HCS / epoxy specimen. The PLA / epoxy specimen has a weaker inter-facial bonding than the HCS / epoxy specimen which is consistent with their respective opening rates. The results quantitatively show that ε^l_y is affected by the fiber / matrix couple's bonding strength.

Figure 7.7b presents the strain measured by the virtual extensometer aligned along the x direction near the fiber / matrix interface. The PTFE / epoxy and PLA / epoxy specimens ε^l_x grow at the same rate up to an applied global strain of about 2%. ε^l_x measured for the PLA / epoxy specimen becomes more compressive than that observed in the PTFE / epoxy specimen. Moreover, ε^l_x's growth rate for the PTFE / epoxy specimen accelerates after a global strain of 3%. The behavior of the HCS / epoxy specimen is significantly different. Under an applied strain rate of 2%, ε^l_x is slightly positive or about 0%, showing that the extensometer marginally undergoes tension at first along the x axis. It then becomes compressive, and decreases quasi-linearly with a slower rate than the two other specimens. This behavior is attributed to the stronger bonding of the HCS fiber with the epoxy matrix.

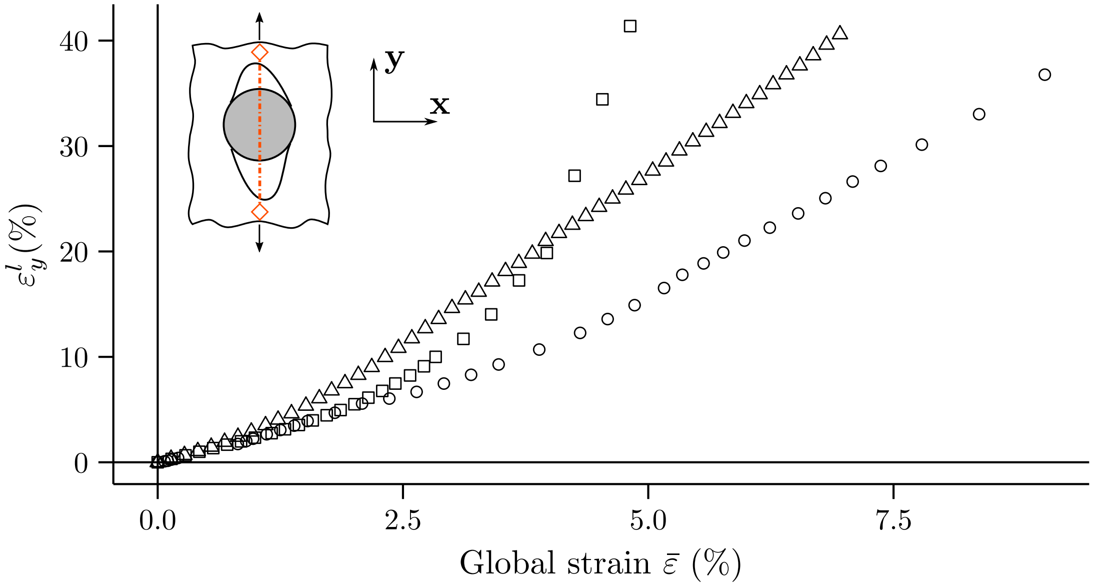

(a)

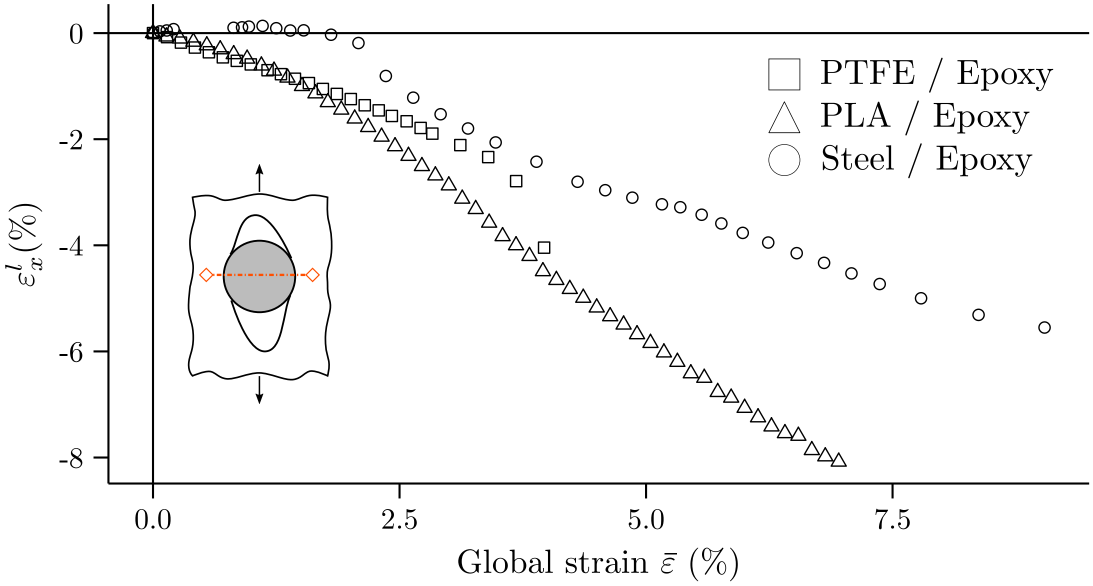

(b)

Figure 7.7 ε_x^l and ε_y^l are shown as a function of the global strain applied on the specimen $\bar{\varepsilon}$. ε_x^l and ε_y^l are obtained by applying a virtual extensometer around the fibre/matrix interface, as shown on the schematics in Figures **a** and **b**. ε_x^l measures the strain applied by the matrix on the fiber along the x direction. ε_y^l measures the strain applied by the matrix on the fiber and the opening of the inter-facial fiber, along the y direction

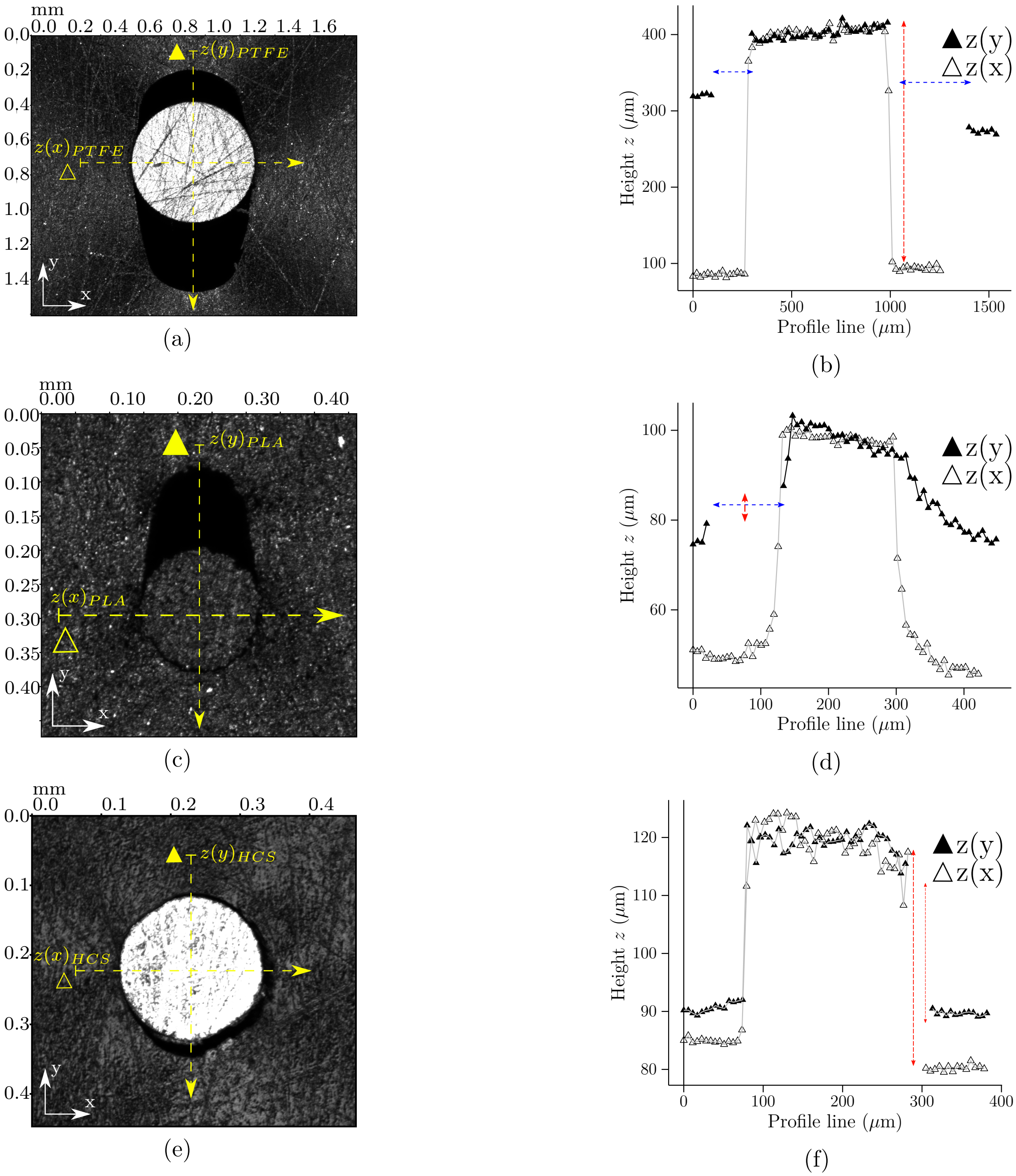

(a) (b) (c) (d) (e) (f)

Figure 7.8 Height measurements along longitudinal and transverse profile lines for each single fiber specimen. The left hand side shows the fiber along with the x and y profile lines over which the z coordinate is extracted. The right hand side shows the actual plots for the z coordinates. Figures **(a)** and **(b)** present these results for the **PTFE / epoxy** specimen at the same global strain as Figure 7.3c; Figures **(c)** and **(d)** for the **PLA / epoxy** specimen and Figure **(e)** at the same global strain as Figure 7.4c and **(f)** the **HCS / epoxy** at the same global strain as Figure 7.5c. Blue dashed lines were added to the plots to highlight in plane cracks and red dashed lines for the out of plane cracks

Out of plane measurements

Out of plane measurements are independent of the DIC measured displacements and computed strains as they were obtained solely using the data provided by the microscope.

Figure 7.8 presents $z(x)$ and $z(y)$ out of plane measurements along profile lines oriented in the x and y directions, at the last time step (corresponding to Figures 7.3c, 7.4c and 7.5c). Figure 7.8 shows that each fiber is protruding above the matrix that underwent compression due to Poisson's effect, for all specimens.

Figure 7.8a shows $z(y)$ and $z(x)$ for the PTFE / epoxy specimen. $z(y)$ exhibits two gaps resulting from the 0^o and 180^o in plane inter-facial cracks shown in Figure 7.8b. Two clear discontinuities can be seen in the $z(y)$ height profile (highlighted with blue dashed lines in Figure 7.8b), showing that out of plane inter-facial debonding clearly happened due to the tunneling effect. The difference in height between the fiber's free surface and the matrix - the out of plane inter-facial crack - along the x axis is about 390 µm and is shown as a red dashed line in Figure 7.8b.

Figure 7.8c shows that a large in plane top crack (0^o) is clearly visible and is about 200 µm long in the PLA / epoxy specimen. Figure 7.8d presents $z(y)$ and $z(x)$ for the PLA / epoxy specimen. Note that the portion of $z(y)$'s profile where there is no reported value (shown as a blue dashed line) corresponds to the crack's location. It also shows the 180^o inter-facial crack which appears as a gradual height decrease, from 300 µm onward. The fiber's top free surface appears to be tilted toward the 180^o crack. These two observations suggest that the fiber is still bonded to the matrix, only angles ranging from $\approx 135^o$ to -135^o.

Figure 7.8e presents similar results for the HCS / epoxy specimen. An in plane inter-facial crack is visible at 180^o and -90^o, as presented on the micrograph. $z(y)$ and $z(x)$ profiles show that the out of plane inter-facial crack is more than 30 µm wide (shown with red dashed lines), which is about three times larger than the in plane inter-facial crack. The transition from the fiber to matrix is similar to the profiles presented for PTFE / epoxy (Figure 7.8b), except that the in plane crack is less than 10 µm long.

7.5.2 Carbon Fiber bundle

Figure 7.9 shows the CF / epoxy specimen's studied area. Two areas were selected as ROIs. The larger area (ROI CF1) contains about one hundred CFs loosely gathered in a bundle. A surface manufacturing defect is also visible in ROI CF1 (dark area). The second area (ROI CF2), on the left, shows a small bundle containing five CFs and a single fiber isolated on the top left. Images were acquired when the confocal microscope's plate was moved from one area to the other after the mechanical loading pauses.

Strain evolution and damage

Figures 7.10 and 7.11 show ε_x, ε_y and ε_{xy} strain field contour plots for ROI CF1 and ROI CF2, respectively, for arbitrarily chosen load levels.

The first row of Figure 7.10 shows how the strain localizes and that damage develops around a relatively large bundle of CFs. Damage appears as inter-facial cracks growing at the bundle's top and bottom. It is worth noting that the macroscopic crack at the bundle's top (0°) and bottom (180°) developed due to the coalescence of individual inter-facial debonding cracks. Damaged interfaces are located in the bundle's periphery along the 90° and −180° areas, which is similar to what was observed in single fiber composites when the bundle is assimilated as a single fiber. These cracks are highlighted in Figures 7.10b and 7.10c as yellow arrows. Similarly to the single fiber, ε_y's maximum is localized along the 0° and −180° edges of the bundle. ε_x's maximum and minimum are localized along the 90° and -90° areas, respectively. Figures 7.10b and 7.10c also show that ε_x, ε_y and ε_{xy} fields remain close to 0 % within the bundle's core and exhibit concentrations along its edge. ε_y's maximum value is about 6 times higher than the global applied strain in Figure 7.10c.

Figure 7.11 shows the ε_y, ε_x and ε_{xy} fields for ROI CF2. Similarly to the larger CF bundle,

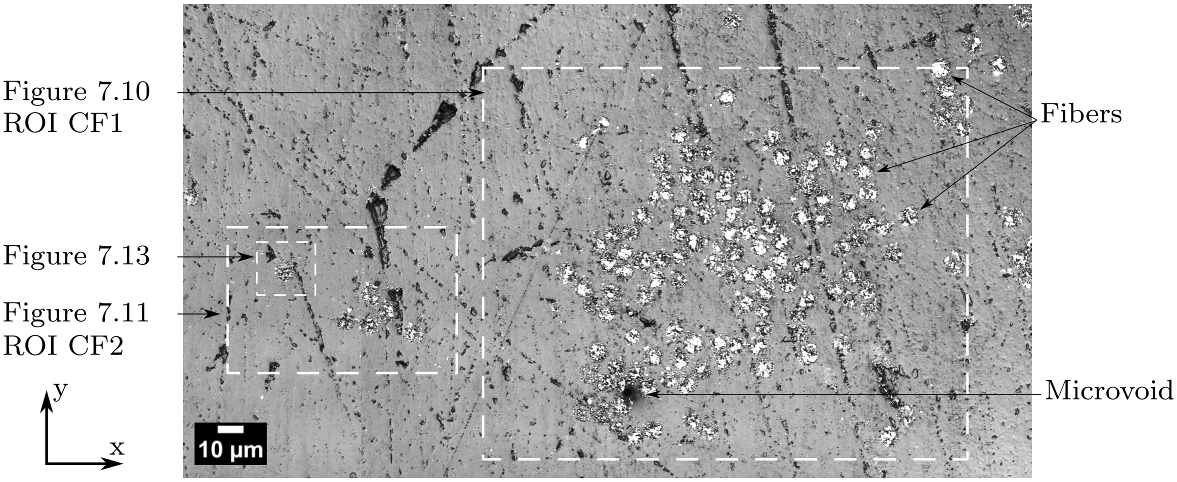

Figure 7.9 Micrograph of the area of interest studied for the **CF/epoxy**. The **area on the left** contains a small bundle containing five carbon fibers and a single fiber on the top left. The **area on the right** contains a bundle of carbon fibers with about a hundred fibers. Within the area on the left, a single carbon fiber was arbitrarily selected to perform in plane and out of place crack size measurements, which are presented in Figure 7.13

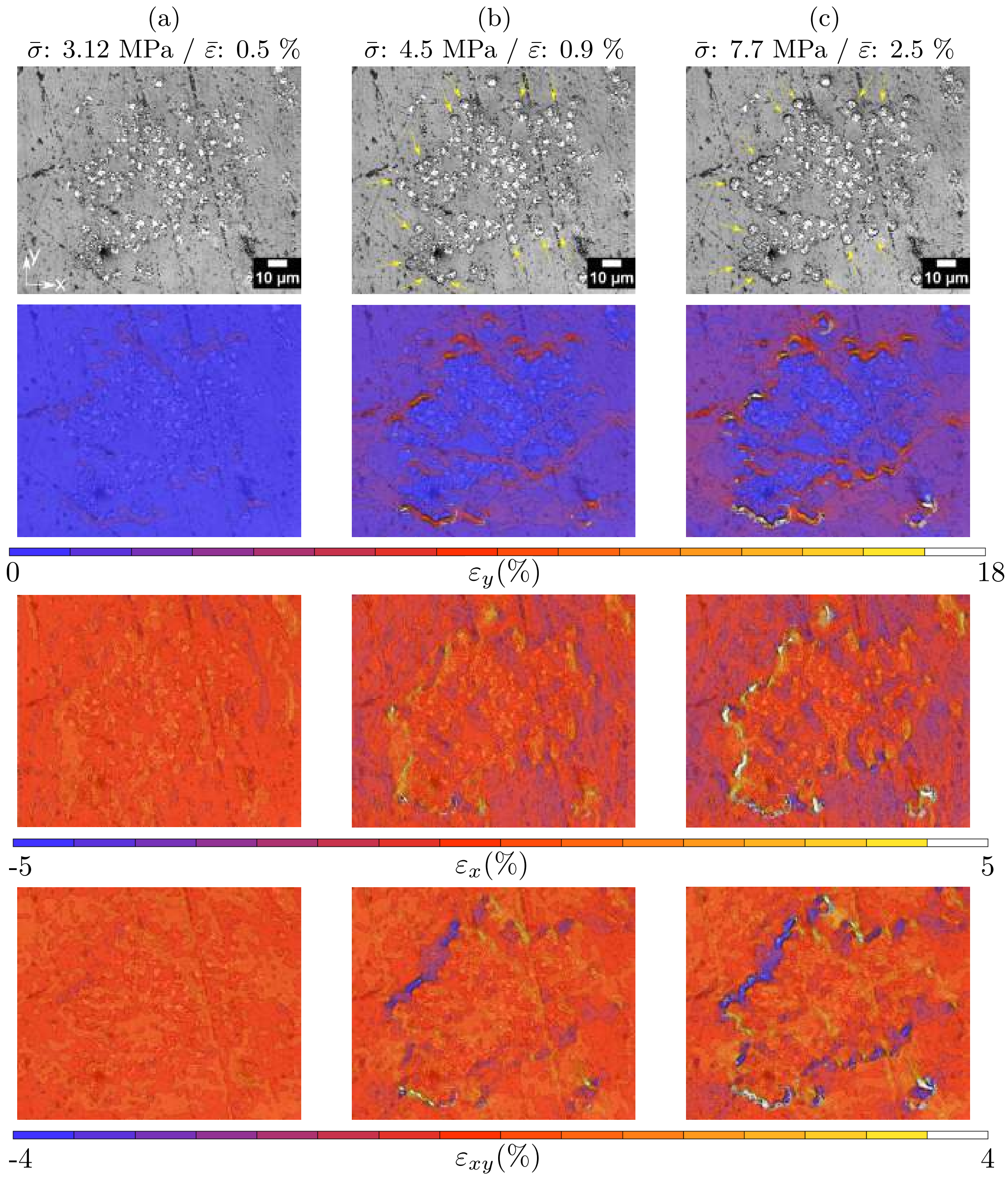

Figure 7.10 Timelapse of **CF** bundle / **epoxy** composite loaded in tension in the y direction, this figure presents results for the area on the **right hand side**, ROI CF1, in Figure 7.9. The bundle contains about 100 CFs. Column (a) includes images taken before any damage is visible on the image. Column (b) includes images taken after an inter-facial cracks started appearing. Column (c) includes images taken before DIC tracking was lost. The global stress and strain values for each column are provided at the very top of the figure. The first row shows the raw images. The second and third rows present the strain contour plots in the y and x directions, and the last row presents the shear strain xy

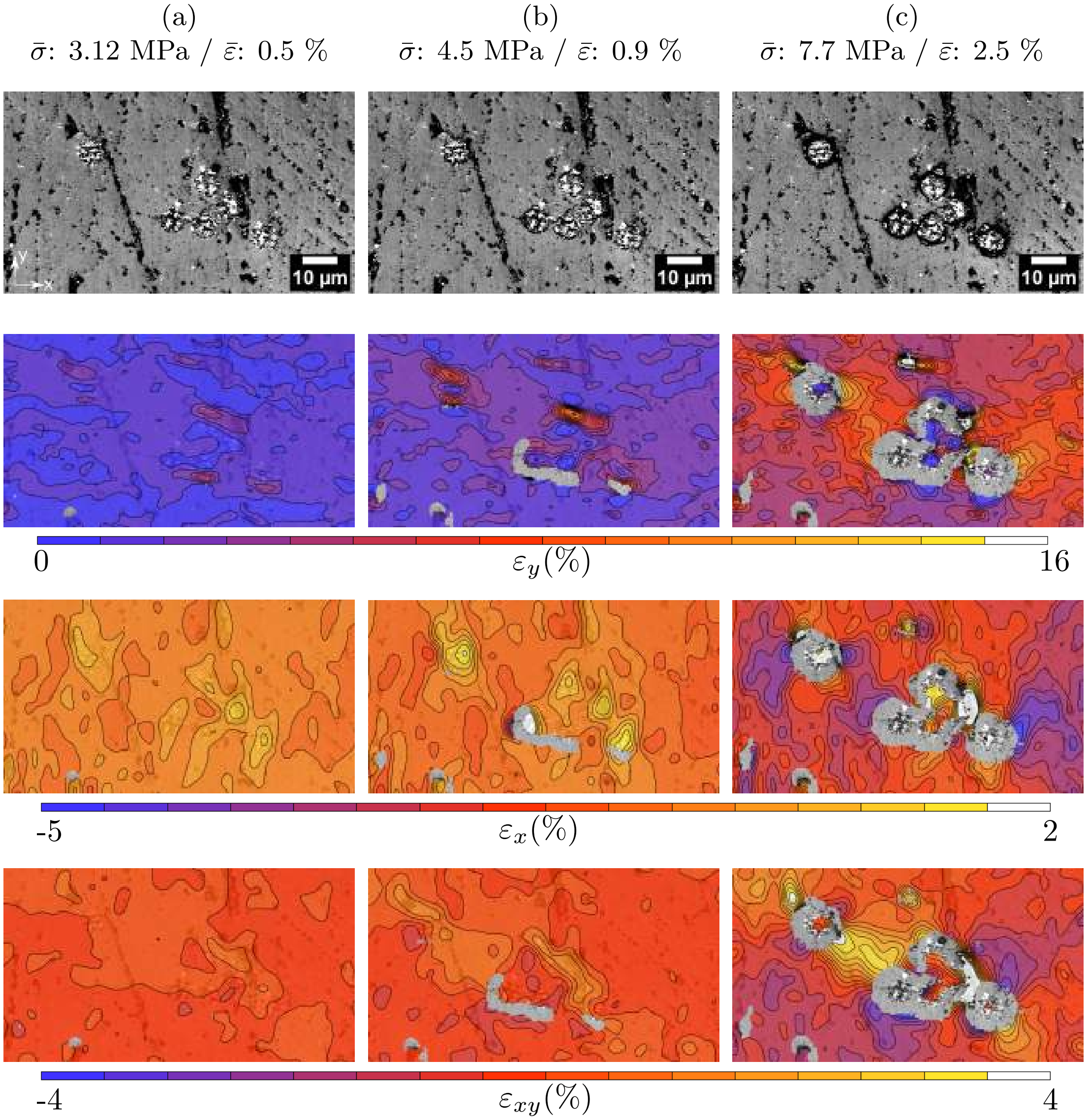

Figure 7.11 **CF** bundle / **epoxy** single-fiber composite loaded in tension in the y direction for ROI CF2, in Figure 7.9. The bundle contains five CFs and an isolated fiber. Column (a) includes images taken before any damage is visible. Column (b) includes images taken after an inter-facial cracks appeared. Column (c) includes images taken before DIC tracking was lost. The global stress and strain values for each column are provided at the very top of the figure. The first row shows the raw images. The second and third rows present the strain contour plots in the x and y directions, and the last row presents the shear strain xy

damage initiates with debonding around the bundle's 0° and -180° edges (Figure 7.11b). Pixel tracking is gradually lost around the small bundle and the single fiber due to the apparition of inter-facial cracks. The single fiber isolated on the top left corner of ROI CF2 is also, at this point, experiencing partial debonding. The ε_x and ε_y strain fields around the single fiber are similar to those observed for the single fiber composites. ε_y is maximal around the 0° and 180° of the single fiber while ε_x exhibits strain concentrations around the single fiber (Figure 7.11b), forming a cross shape similar to those observed for the PTFE / epoxy, PLA / epoxy and HCS / expoy specimens. ε_{xy}'s distribution is also similar to that of single fibers, revealing a symmetrical shape with maximums at 45° and -135° and minimums with opposite values at 45° and -135° along the carbon fiber / epoxy interface. Figure 7.11c shows that inter-facial debonding progresses on the edges of the small bundle, without affecting its core. Inter-facial debonding also grows through the whole interface of the isolated fiber, completely debonding it. No debonding was visible around the fiber / matrix interface at the bundle's core, throughout the whole mechanical test.

Out of plane displacements

Figure 7.12 presents out of plane measurements for the CF / epoxy composite. The area presented is the same as that shown in Figure 7.9, for $\bar{\sigma} = 4.5$ MPa and $\bar{\varepsilon} = 2.5\%$ as shown in Figures 7.10c and 7.11c.

Following polishing, variations in out of plane measurements were found to be less than 2.5 µm for the area presented in Figure 7.9 (although the unloaded out of plane measurements were not presented in this work, they are available in the data package). Figure 7.12 shows that the surface observed, has now severely been deformed in the out of plane direction. The fibers within the large CF bundle, as detailed in Figure 7.10c, are now protruding out of the material at a height of about 12 µm above the average height of the matrix far away from the bundle. The matrix has experienced compression along the out of plane direction z due to the strain applied in the y direction (Poisson's effect). Matrix areas entrapped within the fibers at the core of the bundle also appear to not have experienced any out of plane compression as their average height is about 10 µm. This delay in inter-facial cracking between the bundle's core region and its edges is attributed to the strong matrix / fiber interface. The smaller fiber bundle detailed in Figure 7.11c is also protruding out of the matrix, as shown in Figure 7.12. The average height of the smaller bundle is about 8-10 µm smaller than that of the larger bundle and also appears to continuously decrease from the bundle's center down to the matrix. Single fibers are also protruding out of the matrix, showing a clear discontinuity in out of plane measurements.

Figure 7.13a shows a cropped area around the single fiber shown in Figure 7.9 for a stress level of 7.7 MPa (e.g., Figure 7.11c). The vertical and horizontal slide rulers show that the in plane inter-facial crack (black area around the fiber) is about 2 μm at most. Figure 7.13b presents height measurements along the two profile lines (oriented along x and y) shown in Figure 7.13a. $z = 0$ was selected as the minimum out of plane value measured within Figure 7.13a and is not visible in Figure 7.13b. The plateau at about 7 μm of height corresponds to the CF's free surface. The plot shows that out of plane measurements sharply decrease along the x and y directions away from the fiber at first, then decrease progressively, as it can also be observed from Figure 7.12. The out of plane inter-facial crack is about 2 μm at least, which is about the same size as the in plane inter-facial crack. The debonding profile observed is similar to that observed for the HCS / epoxy specimen presented in Figure 7.8f.

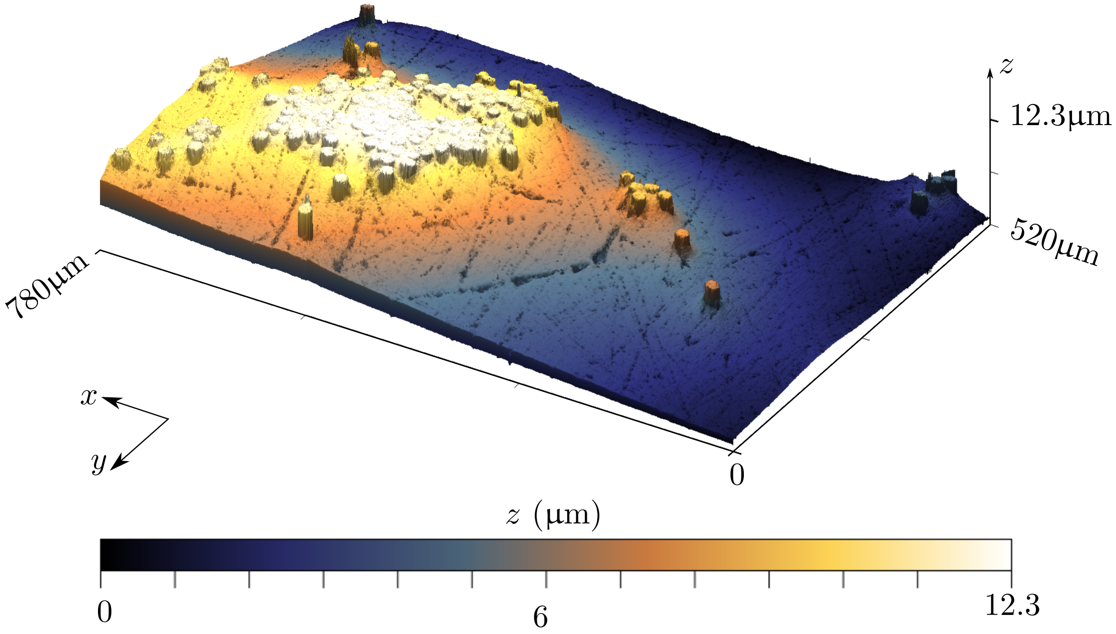

Figure 7.12 3D surface profile of the area presented in Figure 7.9 for $\bar{\varepsilon} = 2.5$ % (see Figures 7.10c and 7.11c). Height measurements are obtained using the laser confocal microscope [129]. A large bundle (≈ 100 fibers), a smaller bundle (≈ 5 fibers) and single fibers are visible, along with their out of plane displacement, shown as a contour plot

7.6 DISCUSSION

7.6.1 Strong and weak bonding

The PTFE, PLA and HCS single fibers studied in this work were selected based on their bonding strengths with epoxy, thus providing a case with no interface (PTFE), a case with a weak bonding (PLA), and a case with strong bonding (HCS). The interface strain localization strongly depended on the interface toughness (Figure 7.6, 7.7a and b). The HCS / epoxy composite was shown to behave differently than the PTFE / epoxy or PLA / epoxy when submitted to transverse loading in Section 7.5.1. Figure 7.6 shows that $\varepsilon_{\mathrm{y}}^{\mathrm{T}}$ increases at a faster rate than linear rate with respect to the applied global strain for the PTFE / epoxy composite and faster than that observed for the PLA / epoxy and HCS / epoxy composites. By opposition, $\varepsilon_{\mathrm{y}}^{\mathrm{T}}$ for the HCS / epoxy specimen shows that strong bonding hinders tangential opening (Mode II) around the inter-facial areas at 90° and -90°. Figure 7.7b also shows that the compressive strain applied by the matrix on the HCS fiber is negligible before $\bar{\varepsilon} = 2$ %. The matrix even appears to be pulling on the fiber, as ε_x^l is positive for the HCS / epoxy specimen at the beginning of the test. This behavior is unique to the HCS / epoxy specimen. Strong bonding could explain this behavior as it was also observed in a previous

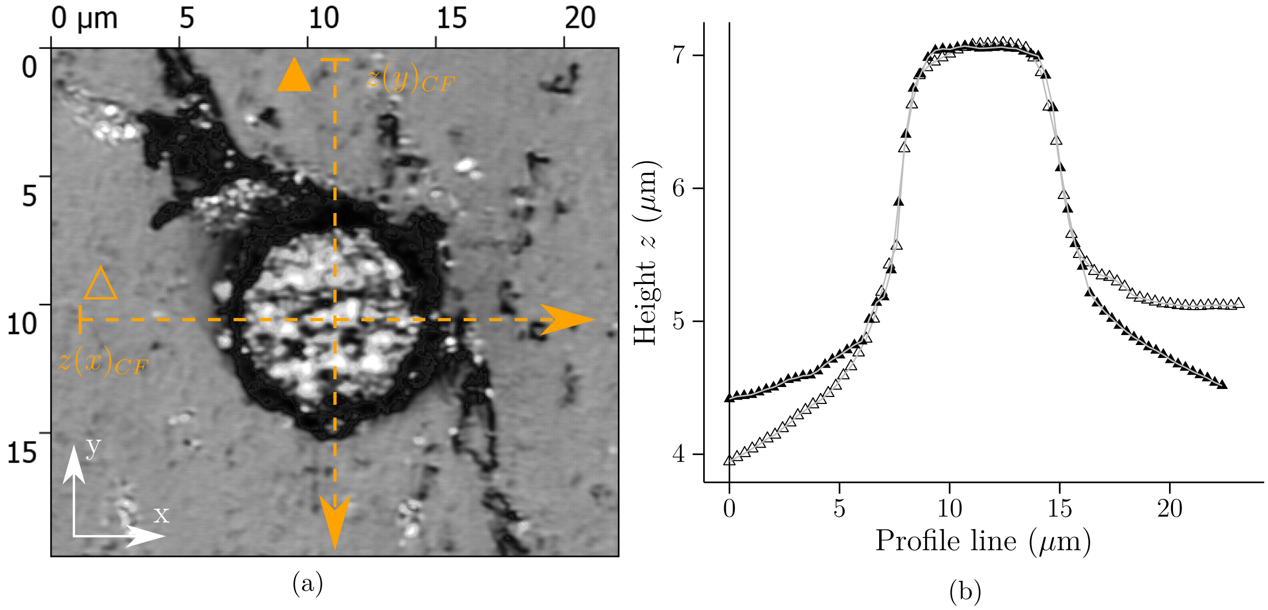

(a)

(b)

Figure 7.13 **(a)** Cropped area around the single fiber shown in Figure 7.9. Vertical and horizontal side rulers are provided and show that the in-plane inter-facial crack appears to be about 2 µm wide at most. **(b)** Height measurements along two profile lines shown in (a). The top of the CF is visible as a plateau at about 7 µm. The out of plane crack, distance between the matrix height and top of the CF, is about 2 µm wide work involving 1 mm galvanized steel fibers in two different epoxies [1].

While the bundle of CFs is composed of clusters of single CFs, damage first occurs at the bundle's interface with the martix due to the coalescence of individual cracks located at the fiber / matrix interface of fibers at the bundle's periphery, while no particular damage was observed within its core. This early damage localization is analogous to that investigated in single fiber reinforced composites, when the fiber bundle is considered as a single fiber.

7.6.2 Damage initiation

Damage initiation and growth of the inter-facial crack for single fiber specimens happen differently for each configuration. Figure 7.7a shows that the inter-facial crack immediately starts growing as ε_y^l increases from the very beginning of the test, although the crack is not yet visible on the micrographs due to the optical setup resolution.

The inter-facial crack around the PTFE fiber in Figure 7.3a appears to only be present at the 0° and 180° areas. Later on during the test (Figures 7.3b), no sign of inter-facial debonding is visible around the 90° and -90° inter-facial areas. Both cracks (0° and 180°) appear to be symmetrically growing at the same rate.

For the PLA / epoxy specimen, Figure 7.4a shows that an inter-facial crack starts growing around the 0° inter-facial area. For this specimen, inter-facial decohesion is also visible all around the fiber as a discontinuity. Figure 7.4b also shows that the crack growth is not symmetric, as only the 0° crack keeps growing. These two differences in behavior, with respect to those observed for the PTFE / epoxy specimen, are attributed to the weak bonding of PLA / epoxy. As out of plane and in plane debonding occurs, the inter-facial crack visibly grows around the fiber, which is not the case for the PTFE / epoxy specimen as there is no bonding in that case. Inter-facial bonding might arbitrarily be stronger in the 180° inter-facial area, promoting debonding around the 0° inter-facial area.

The inter-facial crack of the HCS / epoxy specimen debonded between 135° and -90° in the interface (Figure 7.5a). The crack initiation and growth is not symmetric in this case. The inter-facial area around 90° appears to remain bonded throughout the whole test, favoring inter-facial crack growth between 135° and 45° (Figure 7.5b and c).

7.6.3 Fiber size effect

The size of the inter-facial debonding crack might depend on the materials' mechanical properties, bonding strength and fiber diameter [9,26]. A previous study involving two different epoxy matrices with a larger PTFE fiber showed that different matrices had an impact on displacement measurements. The PTFE fiber used in [1] had a diameter of 1000 µm (called "macro" fiber), the matrix used was the same as the one used in this work.

Figure 7.14 presents ε_x^l and ε_y^l with respect to the global applied strain for the PTFE / epoxy specimen presented in this work and the PTFE / epoxy specimen presented in Tabiai et al [1]. The virtual extensometers edges were situated about a subset away from the fiber's

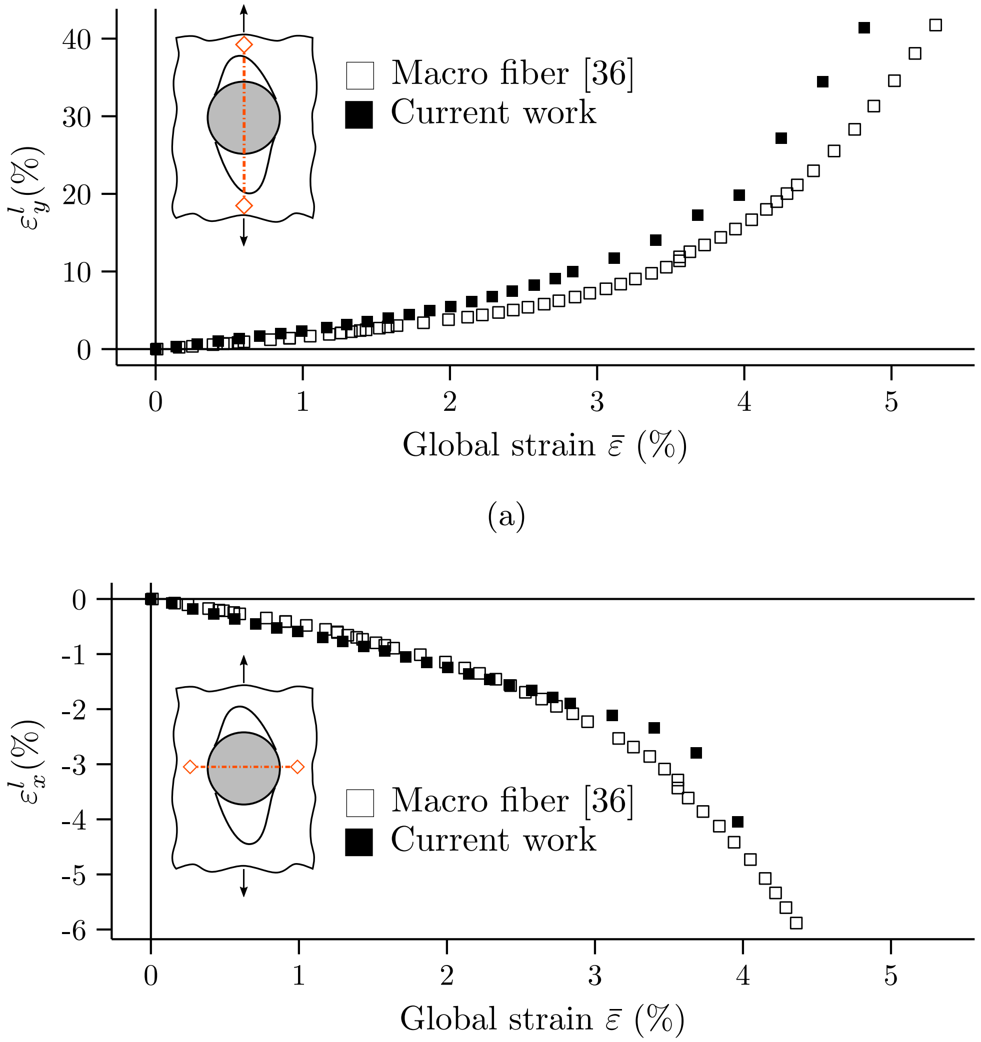

(a)

(b)

Figure 7.14 Comparison of ε_x^l and ε_y^l for a PTFE macro fiber of 1000 µm in diameter from [1] and results for the PTFE fiber (711 µm) used in this work (presented in Figure 7.7). Macro fiber results were obtained using a stereoscopic microscope equipped with two CCD cameras. DIC was carried out with VIC3D7 commercial software edge in each direction. The figure shows that both measurements are consistent and show the same behavior. Differences between ε_x^l and ε_y^l appear at global strains starting at 3 %. At this point, the inter-facial debonding crack is already significant and might have a larger impact on ε_x^l and ε_y^l, which might explain the small quantitative difference later on. Another possibility is that the placement of both virtual extensometers was not quite the same with respect to the fiber due to the subsets having different sizes in both works. The fiber size does not appear to significantly affect the inter-facial debonding crack growth.

7.6.4 Limitations of the study

Residual stresses inherent to the fabrication process must have developed for all FRC variants due to the different coefficient of thermal expansion (CTE) for fibers and matrix, as well as chemical shrinkage [5, 12]. These potential residual stresses were not measured during this work.

For each single fiber specimen tested, the out of plane inter-facial debonding is growing within the specimen around the fiber, along the z direction. This mechanism, called tunneling [130], is directly linked to the cracks visible at the free surface [9]. The opening of the 0° and 180° cracks visible for the PTFE / epoxy and PLA / epoxy specimens (Figures 7.3c and 7.4c) results from tunneling. Martyinuk et al. [9] showed that free surface visible crack growth might be linearly linked to tunneling growth. Tunneling growth depends on the fiber / matrix bonding strength as debonding must continue along the fiber. The optical setup used in this work could not allow direct observation of this mechanism.

Inter-facial debonding happens in plane and out of plane, simultaneously, for the CF / epoxy specimen as shown in Figure 7.12. Out of plane measurements, after inter-facial debonding initiation, present a clear discontinuity between isolated carbon fibers and matrix. It can also be seen that out of plane inter-facial debonding is particularly significant around the edges of the large CFs bundle where in plane inter-facial debonding is also the most significant. Out of plane inter-facial debonding is also present within the bundle's core but is less pronounced (inferior to 1 μm) than on the periphery. These results show that modeling this experiment should account for 3D effects as out of plane inter-facial debonding was present during all tests and is as pronounced as in plane inter-facial debonding. Height measurements for all specimens presented in this work, for each timestep, and a procedure to explore the dataset are provided in the additional package [131].

7.6.5 Experimental data availability

CSV files containing the displacement, height, strain, confidence $\mathcal{C}$ value for each pixel at each time-step, are made available as an additional dataset. The applied load and displacement for any image taken during the tests presented here is also made available. A “readme PDF” file clarifying the format in which the data is structured is also provided. The calibration parameters obtained after calibrating each test are also included with the additional dataset. The images used for the calibration process are also provided in the additional dataset, meaning that this information can, for example, be used to spatially calibrate another DIC software to analyze the data differently, using different parameters [131].

7.7 CONCLUSION

The purpose of this study was to provide accurate full experimental displacement fields measurements of interfacial debonding and damage initiation in a fiber or bundle’s vicinity with the goal of better understanding damage initiation and growth for fibers under transverse load. This work also provides out of plane measurements for fibers and a bundle of carbon fibers and connects the full displacement field measurements with out of plane displacements and measurements.

Fibre / matrix inter-facial debonding was observed using a LSCM for tree single-fiber and a bundle of carbon fibers composites under quasi-static transverse load. Measurements of the displacement and strain field in the reinforcement’s vicinity were obtained through DIC analysis. Three fiber materials were chosen to create composites of radically different bonding strengths.

Damage in single fiber composites initiated at the fiber / matrix interface where an out of plane displacement difference between the fiber and matrix was the highest and where ε_y was maximal (0° and 180°). The inter-facial debonding crack then grew around each single fiber. Inter-facial debonding was shown to grow faster around PTFE and PLA fibers, which have the weakest bonding. Out of plane inter-facial debonding is shown to play an important role in inter-facial debonding as the size of the out of plane inter-facial crack is larger than the in plane one for all specimens. Local measurements show that strong bonding for the HCS / epoxy specimen, prevents tangential debonding around the -90° and +90° interface areas, slowing down the inter-facial crack growth under Mode II. The bundle of CF showed how damage initiates and grows around a large bundle composed of about a hundred fibers and a small one containing only a few CF. Damage initiated at the edges of each bundle, which is also where ε_y was maximal (0° and 180°). Interfacial damage then grew around fibers on the edges without affecting the bundle's core. Out of plane interfacial debonding appears to be critical for single fibers, as the out of plane interfacial crack is larger than the in plane one. The larger bundle of CFs shows that carbon fibers concentration slows down out of plane interfacial crack growth. No visible in plane interfacial crack is visible at the bundle's core although less than 1 μm out of plane cracks were measured within the core. A quantitative comparison of the displacement and strain fields around single fibers and a bundle of fibers is also provided here and shows that a bundle of carbon fibers can be assumed to behave, in overall, like a single fiber.

μDIC is shown to be a promising technique in order to better quantitatively understand damage at the microscale. In addition, μDIC observation apparatus able to provide out of plane displacement values (stereoscopic DIC or LSCM) are shown to provide relevant information which cannot be obtained using an SEM or synchrotron observation apparatus. These simple cases can be used to calibrate inter-facial properties for simulation of a similar problem. Results also show that damage to a single-fiber composite is related to fiber debonding along the fiber and is thus a 3D problem. The CF specimen shows that out of plane displacement also plays an important role for a bundle of carbon fibers, as the inter-facial debonding happening on the outer edges of the bundle is also directly connected to areas where a strong out of plane displacement can be seen. Modeling of such a problem must be in 3D in order to consider all the problem's components.

Extensive results for each specimen presented here are available online as an additional package. These results can be used to provide a better understanding of damage initiation and growth in a FRC. The geometry of specimens and reinforcements along with their elastic properties are provided. These results can also be used to quantitatively benchmark micromechanical damage models.

CHAPTER 8 GENERAL DISCUSSION

The aim of this thesis was to provide quantitative full field measurements of UD FRCs under transverse load in order to benchmark damage models and better understand how damage initiates and propagates. The limitations of the experimental setups used, limitations related to out-of-plane measurements and missing considerations regarding used materials are discussed in this section.

8.1 Experimental limitations

8.1.1 Image acquisition

The first article of this thesis presents stereo images that were used for DIC analysis; experimental images were obtained using a stereo-microscope equipped with CCD cameras. Images obtained covered an area of about 6 mm × 7 mm with a resolution of 2.5 $^{\mu m}/_{px}$. The LSCM used to observe the bundle of CFs presented in the third article of this thesis provided images covering an area of 256 µm × 256 µm with a scale of 0.063 $^{\mu m}/_{px}$. This scale improvement enable to distinguish and measure inter-facial cracks around single CFs of 7.5 µm. However it is possible to see in Figures 7.10c and 7.11 that it is not possible to accurately observe the inter-facial crack's junction with the fiber because inter-facial cracks are at most 4 µm wide. A different observation setup ought to be used to more precisely study damage mechanisms in the vicinity of a single carbon fiber.

Another possible observation technique is a SEM, which is commonly used to observe FRCs [51, 59, 61]. In order to observe epoxy under a SEM, it will be necessary to coat the polymer with a conductive material [59]. This operation makes usage of the polymer's roughness as a speckle pattern much harder because the coating would eliminate the differences in surface reflectivity.

Single fiber inter-facial debonding for an Eglass / epoxy specimen has also been observed using a µCT as mentioned in Section 2.2.3 although µCT scans are still used to study damage in FRCs [132, 133]. This observation method would allow for a better resolution, however it has been reported to damage the free surface and is susceptible to modify the matrix behavior in the fiber vicinity [9]. A µCT observation setup would be ideal for observation of in plane and out of plane inter-facial debonding through the specimen as shown by Martyniuk et al [9], which was missing in this work.

8.1.2 Speckle pattern

Figures 7.3, 7.4 and 7.5 show that the tracking area lost around the single-fiber specimen during each test remains quite small (about 10 μm). However, for the single CF or small bundle of CFs, shown in Figures 7.10c and 7.11, the area over whicht racking is lost is significant with respect to a CF size. As explained in Section 6, the area over which tracking is lost is dependent of the speckle pattern average feature size and their spatial distribution [56]. In order to reduce the area over which tracking is lost, a finer speckle pattern would be required.

The most common method employed to make a speckle pattern for μDIC consists of having small amounts of sub-micron alumina particles mixed within dispersing agent, depositing the solution on a material and then letting it dry. Due to their different color under a SEM, these particles would ideally be visible as white dots homogeneously distributed on the material's surface [59]. This method creates aggregates in the final speckle pattern, and shows higher concentrations of particles at the edge of the fiber / matrix interface due to a slight difference in height of the matrix and fiber free surface (see section 8.2.2). Speckle patterns obtained using this method are also not homogeneous over areas larger than a few hundred square micrometers [61].

The speckle pattern can also be made using "scratches", as shown in the third article presented in this thesis (Section 7). Silicon carbide abrasive grinding paper was used in that work. Other methods that affect the roughness profile of a polymer could also be used to provide a speckle pattern for DIC. Surface etching consists in removing material from a sample's surface in order to create roughness. Surface etching is routinely used in the industry before applying adhesives on a material's surface in order to improve its surface energy by creating new surfaces. Etching can be performed on epoxies using specific acids [52] or using plasma treatment [136]. Figure 8.1a shows how a plasma jet can be used to etch a polymer's surface and create a roughness profile which can be used as a speckle pattern for DIC tracking. Figure 8.1b presents an example of an Epoxy / PSU copolymer chemically etched. The result is a roughness profile on the specimen's surface which could then be used as a speckle pattern for DIC tracking.

8.1.3 Out of plane measurements using the LSCM

In the first paper presented in this thesis (section 5), out of plane measurements were performed using the DIC software, which allowed a direct connection between each pixel and its out of plane displacement during the test. In the third paper (section 7), the LSCM is used to measure the out of plane profile of an area and capture micrographs. The DIC software used in that work is however not able to process the out of plane information provided by the LSCM. Because of this the results presented in the third paper are out of plane profile measurements and not displacements. Results cannot show how a specific material point behaved during the test. This limitation can be overcome by developing a method able to extract the out of plane information from the LSCM proprietary file format for a specific pixel on the micrograph.

8.2 Damage initiation

8.2.1 Residual stresses measurement

Residual stresses due to the fabrication process must have developed for all specimens presented in this work due to the different coefficient of thermal expansion (CTE) for fibers and matrix, as well as chemical shrinkage [5, 12]. Although the epoxy used cures at room temperature, it was possible to notice that the molds temperature increased during curing

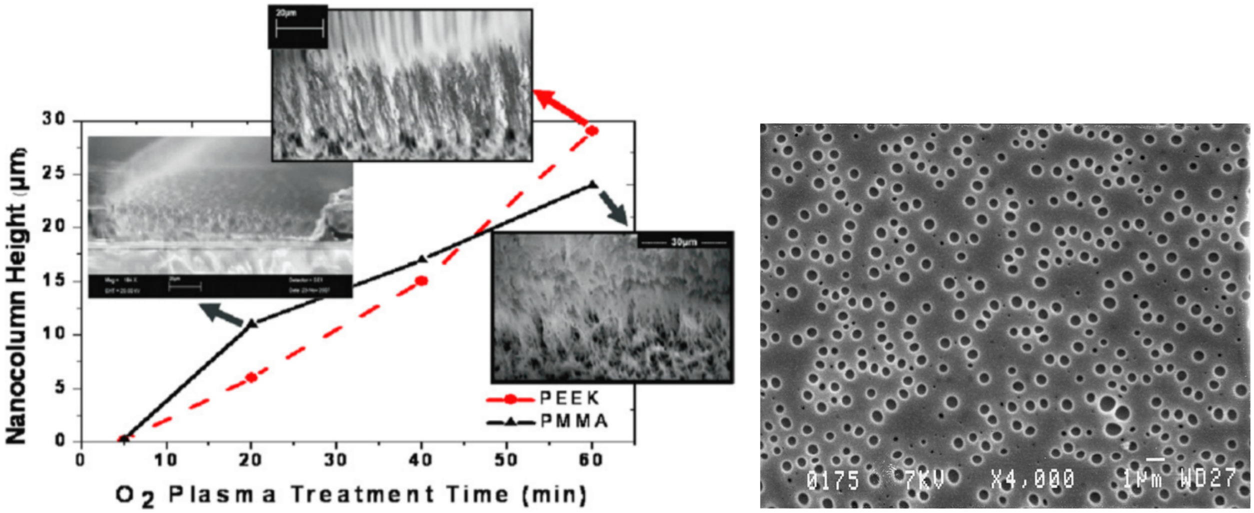

(a)

(b)

Figure 8.1 A plasma torch can be used to create a roughness profile on polymers. (a) shows a graph presenting the height of nanocolumns as a function of the oxygen jet plasma treatment time; results are presented for two polymers, PEEK and PMMA. SEM micrographs are provided, showing how the nanocolumn structure creates a roughness pattern on the surface which can then be used as a speckle pattern for DIC analysis [134]. (b) presents a SEM micrograph of an Epoxy / PSU copolymer (DGEBA epoxy-PACM 20 / PSU) etched at 100° C with methylene chloride. The micrograph shows how a fine speckle pattern can be obtained through chemical etching for a copolymer [135] due to the exothermic nature of epoxy polymerization. Qualitative photo-elastic observations of specimens before loading also revealed the presence of residual stresses around embedded fibers on the specimen's edge (due to resin-mold interaction). One of the goals of this work is to provide experimental results which could be used to benchmark simulation results. In order to quantitatively compare experimental full field measurements with simulation results, it might be necessary to also model residual stresses within the simulation.

In addition, thermal residual stresses might affect interfacial debonding. *Asp et al.* showed that residual stresses increase a UDFRC's transverse strength for high fiber concentrations and change the damage initiation site of the matrix cavitation damage mechanism when loaded in tension [137]. Although residual stresses might have affected the fiber/matrix interfacial debonding, these potential residual stresses were not measured during this thesis.

8.2.2 Interface initial state

Throughout this thesis, each specimen was implicitly considered as completely free of damage before a crack appeared during a test. A specimen was considered as damaged when a crack became visible. While investigating damage mechanisms in UD FRCs, Marshall et al. [138] showed that a crack might already be present within each interface before any load is even applied due to the difference in mechanical properties of the fiber and matrix (elastic mismatch). The residual stress in a matrix responsible for the initial inter-facial crack along

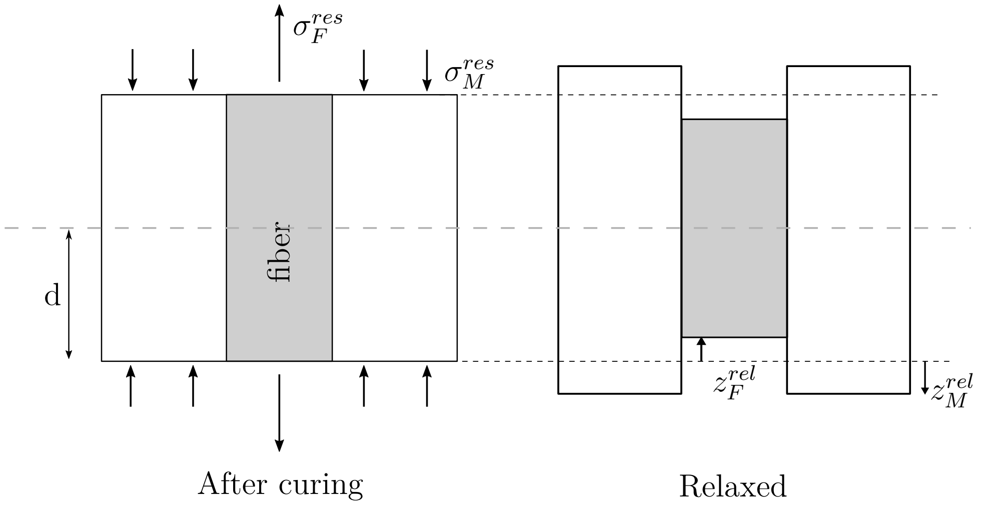

Figure 8.2 The cross-section of a single-fiber surrounded by matrix is schematically shown after curing and once it relaxed. After curing, the matrix is, in this case, under a compressive residual stress, σ_M^{res}, while the fiber is under a tensile one, σ_F^{res}. In order to relax residual stresses, the matrix and fiber should slide one into another by a distance z_M^{rel} and z_F^{rel}

the fiber can be theoretically computed. Let us consider a composite for which the matrix shrinks while the fiber expands. After curing, the matrix is under a compressive stress $-\sigma_M^{res}$, while the fibers are under a stress σ_F^{res}, as shown in Figure 8.2.

The displacements z_F^{rel} and z_M^{rel} necessary to relax those stresses on the fiber and matrix sections can be seen in Figure 8.2. These displacements can be written as $2z_F^{rel} = 2(\frac{\sigma_F^{res}}{E_F})d$ to measure the displacement necessary for the fiber to relax and $2z_M^{rel} = 2(\frac{\sigma_M^{res}}{E_M})d$ for the matrix, where d is the half-thickness of the composite.

Thus, in all tests performed in this thesis, a small difference between the matrix and fiber initial height should be present before even starting the test. For specimens used in the first paper, it was not possible to measure any distinguishable out-of-plane difference between matrix and fiber. A layer of paint was used as a speckle pattern for those specimen and could be the reason why no difference appear between the height of the fiber and matrix. In the third paper, it was not possible to get out of plane measurement results for the PTFE and HCS fiber due to high reflectivity of these two materials. It was however possible to obtain out of plane measurements for the PLA / epoxy specimen.

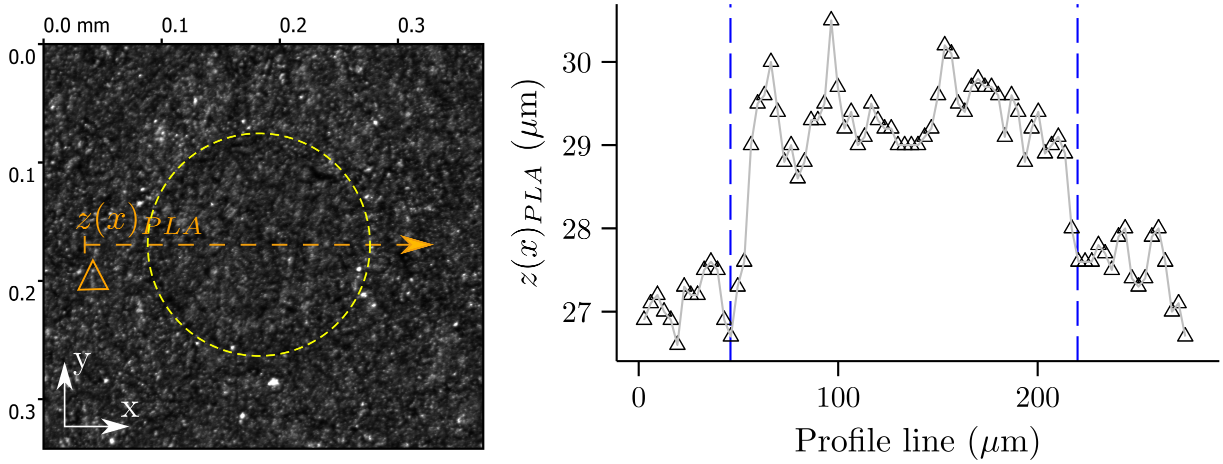

(a)

(b)

Figure 8.3 (a) shows the initial micrograph (unloaded) of the PLA / epoxy specimen. A yellow circle shows the approximative position of the PLA fiber. (b) presents a plot of $z(x)_{PLA}$, the height of each material point along the orange line drawn in (a). The approximative position of the fiber is shown with two blue dashed lines. It is possible to see that out-of-plane measurements for the fiber are higher than the matrix

Figure 8.3 presents out-of-plane measurements for the first time step of the PLA / epoxy test. The specimen was not loaded yet. It is possible to see that the PLA fiber was protruding out of the matrix, ≈2 µm above the matrix. Since the specimen was mirror polished before putting under the LSCM, this protrusion is assumed to happen after polishing, due to the relaxation of residual stresses at the free surface, as shown in Figure 8.2. This observation would mean that for all tests presented in this thesis an initial crack was already present at the fiber / matrix interface at each free surface.

8.3 Matrix viscoelasticity

The pure epoxy used in this thesis was presented as an elastic material. Elastic mechanical properties only were provided in the first and third papers presented in this work (Sections 5 and 7). However, epoxies are known to have a viscoelastic behavior. In the experimental setup presented in the first paper, the test had to be paused in order to move the mechanical stage holding the stereo-microscope and track the fiber. In the case of the LSCM presented in the third paper, it was necessary to pause the test in oder to capture an image due to the time taken by scanning. During these pauses, it was possible to see the load applied on the specimen quickly drop during the first few seconds and then keeping to drop slower.

In order to properly model its viscoelastic behavior, creep tests were performed at a constant stress level of 11.5 MPa [123]. The specimen was loaded at a rate of 500 $^N/_s$ until the desired force was reached. The force was then maintained for a duration of 30 minutes and the specimen is then unloaded at a speed of -500$^N/_s$. DIC was used during the test to measure the specimen's longitudinal and transverse strain fields. The creep test data was input in the ABAQUS FEA commercial package using the `VISCOELASTIC, TIME=CREEP TEST DATA` to extract the appropriate constitutive Prony serie parameters and relaxation times through non-linear least square optimization. The normalized shear and bulk modulus with their respective relaxation times are provided in Table 8.1.

In order to validate the properties obtained, a specimen similar to the one used to mea-

Table 8.1 Prony series parameters obtained through non-linear least square fit based on creep test data at 11.5MPa. This fitting procedure was automatically done by ABAQUS

Material	Relaxation time (s)	Normalized Shear Modulus (-)	Relaxation time (s)	Normalized Bulk Modulus (-)
Epoxy	7.44	9.52×10^{-2}	0.14	6.89×10^{-3}
	89.67	7.57×10^{-2}	12.62	1.04×10^{-1}
	1154.00	1.79×10^{-1}	6170.00	3.68×10^{-1}

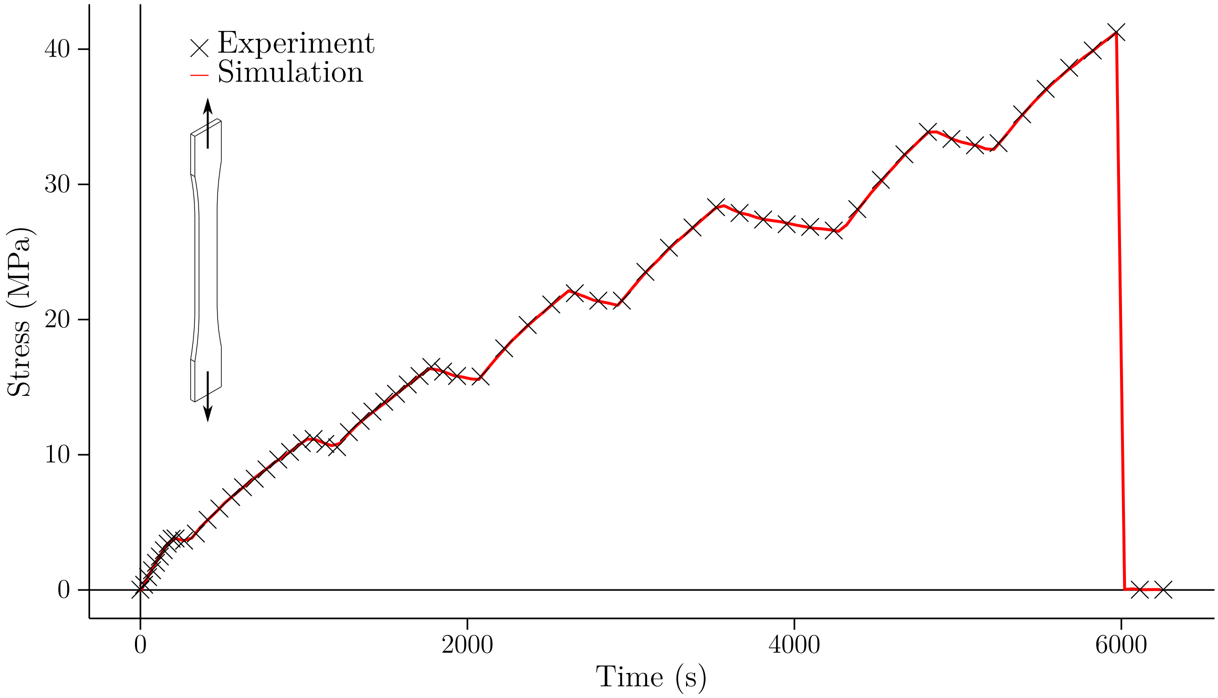

Figure 8.4 A standard tensile test pulled in displacement (at a speed $v_1 = 0.05$ $^{\mathrm{mm}}/_{\mathrm{min}}$) test was performed on a plain dogbone specimen made of the studied matrix epoxy. The test was arbitrarily paused (the machine's crosshead was blocked) for a random amount of time several times during the test. Black crosses show the stress levels recorded by the electromechanical testing machine's load cell during the test. The red line presents the stress levels measured in a simulation of the same experimental setup for a specimen pulled in displacement at speed v_1

sure the viscoelastic properties was loaded in tension. The test was paused for arbitrary lengths of time at random moments, similarly to pauses during the single-fiber tests. During pauses, the stress measured by the tensile testing machine dropped down while the applied displacement remained constant. When pulled, the specimen was loaded in displacement at a rate of 0.05 $^{\mathrm{mm}}/_{\mathrm{min}}$. The same experiment was then done as a simulation using the same specimen geometry. The displacement applied by the tensile testing machine was applied as a boundary condition in the simulation. The stress within the strain gage of the simulation specimen is then compared with the stress from the experiment. Figure 8.4 presents both the experimental and simulation stresses in order to validate the viscoelastic properties measured. Both the simulation and experiment concord, thus the properties presented in Table 8.1 are valid. These viscoelastic properties should thus be used if the epoxy material is modeled.

CHAPTER 9 CONCLUSION AND RECOMMENDATIONS

This thesis presents the experimental investigation of damage initiation and growth of FRCs under transverse loading at the fiber level, the in plane and out of plane full field measurements for different single fiber composites and for a bundle of carbon fibers. The main goal is to provide a better understanding of how weak and strong fiber / matrix interfaces impact damage initiation and growth, and to provide quantitative benchmark results for micro mechanical damage models.

The impact of weak and strong inter-facial bonding on the 3D displacement fields, in plane strain field and crack growth was experimentally studied. Four different single fiber specimens were manufactured. The fibers used were ≈ 200 times larger than fibers used in commercial carbon fibers / epoxy composites. Two different epoxies were used as matrices and two different fibers, one having strong bonding with epoxies and the other a weak to no bonding with epoxies were used as materials. Each specimen was then tested, the fiber was disposed in the transverse direction with respect to the applied load. Stereoscopic digital image correlation was used to investigate displacement fields. Specimens were observed in and out of plane, and SDIC was used for displacement and strain full field measurements. Full strain fields results show correlations between the fiber / matrix bonding strengths and their respective full field measurements and damage features growth. In addition, the study shows how out of plane displacements plays an important role in cracks' initiation and growth. Our study showed that damage occurs in three different steps:

1. Damage initiated at the fiber / matrix interface at the location where an out of plane displacement difference between the fiber and matrix was the highest and where ε_y was maximal (0^o and 180^o);
2. Debonding crack growth on the transverse areas at the 45^o, -45^o, 135^o and -135^o angles around the fiber;
3. (a) PTFE: specimen failure caused by crack kinking in the matrix at the 90^o and -90^o areas, where the fiber was horizontally compressed and heavy out-of-plane striction was experienced in the case of PTFE specimens; or in the case of galvanized steel specimens
   (b) Galvanized steel: specimen failure caused by crack kinking in the matrix at the 45^o, -45^o, 135^o or -135^o angles

Damage features such as inter-facial cracks and matrix cracks were further investigated. DIC provides quantitative displacement field results, but does not directly provide quantitative information about damage features. A method using image processing techniques and DIC results was developed to autonomously extract crack pixels and identify them. The method developed provides crack area measurements for each image analyzed with DIC, the exact crack path on the reference image and the global strain or stress value at which a pixel becomes part of the crack. These results were applied to the single-fiber specimens presented above. The crack area growth showed that damage initiates at about the same strain applied on the specimen but that it grew faster for specimens with weak inter-facial bonding. The final crack path in the reference coordinate showed that the final damage mechanism for weak and strong bonding specimens is different. The crack path for the weakly bonded specimen is almost perpendicular to the applied force and symmetrical with respect to the fiber, while it is shifted for a strongly bonded specimen.

An experimental setup using a laser scanning confocal microscope was also used to obtain similar measurements for new fiber materials about 20 times larger than fibers from commercial carbon fibers / epoxy composites. Fibers with no bonding, weak bonding and strong bonding with epoxy were tested. Single fiber composites validated results previously observed with larger fibers. A specimen was also manufactured with a bundle of commercial carbon fibers instead of a single fiber. The bundle was observed at different magnifications during the test over different areas, in order to observe the whole bundle, a smaller isolated bundle and a single carbon fiber. In plane displacement and strain fields in addition to out of plane measurements were obtained for each magnification and provided quantitative measurements while damage was growing. Out of plane measurements showed that large interfacial cracks grow along the fiber and accelerate propagation of in plane cracks. The full strain and displacement fields showed that crack initiation might be caused by an initial out of plane mismatch present in all FRCs.

All the experimental results and subroutines used for this thesis were packaged and uploaded to reliable data repositories. Each package was prepared to ensure that a fellow researcher will be able to understand and use them. Each data package can be used to benchmark predictions for a micro mechanical damage model, analyze the results in order to better understand how damage initiates and grows and obtain the exact mode mixity or displacement-traction laws around a growing crack for cohesive elements' design.

Recommendations for future studies

- **Develop a method to manufacture a consistent speckle pattern for SEM observations**

  At magnifications higher than the one used for the LSCM, optical artifacts started appearing on micrographs. These artifacts make the recognition of subsets through DIC impossible for one image to the next. Displacement measurements with a higher accuracy than the one presented in this work would require a SEM with a microtensile testing machine located in its chamber.

- **Damage growth in small bundle of large fibers to study crack propagation within a bundle**
  Using the same methodology as the one presented in the first paper of this thesis, it is possible to manufacture a specimen containing a small bundle of about six fibers. By changing the shape of the hooks at the bottom of the mold, it would be possible to specify the arrangement and distances between these large fibers. It would be possible to observe and measure in and out-of-plane displacement fields for such a bundle. Specimens with bundles of fibers having different bonding strengths with epoxy could be used. Several parameters and their impact on damage could be studied such as arrangements of fibers, distances between fibers or inter-facial bonding strength. Full strain and displacement field results (in and out-of-plane) would help better understand crack propagation within a bundle. They could also be used to benchmark simulation results.

- **Accurate out of plane measurements for unloaded specimen**
  Section 8.2.2 shows that there is an initial difference in height between the PLA fiber height and epoxy matrix, this difference in height is a function of the material's Young modulus. Such a difference might be more noticeable in the case of larger fiber, such as the ones used in the first paper presented in this thesis. Measurements of this difference for fibers with different Young's modulus could show these differences in height. These results could lead to a better understanding of observable crack initiation.

- **Global extended digital image correlation**
  DIC analysis presented in this work were done using commercial local DIC softwares. Recently, global DIC has been extended by Besnard et al. [105] using concepts from the X-FEM method. The method might be able to improve DIC results by extending the tracked area around discontinuities (cracks). Global DIC has not been implemented in commercial or open source DIC software and would require extensive work to maintain the same spatial resolution and out of plane displacement measurements. This work would not require additional experiments as the complete experimental results from this work are available. The data package provided with the first and third publications presented in this work can be used to perform a global DIC analysis.

- **Volumetric DIC**
  A μCT can be used to observe a single fiber composite and provide cross-sections of the specimen that can be used to recreate a 3D virtual model of the specimen. Metallic submicron particles could be distributed within the matrix and would be distinguishable from the matrix in the μCT 3D virtual model. An in-situ test observed with a μCT could thus be used to measure volumetric full field displacements in the fiber's vicinity during tunneling and provide data which could validate assumptions about the connections between out of plane and in plane crack growth.

- **Residual stress estimation**
  Residual stress measurements for polymers can be challenging. In addition, residual stress measurement methods (e.g. layer removal, hold drilling or chemical probe technique) allow measurements over volumes larger than the fiber. Residual stresses can also be estimated by measuring temperatures in different areas of the mold during room or oven curing. The final residual stress state of the specimen can then be estimated using FEM simulations.

- **Fatigue in-situ testing**
  While working on this thesis, a preliminary qualitative fatigue test was done using a specimen similar to the ones used in the first paper of this thesis. It was possible to measure displacements and strains during the fatigue test and after it was done. An inter-facial crack appeared and grew around the fiber before growing in the matrix and provoking specimen failure.

REFERENCES

[1] I. Tabiai, R. Delorme, D. Therriault et M. Levesque, “In-situ Full Field Measurements During Inter-Facial Debonding in Single Fiber Composite Under Transverse Load,” *Experimental Mechanics*, oct. 2018. [En ligne]. Disponible: http://link.springer.com/10.1007/s11340-018-0429-9

[2] Dr. Faye Smith, “The use of composites in aerospace: Past, present and future challenges,” janv. 2013. [En ligne]. Disponible: https://avaloncsl.files.wordpress.com/2013/01/avalon-the-use-of-composites-in-aerospace-s.pdf

[3] Peter B. Ladkin, “The Crash of AA587: A Guide,” nov. 2004. [En ligne]. Disponible: http://www.leonardo-in-flight.nl/PDF/Airbus%20Crash%20of%20AA587%20due%20inappropriate%20use%20of%20rudder.pdf

[4] R. Talreja et C. Veer Singh, *Damage and Failure of Composite Materials*, cambridge university press éd. Cambridge University Press, 2012.

[5] P. P. Parlevliet, H. E. N. Bersee et A. Beukers, “Residual stresses in thermoplastic composites—A study of the literature—Part I: Formation of residual stresses,” *Composites Part A: Applied Science and Manufacturing*, vol. 37, n°. 11, p. 1847–1857, nov. 2006. [En ligne]. Disponible: http://www.sciencedirect.com/science/article/pii/S1359835X06000145

[6] Xavier Martinez, “Micro-mechanical simulation of composite materials using the Serial/Parallel mixing theory,” Thèse de doctorat, Polytechnique university of Catalunya, Barcelona, juin 2008. [En ligne]. Disponible: https://web.cimne.upc.edu/users/xmartinez/Public/Publications/PhD/PhD%20-%20Xavier%20Martinez.pdf

[7] A. Gherissi, F. Abbassia et A. Zghal, “A Comparative Study of Three Different Microscale Approaches for Modeling Woven Composite Material,” *Journal of Material Sciences & Engineering*, p. 1–7, déc. 2016.

[8] H. Kikuchi, K. Mukoyama et S. Takuya, “An estimation of failure envelope for FRP using oblique unit model,” 2015.

[9] K. Martyniuk, F. Sørensen, P. Modregger et E. M. Lauridsen, “3d in situ observations of glass fibre/matrix interfacial debonding,” *Composites Part A: Applied Science and Manufacturing*, vol. 55, p. 63–73, déc. 2013.

[10] R. B. PRIME, “CHAPTER 5 - Thermosets,” dans *Thermal Characterization of Polymeric Materials*, E. A. TURI, édit. Academic Press, 1981, p. 435–569. [En ligne]. Disponible: http://www.sciencedirect.com/science/article/pii/B9780127037806500109

[11] S. W. Goodman, *Handbook of Thermoset Plastics, 2nd Ed.* Cambridge University Press, déc. 1999.

[12] C. González et J. LLorca, “Mechanical behavior of unidirectional fiber-reinforced polymers under transverse compression: Microscopic mechanisms and modeling,” *Composites Science and Technology*, vol. 67, n°. 13, p. 2795–2806, oct. 2007. [En ligne]. Disponible: http://linkinghub.elsevier.com/retrieve/pii/S0266353807000711

[13] M. Abouhamzeh, J. Sinke, K. M. B. Jansen et R. Benedictus, “closed form expression for residual stresses and warpage during cure of composite laminates,” *Composite Structures*, 2016. [En ligne]. Disponible: http://www.sciencedirect.com/science/article/pii/S0263822315006443

[14] J. Jakobsen, M. Jensen et J. H. Andreasen, “Thermo-mechanical characterisation of in-plane properties for CSM E-glass epoxy polymer composite materials – Part 1: Thermal and chemical strain,” *Polymer Testing*, vol. 32, n°. 8, p. 1350–1357, déc. 2013. [En ligne]. Disponible: http://www.sciencedirect.com/science/article/pii/S0142941813001682

[15] D. Vasiukov, S. Panier et A. Hachemi, “Direct method for life prediction of fibre reinforced polymer composites based on kinematic of damage potential,” vol. 70, p. 289–296. [En ligne]. Disponible: http://www.sciencedirect.com/science/article/pii/S0142112314002552

[16] T. Jollivet, C. Peyrac et F. Lefebvre, “Damage of composite materials,” vol. 66, p. 746–758. [En ligne]. Disponible: http://www.sciencedirect.com/science/article/pii/S1877705813019619

[17] C. Ageorges, K. Friedrich, T. Schüller et B. Lauke, “Single-fibre Broutman test: fibre–matrix interface transverse debonding,” *Composites Part A: Applied Science and Manufacturing*, vol. 30, n°. 12, p. 1423–1434, déc. 1999. [En ligne]. Disponible: http://www.sciencedirect.com/science/article/pii/S1359835X99000457

[18] N. J. Pagano, “On the micromechanical failure modes in a class of ideal brittle matrix composites. Part 1. Coated-fiber composites,” *Composites Part B: Engineering*, vol. 29, n°. 2, p. 93–119, 1998. [En ligne]. Disponible: http://www.sciencedirect.com/science/article/pii/S1359836897000024

[19] M. Romanowicz, “Progressive failure analysis of unidirectional fiber-reinforced polymers with inhomogeneous interphase and randomly distributed fibers under transverse tensile loading,” vol. 41, n°. 12, p. 1829–1838. [En ligne]. Disponible: http://www.sciencedirect.com/science/article/pii/S1359835X10002496

[20] Z. Hashin, “Analysis of damage in composite materials,” dans *Yielding, Damage, and Failure of Anisotropic Solids*, egf publication éd. J. P. Boehler, 1987, vol. 5. [En ligne]. Disponible: http://www.wiley.com/WileyCDA/WileyTitle/productCd-0852987358.html

[21] C. J. Spragg et L. T. Drzal, *Fiber, Matrix, and Interface Properties.* ASTM International.

[22] L. Hart-Smith, “Application of the strain invariant failure theory (SIFT) to metals and fiber–polymer composites,” vol. 90, n°. 31, p. 4263–4331, 2010. [En ligne]. Disponible: http://www.tandfonline.com/doi/abs/10.1080/14786435.2010.510450

[23] S. Zhandarov et E. Mäder, “Characterization of fiber/matrix interface strength: applicability of different tests, approaches and parameters,” *Composites Science and Technology*, vol. 65, n°. 1, p. 149–160, janv. 2005. [En ligne]. Disponible: http://www.sciencedirect.com/science/article/pii/S026635380400171X

[24] B. K. Larson et L. T. Drzal, “Glass fibre sizing/matrix interphase formation in liquid composite moulding: effects on fibre/matrix adhesion and mechanical properties,” vol. 25, n°. 7, p. 711–721, 1994. [En ligne]. Disponible: http://www.sciencedirect.com/science/article/pii/0010436194902062

[25] B. F. Sørensen, K. Jørgensen, T. K. Jacobsen et R. C. Østergaard, “DCB-specimen loaded with uneven bending moments,” vol. 141, n°. 1, p. 163–176, 2006. [En ligne]. Disponible: http://link.springer.com/article/10.1007/s10704-006-0071-x

[26] B. F. Sørensen et S. Goutianos, “Mixed Mode cohesive law with interface dilatation,” *Mechanics of Materials*, vol. 70, p. 76–93, mars 2014.

[27] J. Koyanagi, P. D. Shah, S. Kimura, S. K. Ha et H. Kawada, “Mixed-Mode Interfacial Debonding Simulation in Single-Fiber Composite under a Transverse Load,” *Journal of Solid Mechanics and Materials Engineering*, vol. 3, n°. 5, p. 796–806, 2009.

[28] J.A. Nairn, R. Talreja, J.A.E. Manson, “Matrix Microcracking in Composites,” dans *Polymer Matrix Composites*, ser. Comprehensive Composite Materials. Elsevier Science, 2000, n°. 2, p. 403–32.

[29] M. Hinton, “Predicting failure in composite laminates: the background to the exercise,” *Composites Science and Technology*, vol. 58, nº. 7, p. 1001–1010, juill. 1998. [En ligne]. Disponible: http://linkinghub.elsevier.com/retrieve/pii/S0266353898000748

[30] P. J. Herrera-Franco et L. T. Drzal, “Comparison of methods for the measurement of fibre/matrix adhesion in composites,” vol. 23, nº. 1, p. 2–27, 1992. [En ligne]. Disponible: http://www.sciencedirect.com/science/article/pii/001043619290282Y

[31] J. D. Schaefer, M. E. Guzman, C.-S. Lim, A. J. Rodriguez et B. Minaie, “Influence of functionalized carbon nanofibers on the single carbon fiber–epoxy matrix interface,” vol. 55, p. 41–47, 2013. [En ligne]. Disponible: http://www.sciencedirect.com/science/article/pii/S1359836813003077

[32] S. F. Zhandarov et E. V. Pisanova, “The local bond strength and its determination by fragmentation and pull-out tests,” vol. 57, nº. 8, p. 957–964, 1997. [En ligne]. Disponible: http://www.sciencedirect.com/science/article/pii/S0266353897000377

[33] R. J. Kerans et T. A. Parthasarathy, “Theoretical analysis of the fiber pullout and pushout tests,” vol. 74, nº. 7, p. 1585–1596, 1991. [En ligne]. Disponible: http://onlinelibrary.wiley.com/doi/10.1111/j.1151-2916.1991.tb07144.x/abstract

[34] M. C. Watson et T. W. Clyne, “The tensioned push-out test for fibre-matrix interface characterisation under mixed mode loading,” vol. 160, nº. 1, p. 1–5, 1993. [En ligne]. Disponible: http://www.sciencedirect.com/science/article/pii/092150939390491V

[35] P. F. M. Meurs, B. A. G. Schrauwen, P. J. G. Schreurs et T. Peijs, “Determination of the interfacial normal strength using single fibre model composites,” *Composites Part A: Applied Science and Manufacturing*, vol. 29, nº. 9–10, p. 1027–1034, 1998. [En ligne]. Disponible: http://www.sciencedirect.com/science/article/pii/S1359835X97001309

[36] M. R. Piggott, “Why interface testing by single-fibre methods can be misleading,” *Composites Science and Technology*, vol. 57, nº. 8, p. 965–974, 1997. [En ligne]. Disponible: http://www.sciencedirect.com/science/article/pii/S0266353897000365

[37] M.J. Rich, L.T. Drzal, Donald L. Hunston, Gale A. Holmes et Walter G. McDonough, “Round robin assessment of the single fiber fragmentation test,” p. 10 pp., 2002. [En ligne]. Disponible: http://www.nist.gov/manuscript-publication-search.cfm?pub_id=860441

[38] K. W. Stefanie Feih, “Testing procedure for the single fiber fragmentation test,” 2004.

[39] L. Yang et J. L. Thomason, “Interface strength in glass fibre–polypropylene measured using the fibre pull-out and microbond methods,” *Composites Part A: Applied Science and Manufacturing*, vol. 41, n^o. 9, p. 1077–1083, sept. 2010. [En ligne]. Disponible: http://www.sciencedirect.com/science/article/pii/S1359835X09003157

[40] J. F. Mandell, J. H. Chen et F. J. McGarry, “A microdebonding test for in situ assessment of fibre/matrix bond strength in composite materials,” *International Journal of Adhesion and Adhesives*, vol. 1, n^o. 1, p. 40–44, juill. 1980. [En ligne]. Disponible: http://www.sciencedirect.com/science/article/pii/0143749680900330

[41] A. Perrier, F. Touchard, L. Chocinski-Arnault et D. Mellier, “Mechanical behaviour analysis of the interface in single hemp yarn composites: DIC measurements and FEM calculations,” *Polymer Testing*, vol. 52, p. 1–8, juill. 2016. [En ligne]. Disponible: http://www.sciencedirect.com/science/article/pii/S0142941816301246

[42] J. Koyanagi, H. Nakatani et S. Ogihara, “Comparison of glass–epoxy interface strengths examined by cruciform specimen and single-fiber pull-out tests under combined stress state,” *Composites Part A: Applied Science and Manufacturing*, vol. 43, n^o. 11, p. 1819–1827, nov. 2012. [En ligne]. Disponible: http://www.sciencedirect.com/science/article/pii/S1359835X12001911

[43] J. P. McCrory, S. K. Al-Jumaili, D. Crivelli, M. R. Pearson, M. J. Eaton, C. A. Featherston, M. Guagliano, K. M. Holford et R. Pullin, “Damage classification in carbon fibre composites using acoustic emission: A comparison of three techniques,” vol. 68, p. 424–430, 2015. [En ligne]. Disponible: http://www.sciencedirect.com/science/article/pii/S1359836814003849

[44] R. B. Toumi, J. Renard, M. Monin et P. Nimdum, “Fatigue damage modelling of continuous e-glass fibre/epoxy composite,” vol. 66, p. 723–736, 2013. [En ligne]. Disponible: http://www.sciencedirect.com/science/article/pii/S1877705813019590

[45] J. Blom, J. Wastiels et D. G. Aggelis, “Application of acoustic emission on the characterization of fracture in textile reinforced cement laminates,” vol. 2014, p. e178020, 2014. [En ligne]. Disponible: http://www.hindawi.com/journals/tswj/2014/178020/abs/

[46] J.-M. Park, J.-W. Kim et D.-J. Yoon, “Comparison of interfacial properties of electrodeposited single carbon fiber/epoxy composites using tensile and compressive fragmentation tests and acoustic emission,” vol. 247, n^o. 1, p. 231–245, 2002.

[47] S. R. Stock, *MicroComputed Tomography: Methodology and Applications.* CRC Press, 2008.

[48] M. Yasaee, J. K. Lander, G. Allegri et S. R. Hallett, "Experimental characterisation of mixed mode traction-displacement relationships for a single carbon composite z-pin." [En ligne]. Disponible: http://www.sciencedirect.com/science/article/pii/S0266353814000372

[49] Y. Abdin, S. V. Lomov, A. Jain, G. H. van Lenthe et I. Verpoest, "Geometrical characterization and micro-structural modeling of short steel fiber composites," vol. 67, p. 171–180. [En ligne]. Disponible: http://www.sciencedirect.com/science/article/pii/S1359835X14002589

[50] M. Rask, B. Madsen, B. F. Sørensen, J. L. Fife, K. Martyniuk et E. M. Lauridsen, "In situ observations of microscale damage evolution in unidirectional natural fibre composites," vol. 43, n°. 10, p. 1639–1649. [En ligne]. Disponible: http://www.sciencedirect.com/science/article/pii/S1359835X12000656

[51] P. Wright, A. Moffat, I. Sinclair et S. M. Spearing, "High resolution tomographic imaging and modelling of notch tip damage in a laminated composite," *Composites Science and Technology*, vol. 70, n°. 10, p. 1444–1452, sept. 2010. [En ligne]. Disponible: http://www.sciencedirect.com/science/article/pii/S0266353810001417

[52] W.W. Adams, V.B. Gupta et L.T. Drzal, "An electron microscopic study of the morphology of cured epoxy resin," Systems Research Laboratories, Systems Research Laboratories, Dayton, OH 45440, Rapport technique AWAL-TR-86-4029, déc. 1986. [En ligne]. Disponible: http://www.dtic.mil/dtic/tr/fulltext/u2/a177995.pdf

[53] Benjamin Ttize, "Techniques to prevent sample surface charging and reduce beam damage effects for SEBM imaging," Thèse de doctorat, Ruperto Carola University of Heidelberg, Göttingen, Germany, juill. 2013. [En ligne]. Disponible: http://archiv.ub.uni-heidelberg.de/volltextserver/15372/1/Dissertation_Titze_2013.pdf

[54] M. Stamborska, J. Lapin, O. Bajana et M. Losertová, "Tensile deformation behaviour of ferritic-pearlitic steel studied by digital image correlation method," *Metallic Materials*, vol. 53, n°. 06, p. 399–407, 2016.

[55] B. Pan, D. Wu et Y. Xia, "High-temperature deformation field measurement by combining transient aerodynamic heating simulation system and reliability-guided digital image correlation," *Optics and Lasers in Engineering*, vol. 48, n°. 9, p.

841–848, sept. 2010. [En ligne]. Disponible: http://linkinghub.elsevier.com/retrieve/pii/S0143816610000916

[56] M. A. Sutton, J.-J. Orteu et H. W. Schreier, *Image correlation for shape, motion and deformation measurements: basic concepts, theory and applications.* New York, N.Y: Springer, 2009.

[57] B. Wang et B. Pan, “Subset-based local vs. finite element-based global digital image correlation: A comparison study,” *Theoretical and Applied Mechanics Letters*, vol. 6, n°. 5, p. 200–208, sept. 2016. [En ligne]. Disponible: http://linkinghub.elsevier.com/retrieve/pii/S2095034916300411

[58] F. Mortazavi, M. Lévesque et I. Villemure, “Image-based Continuous Displacement Measurements Using an Improved Spectral Approach,” *Strain*, vol. 49, n°. 3, p. 233–248, juin 2013.

[59] M. Mehdikhani, M. Aravand, B. Sabuncuoglu, M. G. Callens, S. V. Lomov et L. Gorbatikh, “Full-field strain measurements at the micro-scale in fiber-reinforced composites using digital image correlation,” *Composite Structures*, vol. 140, p. 192–201, avr. 2016.

[60] S. Correlated, *Vic-3D Help Manual*, ser. Correlated Solutions, 2010. [En ligne]. Disponible: http://www.correlatedsolutions.com/installs/Vic-3D-2010-manual.pdf

[61] L. Canal, C. González, J. Molina-Aldareguía, J. Segurado et J. LLorca, “Application of digital image correlation at the microscale in fiber-reinforced composites,” *Composites Part A: Applied Science and Manufacturing*, vol. 43, n°. 10, p. 1630–1638, oct. 2012. [En ligne]. Disponible: http://linkinghub.elsevier.com/retrieve/pii/S1359835X1100220X

[62] S. A. Silling et R. B. Lehoucq, “Peridynamic Theory of Solid Mechanics,” dans *Advances in Applied Mechanics*, ser. Advances in Applied Mechanics, H. A. a. E. v. d. Giessen, édit. Elsevier, 2010, vol. 44, p. 73–168. [En ligne]. Disponible: http://www.sciencedirect.com/science/article/pii/S0065215610440028

[63] S. Ramdoum, H. Fekirini, F. Bouafia, S. Benbarek, B. Serier et L. Feo, “Carbone/epoxy interface debond growth using the Contour Integral/Cohesive zone method,” *Composites Part B: Engineering*, vol. 142, p. 102–107, juin 2018. [En ligne]. Disponible: http://www.sciencedirect.com/science/article/pii/S1359836817341252

[64] M. J. Hinton, A. S. Kaddour et P. D. Soden, “Chapter 1.1 - The world-wide failure exercise: Its origin, concept and content,” dans *Failure Criteria in*

Fibre-Reinforced-Polymer Composites, M. J. Hinton, A. S. Kaddour et P. D. Soden, édit. Oxford: Elsevier, janv. 2004, p. 2–28. [En ligne]. Disponible: http://www.sciencedirect.com/science/article/pii/B9780080444758500020

[65] A. Kaddour et M. Hinton, “Maturity of 3d failure criteria for fibre-reinforced composites: Comparison between theories and experiments: Part B of WWFE-II , Maturity of 3d failure criteria for fibre-reinforced composites: Comparison between theories and experiments: Part B of WWFE-II,” *Journal of Composite Materials*, vol. 47, n°. 6-7, p. 925–966, mars 2013.

[66] R. M. Christensen, “The World Wide Failure Exercise II Examination of Results - FailureCriteria.com,” 2014. [En ligne]. Disponible: http://www.failurecriteria.com/theworldwidefail.html

[67] “Matweb - zeus PTFE Tubing,” 2014. [En ligne]. Disponible: http://www.matweb.com/search/datasheet.aspx?matguid=813c4ba4827a4e2580fd58a4df1f2a13&ckck=1

[68] J. Shao et J. Rudnicki, “A microcrack-based continuous damage model for brittle geomaterials,” vol. 32, n°. 10, p. 607–619. [En ligne]. Disponible: http://linkinghub.elsevier.com/retrieve/pii/S0167663600000247

[69] S. Nemat-Nasser et M. Obata, “A microcrack model of dilatancy in brittle materials,” vol. 55, n°. 1, p. 24–35. [En ligne]. Disponible: http://dx.doi.org/10.1115/1.3173647

[70] P. J. Lemaitre, “Phenomenological aspects of damage,” dans *A Course on Damage Mechanics.* Springer Berlin Heidelberg, p. 1–37. [En ligne]. Disponible: http://link.springer.com/chapter/10.1007/978-3-642-18255-6_1

[71] F. J. Vernerey et M. Kabiri, “Adaptive Concurrent Multiscale Model for Fracture and Crack Propagation in Heterogeneous Media,” *Computer Methods in Applied Mechanics and Engineering*, juill. 2014. [En ligne]. Disponible: http://www.sciencedirect.com/science/article/pii/S0045782514000905

[72] A. Reinarz, T. Dodwell, T. Fletcher, L. Seelinger, R. Butler et R. Scheichl, “Dune-composites – A new framework for high-performance finite element modelling of laminates,” *Composite Structures*, vol. 184, p. 269–278, janv. 2018. [En ligne]. Disponible: http://www.sciencedirect.com/science/article/pii/S0263822317321797

[73] H.C., Lee, J.S. Choi, K.H. Jung et Y.T. Im, “Application of element deletion method for numerical analyses of cracking,” vol. 35, n°. 2, p. 154–161. [En ligne]. Disponible: http://ww.journalamme.org/papers_vol35_2/3526.pdf

[74] Y. Zhang, J. Zhao, Y. Jia, T. Mabrouki, Y. Gong, N. Wei et T. Rabczuk, “An analytical solution on interface debonding for large diameter carbon nanotube-reinforced composite with functionally graded variation interphase,” vol. 104, p. 261–269. [En ligne]. Disponible: http://www.sciencedirect.com/science/article/pii/S0263822313001931

[75] E. Madenci, *Peridynamic theory and its applications.* New York: Springer, 2014.

[76] K. M. Liechti et Y. S. Chai, “Asymmetric Shielding in Interfacial Fracture Under In-Plane Shear,” *Journal of Applied Mechanics*, vol. 59, n°. 2, p. 295, 1992. [En ligne]. Disponible: http://AppliedMechanics.asmedigitalcollection.asme.org/article.aspx?articleid=1410649

[77] J. Varna, L. A. Berglund et M. L. Ericson, “Transverse single-fibre test for interfacial debonding in composites: 2. Modelling,” *Composites Part A: Applied Science and Manufacturing*, vol. 28, n°. 4, p. 317–326, janv. 1997. [En ligne]. Disponible: http://www.sciencedirect.com/science/article/pii/S1359835X9600125X

[78] W. H. Peters et W. F. Ranson, “Digital Imaging Techniques In Experimental Stress Analysis,” *Optical Engineering*, vol. 21, n°. 3, p. 213427, juin 1982.

[79] F. Hild et S. Roux, “Digital image correlation: from displacement measurement to identification of elastic properties – a review,” *Strain*, vol. 42, n°. 2, p. 69–80, 2006.

[80] L. Chevalier, S. Calloch, F. Hild et Y. Marco, “Digital image correlation used to analyze the multiaxial behavior of rubber-like materials,” *European Journal of Mechanics - A/Solids*, vol. 20, n°. 2, p. 169–187, 2001.

[81] J.-N. Périé, S. Calloch, C. Cluzel et F. Hild, “Analysis of a multiaxial test on a c/c composite by using digital image correlation and a damage model,” *Experimental Mechanics*, vol. 42, n°. 3, p. 318–328, 2002.

[82] F. Mathieu, F. Hild et S. Roux, “Identification of a crack propagation law by digital image correlation,” *International Journal of Fatigue*, vol. 36, n°. 1, p. 146 – 154, 2012.

[83] J. N. Périé, H. Leclerc, S. Roux et F. Hild, “Digital image correlation and biaxial test on composite material for anisotropic damage law identification,” *International Journal of Solids and Structures*, vol. 46, n°. 11–12, p. 2388 – 2396, 2009.

[84] V. Crupi, E. Guglielmino et F. Tavilla, “Application of digital image correlation for the effect of glass fibres on the strength and strain to failure of polyamide plastics,” p. 287–296.

[85] V. Mantič et I. G. García, “Crack onset and growth at the fibre–matrix interface under a remote biaxial transverse load. application of a coupled stress and energy criterion,” vol. 49, nº. 17, p. 2273–2290. [En ligne]. Disponible: http://www.sciencedirect.com/science/article/pii/S0020768312001709

[86] S. A. Silling, “Origin and effect of nonlocality in a composite,” *Journal of Mechanics of Materials and Structures*, vol. 9, nº. 2, p. 245–258, mai 2014. [En ligne]. Disponible: http://msp.org/jomms/2014/9-2/p06.xhtml

[87] H. D. Wagner, M. Rubins et G. Marom, “The significance of microcomposites as experimental models,” *Polymer Composites*, vol. 12, nº. 4, p. 233–236, août 1991. [En ligne]. Disponible: http://onlinelibrary.wiley.com/doi/10.1002/pc.750120404/abstract

[88] H. Zhang, M. L. Ericson, J. Varna et L. A. Berglund, “Transverse single-fibre test for interfacial debonding in composites: 1. Experimental observations,” *Composites Part A: Applied Science and Manufacturing*, vol. 28, nº. 4, p. 309–315, 1997. [En ligne]. Disponible: http://www.sciencedirect.com/science/article/pii/S1359835X96001236

[89] S. Ogihara et J. Koyanagi, “Investigation of combined stress state failure criterion for glass fiber/epoxy interface by the cruciform specimen method,” *Composites Science and Technology*, vol. 70, nº. 1, p. 143–150, janv. 2010. [En ligne]. Disponible: http://www.sciencedirect.com/science/article/pii/S0266353809003546

[90] N. R. Sottos, W. R. Scott et R. L. McCullough, “Micro-interferometry for measurement of thermal displacements at fiber/matrix interfaces,” *Experimental Mechanics*, vol. 31, nº. 2, p. 98–103, juin 1991. [En ligne]. Disponible: http://link.springer.com/10.1007/BF02327559

[91] B. Han, “Higher sensitivity moire interferometry for micromechanics studies,” *Optical Engineering*, vol. 31, nº. 7, p. 1517–1527, juill. 1992. [En ligne]. Disponible: https://www.spiedigitallibrary.org/journals/Optical-Engineering/volume-31/issue-7/0000/Higher-sensitivity-moire-interferometry-for-micromechanics-studies/10.1117/12.57681.short

[92] R. Talreja, “Physical modelling of failure in composites,” *Philosophical Transactions of the Royal Society A: Mathematical, Physical and Engineering Sciences*, vol. 374, nº. 2071, p. 20150280, juill. 2016. [En ligne]. Disponible: http://rsta.royalsocietypublishing.org/lookup/doi/10.1098/rsta.2015.0280

[93] H. A. Bruck, C. L. Moore et T. L. Valentine, “Repeatable bending actuation in polyurethanes using opposing embedded one-way shape memory alloy wires exhibiting large deformation recovery,” *Smart Materials and Structures*, vol. 11, n°. 4, p. 509, 2002. [En ligne]. Disponible: http://stacks.iop.org/0964-1726/11/i=4/a=305

[94] J. Tracy, A. Waas et S. Daly, “A New Experimental Approach for In Situ Damage Assessment in Fibrous Ceramic Matrix Composites at High Temperature,” *Journal of the American Ceramic Society*, vol. 98, n°. 6, p. 1898–1906, juin 2015. [En ligne]. Disponible: http://doi.wiley.com/10.1111/jace.13538

[95] S. Haldar, N. Gheewala, K. J. Grande-Allen, M. A. Sutton et H. A. Bruck, “Multi-scale Mechanical Characterization of Palmetto Wood using Digital Image Correlation to Develop a Template for Biologically-Inspired Polymer Composites,” *Experimental Mechanics*, vol. 51, n°. 4, p. 575–589, avr. 2011. [En ligne]. Disponible: http://link.springer.com/10.1007/s11340-010-9422-7

[96] Ilyass Tabiai, Rolland Delorme, Daniel Therriault et Martin Lévesque, “Additional data for the "In-situ full field measurement during inter-facial debonding in single fiber composite under transverse load",” févr. 2018, type: dataset.

[97] J. B. Petr Hlaváček, “Using of abrasive water jet for measurement of residual stress in railway wheels,” *Tehnicki Vjesnik*, vol. 19, n°. 2, p. 387–390, 2012.

[98] M. Nakazawa, “Mechanism of Adhesion of Epoxy Resin to Steel Surface,” *Nippon Steel Technical Report*, vol. 63, n°. 63, p. 16–22, oct. 2014. [En ligne]. Disponible: http://www.nssmc.com/en/tech/report/nsc/pdf/6303.pdf

[99] S. K. Biswas et K. Vijayan, “Friction and wear of PTFE — a review,” *Wear*, vol. 158, n°. 1, p. 193–211, oct. 1992.

[100] J. Plummer, “What makes epoxy resins good adhesives? Why do they bond so strongly to surfaces?” Mereco Technologies, Londonderry, NH 03053, Rapport technique, 2014. [En ligne]. Disponible: https://goo.gl/PZnCng

[101] P. Mazzoleni, “Uncertainty estimation and reduction in digital image correlation measurements,” 2013. [En ligne]. Disponible: https://www.politesi.polimi.it/handle/10589/74525

[102] F. Hild et S. Roux, “Digital image correlation: from displacement measurement to identification of elastic properties – a review,” *Strain*, vol. 42, n°. 2, p. 69–80.

[103] B. P., K. Q., H. X. et A. A., “Two-dimensional digital image correlation for in-plane displacement and strain measurement: a review,” *Meas. Sci. Technol.*, vol. 20, n°. 6, p. 062001, 2009.

[104] J. Réthoré, F. Hild et S. Roux, “Extended digital image correlation with crack shape optimization,” *International Journal for Numerical Methods in Engineering*, vol. 73, n°. 2, p. 248–272, 2008.

[105] G. Besnard, F. Hild et S. Roux, ““Finite-Element” Displacement Fields Analysis from Digital Images: Application to Portevin–Le Châtelier Bands,” *Experimental Mechanics*, vol. 46, n°. 6, p. 789–803, déc. 2006.

[106] M. Sutton, W. Wolters, W. Peters, W. Ranson et S. McNeill, “Determination of displacements using an improved digital correlation method,” *Image and Vision Computing*, vol. 1, n°. 3, p. 133 – 139, 1983.

[107] A. Mohan et S. Poobal, “Crack detection using image processing: A critical review and analysis,” *Alexandria Engineering Journal*, févr. 2017.

[108] T. Yamaguchi et S. Hashimoto, “Fast crack detection method for large-size concrete surface images using percolation-based image processing,” *Machine Vision and Applications*, vol. 21, n°. 5, p. 797–809, Aug 2010.

[109] T. Yamaguchi, S. Nakamura et S. Hashimoto, “An efficient crack detection method using percolation-based image processing,” dans *Industrial Electronics and Applications, 2008. ICIEA 2008. 3rd IEEE Conference on.* IEEE, 2008, p. 1875–1880.

[110] S. Iliopoulos, D. G. Aggelis, L. Pyl, J. Vantomme, P. Van Marcke, E. Coppens et L. Areias, “Detection and evaluation of cracks in the concrete buffer of the Belgian Nuclear Waste container using combined NDT techniques,” *Construction and Building Materials*, vol. 78, n°. Supplement C, p. 369–378, mars 2015.

[111] M. Hamrat, B. Boulekbache, M. Chemrouk et S. Amziane, “Flexural cracking behavior of normal strength, high strength and high strength fiber concrete beams, using Digital Image Correlation technique,” *Construction and Building Materials*, vol. 106, n°. Supplement C, p. 678–692, mars 2016.

[112] S. Y. Alam, A. Loukili, F. Grondin et E. Rozière, “Use of the digital image correlation and acoustic emission technique to study the effect of structural size on cracking of reinforced concrete,” *Engineering Fracture Mechanics*, vol. 143, n°. Supplement C, p. 17–31, juill. 2015.

[113] J. D. Helm, “Digital image correlation for specimens with multiple growing cracks,” *Experimental Mechanics*, vol. 48, n°. 6, p. 753–762, Dec 2008.

[114] F. J. Vernerey et M. Kabiri, “Adaptive Concurrent Multiscale Model for Fracture and Crack Propagation in Heterogeneous Media,” *Computer Methods in Applied Mechanics and Engineering.*

[115] J. Serra, *Image Analysis and Mathematical Morphology.* Orlando, FL, USA: Academic Press, Inc., 1983.

[116] T. Y. Zhang et C. Y. Suen, “A fast parallel algorithm for thinning digital patterns,” *Commun. ACM*, vol. 27, n°. 3, p. 236–239, mars 1984.

[117] J. C. Russ, *The Image Processing Handbook, Sixth Edition*, 6^e^ éd. Boca Raton, FL, USA: CRC Press, Inc., 2011.

[118] C. E. Shannon, “A mathematical theory of communication,” *Bell System Technical Journal*, vol. 27, n°. 3, p. 379–423, 1948.

[119] S. Nemat-Nasser et M. Hori, *Micromechanics : overall properties of heterogeneous materials.* Amsterdam New York North-Holland, 1993. [En ligne]. Disponible: https://trove.nla.gov.au/version/29758283

[120] Z. Sun, L. Zhao, L. Chen et Y. Song, “Research on failure criterion of composite based on unified macro- and micro-mechanical model,” *Chinese Journal of Aeronautics*, vol. 26, n°. 1, p. 122–129, févr. 2013. [En ligne]. Disponible: http://www.sciencedirect.com/science/article/pii/S1000936112000234

[121] F. Paris, E. Correa et J. Canas, “Micromechanical view of failure of the matrix in fibrous composite materials,” *Composites Science and Technology*, vol. 63, n°. 7, p. 1041–1052, mai 2003. [En ligne]. Disponible: http://www.sciencedirect.com/science/article/pii/S0266353803000174

[122] L. Zhuang, A. Pupurs, J. Varna, R. Talreja et Z. Ayadi, “Effects of inter-fiber spacing on fiber-matrix debond crack growth in unidirectional composites under transverse loading,” *Composites Part A: Applied Science and Manufacturing*, vol. 109, p. 463–471, juin 2018. [En ligne]. Disponible: http://www.sciencedirect.com/science/article/pii/S1359835X18301337

[123] D20 Committee, “Test Method for Tensile Properties of Plastics,” ASTM International, Rapport technique, 2010. [En ligne]. Disponible: http://enterprise.astm.org/filtrexx40.cgi?+REDLINE_PAGES/D638.htm

[124] I. S. Awan, W. Xiaoqun, H. Pengcheng et D. Shanyi, “Developing an approach to calculate carbon fiber surface energy using molecular simulation and its application to real carbon fibers,” *Journal of Composite Materials*, vol. 46, n^o. 6, p. 707–715, mars 2012. [En ligne]. Disponible: http://journals.sagepub.com/doi/10.1177/0021998311410491

[125] S.-Z. Guo, F. Gosselin, N. Guerin, A.-M. Lanouette, M.-C. Heuzey et D. Therriault, “Solvent-Cast Three-Dimensional Printing of Multifunctional Microsystems,” *Small*, vol. 9, n^o. 24, p. 4118–4122, déc. 2013. [En ligne]. Disponible: http://onlinelibrary.wiley.com/doi/10.1002/smll.201300975/abstract

[126] A. Pizzi et K. L. Mittal, édit., *Handbook of adhesive technology*, 2^e éd. New York: M. Dekker, 2003.

[127] Xiaoying Rong et Malcolm Keif, “A study of PLA printability with flexography,” 2017. [En ligne]. Disponible: https://pdfs.semanticscholar.org/b89c/c2f09e317f86150d8c21e6f4cacc2fb0c828.pdf

[128] A. N. Borodin, A. I. Sologubov, L. A. Chernenko, P. I. Zolkin, H. M. Aberyahimov et G. A. Grigoriev, “The Influence of Carbon Fibre Surface Energy on their Interfacial Interaction with Resins,” dans *MICC 90: Moscow International Composites Conference, 1990*, I. N. Fridlyander et V. I. Kostikov, édit. Dordrecht: Springer Netherlands, 1991, p. 464–468. [En ligne]. Disponible: https://doi.org/10.1007/978-94-011-3676-1_78

[129] R. B. Ins, Olympic Scientific Solutions Americas, “Laser Confocal Microscopy: Challenging the Limits of Measuring Surface Roughness,” 2017. [En ligne]. Disponible: https://www.photonics.com/a58301

[130] S. Ho et Z. Suo, “Tunneling Cracks in Constrained Layers,” *Journal of Applied Mechanics*, vol. 60, n^o. 4, p. 890–894, déc. 1993. [En ligne]. Disponible: http://dx.doi.org/10.1115/1.2900998

[131] Ilyass Tabiai, Rolland Delorme, Daniel Therriault et Martin Lévesque, “Additional data for the "In-situ full field measurement during inter-facial debonding in single fiber composite under transverse load",” févr. 2018, type: dataset. [En ligne]. Disponible: https://zenodo.org/record/1188272#.WsOTN4jwaMo

[132] O. J. Nixon-Pearson et S. R. Hallett, “An experimental investigation into quasi-static and fatigue damage development in bolted-hole specimens,” *Composites*

Part B: Engineering, vol. 77, p. 462–473, août 2015. [En ligne]. Disponible: http://www.sciencedirect.com/science/article/pii/S1359836815001705

[133] A. Perrier, F. Touchard, L. Chocinski-Arnault et D. Mellier, “Quantitative analysis by micro-CT of damage during tensile test in a woven hemp/epoxy composite after water ageing,” *Composites Part A: Applied Science and Manufacturing*, vol. 102, p. 18–27, nov. 2017. [En ligne]. Disponible: http://www.sciencedirect.com/science/article/pii/S1359835X17302762

[134] E. Gogolides, V. Constantoudis, G. Kokkoris, D. Kontziampasis, K. Tsougeni, G. Boulousis, M. Vlachopoulou et A. Tserepi, “Controlling roughness: from etching to nanotexturing and plasma-directed organization on organic and inorganic materials,” *Journal of Physics D: Applied Physics*, vol. 44, n°. 17, p. 174021, mai 2011. [En ligne]. Disponible: http://stacks.iop.org/0022-3727/44/i=17/a=174021?key=crossref.1c3ca31e000a28bb982d97592f16fb63

[135] G. Rajagopalan, K. Immordino, J. Gillespie et S. McKnight, “Diffusion and reaction of epoxy and amine in polysulfone studied using Fourier transform infrared spectroscopy: experimental results,” *Polymer*, vol. 41, n°. 7, p. 2591–2602, mars 2000. [En ligne]. Disponible: http://linkinghub.elsevier.com/retrieve/pii/S0032386199004188

[136] G. Lucchetta, “Experimental analysis of atmospheric plasma treatment and resin optimization for adhesive bonding of carbon fiber/epoxy composites,” Laurea magistrale in ingegneria aerospaziale, Universita degli studi di padova, Padova, 2015. [En ligne]. Disponible: http://tesi.cab.unipd.it/48832/1/Tesi_ANTONELLO_Julien.pdf

[137] L. Asp, L. Berglund et R. Talreja, “Prediction of matrix-initiated transverse failure in polymer composites,” *Composites Science and Technology*, vol. 56, n°. 9, p. 1089–1097, janv. 1996. [En ligne]. Disponible: http://linkinghub.elsevier.com/retrieve/pii/0266353896000747

[138] D. Marshall et A. G. Evans, “Failure Mechanisms in Ceramic-Fiber/Ceramic-Matrix Composites,” *Journal of the American Ceramic Society*, vol. 68, n°. 5, p. 225–231, mai 1985. [En ligne]. Disponible: http://onlinelibrary.wiley.com/doi/10.1111/j.1151-2916.1985.tb15313.x/abstract

APPENDIX A PUBLISHED PAPERS

- Rolland Delorme, Ilyass Tabiai, Louis Laberge Lebel, Martin Lévesque. Generalization of the ordinary state-based peridynamic model for isotropic linear viscoelasticity, Mechanics of Time-Dependent Materials, February 2017, DOI: 10.1007/s11043-017-9342-3
- Ilyass Tabiai, Rolland Delorme, Daniel Therriault, Martin Lévesque. In-situ full-field measurements during interfacial debonding in single-fiber composites under transverse load, Experimental Mechanics, September 2018, DOI: 10.1007/s11340-018-0429-9
- Patrick Diehl, Ilyass Tabiai, Felix W. Baumann, Daniel Therriault, Martin Lévesque. Long term availability of raw experimental data in experimental fracture mechanics, Engineering Fracture Mechanics, June 2018, DOI: 10.1016/j.engfracmech.2018.04.030

APPENDIX B SUBMITTED PAPERS

- Ilyass Tabiai, Gleb Tkachev, Patrick Diehl, Steffen Frey, Thomas Ertl, Daniel Therriault, Martin Levesque. Hybrid image processing approach for crack area detection and tracking using local digital image correlation results applied to single fiber inter-facial debonding. Submitted to Engineering Fracture Mechanics in October 2018
- Ilyass Tabiai, Damien Texier, Philippe Bocher, Daniel Therriault, Martin Lévesque. In-situ full field out of plane displacement and strain measurements at the micro-scale in single reinforcement composites under transverse load. Submitted to Experimental Mechanics in October 2018
- Rolland Delorme, Patrick Diehl, Ilyass Tabiai, Louis Laberge Lebel, Martin Lévesque. Extracting constitutive mechanical parameters in linear elasticity using the virtual fields method within the ordinary state-based peridynamic framework. Submitted to International Journal of Solids and Structures in October 2018

APPENDIX C OPEN SOURCE CODE

- Patrick Diehl, Ilyass Tabiai. (2017). IaPCS/gmsh-exodus-converter: Release v1.0, DOI: http://doi.org/10.5281/zenodo.437171, Tool which converts a mesh written with gmsh to the Exodus II format, which is used in common simulations tools, such as Peridigm.

- Patrick Diehl, Ilyass Tabiai. (2017). IaPCS/gmsh-to-nodes Generates nodes and volumes from gmsh grid for nodal or particle simulations, each particle is affected with a colume value which is proportional to the element its represents volume (or surface in 2D).

- Patrick Diehl, Rolland Delorme, Ilyass Tabiai. lm2-poly/PeriPyDI, DOI: 10.5281/zenodo.1405731, Peridynamics (PD) computations for state-based PD in 1D, 2D for elastic and viscoelastic materials. Also possible to import Digital Image Correlation results and compute PD forces for each pixel as a node.

- Soufian Hifdi, Ilyass Tabiai, Yahya Abderaffai. (2018). DOI: 10.5281/zenodo.1444066, Python package containing a set of tools to convert G-code to the proprietary commands format used for Fisnar dispensers. The code can be used to convert G-code provided by a 3D printing slicer software to printable Fisnar parts. It supports up to 3 nozzles for multi-material printing.

- Patrick Diehl, Ilyass Tabiai. (2018, March 20). OpenDataExpMechanics/Survey: Final release (Version 1.0). Zenodo. http://doi.org/10.5281/zenodo.1203766 Paper containing the code used to generate results for the publication *Long term availability of raw experimental data in experimental fracture mechanics*. It can be used to perform a similar survey or to further explore results provided in the publication.

APPENDIX D EXPERIMENTAL DATA PACKAGES

- Ilyass Tabiai. (2017). PMMA tensile test until failure, loaded in force. Zenodo. http://doi.org/10.5281/zenodo.895265
- Ilyass Tabiai, Rolland Delorme, Patrick Diehl, Louis Laberge Lebel, Martin Lévesque. (2018). PMMA 3 point bending test until failure loaded in displacement. Zenodo. http://doi.org/10.5281/zenodo.1172068
- Ilyass Tabiai, Rolland Delorme, Daniel Therriault, Martin Lévesque. (2018). Additional data for the "In-situ full field measurement during inter-facial debonding in single fiber composite under transverse load". Zenodo. http://doi.org/10.5281/zenodo.1188272
- Ilyass Tabiai, Damien Texier, Philippe Bocher, Daniel Therriault, Marin Lévesque. (2018). Additional data for "In-situ full field out of plane displacement and strain measurements at the micro-scale in single reinforcement composites under transverse load". Zenodo. http://doi.org/10.5281/zenodo.1464268